Czech Technical University in Prague

Faculty of Electrical Engineering

Doctoral Thesis

April 2013

João Vitor Bernardo Pimentel

Czech Technical University in Prague

Faculty of Electrical Engineering

Department of Electrotechnology

Adaptive self-lubricating low-friction coatings

Doctoral Thesis

João Vitor Bernardo Pimentel

Prague, April 2013

Ph.D. Programme: Electrical Engineering and Information Technology

Branch of study: Electrotechnology and Materials

Supervisor: Doc. Ing. Tomáš Polcar, Ph.D.

Acknowledgements

Before we plunge into the world of spectra and tribolayers, I would like to thank in writing some among the many people without whom this work would have been impossible or, at the very least, a lot more difficult:

Those who shared with me their workspace and time at the laboratory of the Advanced Materials Group – Tomáš Vitů, Petr Mutafov, Karolina Tomešová, and professor Rudolf Novák.

Professor Albano Cavaleiro, at the Department of Mechanical Engineering of the University of Coimbra, and other members of the department, particularly Manuel Evaristo and João Carlos Oliveira, who instructed me in deposition and characterisation techniques, let me use their equipment and time, and tolerated me getting locked in or outside their laboratories.

Finally, Sarah Penteado, who agreed to come with me to a part of the world we did not know, so I could do something I was not quite able to explain. Hopefully, now everything will become clearer.

On a more formal note: this work was supported by the Czech Science Foundation through the project 108/10/0218 and by CTU student grant competition (SGS) OHK4-035/10.

Off we go, then.

Note regarding the experimental procedures

All films with which we deal here were deposited by sputtering at the Department of Mechanical Engineering, University of Coimbra. The following systems were deposited by the author: W-S-Cr (Chapter 5), W-S-C-Cr (Chapter 6), Mo-S-C-Ti and W-S-C-Ti (Chapter 7). The other systems (described in Chapters 3, 4, and 8) had been prepared previously.

Tribological pin-on-disk tests, ball-cratering tests, Raman spectroscopy and three-dimensional optical profilometry were performed by the author at the Faculty of Electrical Engineering of the Czech Technical University in Prague. Scratch tests and nanoindentation were performed along with depositions by the author at the University of Coimbra.

Other measurements were carried out by colleagues at the Czech Technical University in Prague (FTIR and grazing incidence XRD of W-S-C-Cr), Jan Evangelista Purkyně University in Ústí nad Labem (XPS of W-S-C), Uppsala University (XPS of W-S-C-Cr), and University of Coimbra (EPMA, SEM, TEM, XRD and XPS).

Contents

List of Figures

List of Tables

List of Abbreviations

a.u.	Arbitrary units
BE	Binding energy
CLST	Constant load scratch test
d.c.	Direct current
DLC	Diamond-like carbon
DPSS	Diode-pumped solid-state laser
EDX, EDS	Energy dispersive X-ray spectroscopy
EPMA	Electron probe microanalysis
FC	Friction coefficient
FIB	Focused ion beam
FTIR	Fourier transform infrared spectroscopy
FWHM	Full width at half maximum
PLD	Pulsed laser deposition
PLST	Progressive load scratch test
PVD	Physical vapor deposition
r.f.	Radio frequency
RH	Relative humidity
SEM	Scanning electron microscopy
TEM	Transmission electron microscopy
TMD	Transition metal dichalcogenide
UV	Ultraviolet
XPS	X-ray photoelectron spectroscopy
XRD	X-ray (micro)diffraction

List of Symbols

μ	Friction coefficient
A	Arbitrary constant, associated with material and contact conditions
A_c	Cross-section
A_d	Displacement area (in nanoindentation)
A_{max}	Stabilization value of the cross-section area after variations
B	Constant associated with the length of the sliding test
B_w	Arbitrary constant used in the analysis of the wear of patterned samples
D	Diameter of the ball (in ball-cratering test)
d	Distance between crystal planes (in XRD)
d	Distance from a groove to the preceding one
F	Frictional force (in sliding tests)
h	Depth of penetration (in nanoindentation)
H	Hardness
I_C	Total area of peaks attributed to C in a Raman spectrum
I_D	Area of the D peak in a Raman spectrum
I_G	Area of the G peak in a Raman spectrum
I_{MoS2}	Total area of peaks attributed to MoS_2 in a Raman spectrum
I_{WS2}	Total area of peaks attributed to WS_2 in a Raman spectrum
k	Wear rate
L	Load
M	Metal (Mo or W)
n	An arbitrary integer used in describing Bragg's law
N	Normal force exerted by the load (in sliding test)
P	Load in nanoindentation
P_C	Power applied to the C (graphite) target
P_{C+WS2}	Power applied to the graphite target (with WS_2 pellets)
P_{Cr}	Power applied to the Cr target
P_{max}	Maximum load applied (in nanoindentation)
P_{MoS2}	Power applied to the MoS_2 target
P_{WS2}	Power applied to the WS_2 target
Ra	Average surface roughness
s	Linear speed in sliding tests
S	Total running distance of a sliding test
t	Film thickness
V	Worn volume
x	Total width of crater, minus apparent width of the film (in ball-cratering test)
y	Apparent width of the film (in ball-cratering test)
θ	Angle between the incident radiation and the planes of the lattice (in XRD)
λ	Wavelength of the radiation (in XRD and XPS)
ν_0	Frequency of the incident laser (in Raman spectroscopy)
ν_m	Vibrational frequency of a molecule (in Raman spectroscopy)

1 Introduction and Objectives

The study of the natural phenomena in tribology is relatively new in science, having benefited strongly with the development of advanced instrumentation in the 20th century, which opened many possibilities for investigation of its fundaments. The study of tribology itself, as the interaction between surfaces in relative motion, is much older: we can consider for example that in the 15th century basic laws of friction were being studied by Leonardo da Vinci. Still, the term *tribology* was only introduced as a new field of science in 1967, having its root in the Greek *tribos*, for rubbing or sliding [1].

The study of interacting surfaces is a means to extending the lifetime of most devices created by mankind, by finding ways to reduce friction and wear, but not limited to that. It also relates to our own bodies, full of joints with their own lubrication and subject to wear. In a recent study, it was proposed that the skin on the tips of our fingers develop wrinkles when wet due to an evolutionary mechanism, to improve the grip on wet surfaces [2] and so to *avoid* low friction. Indeed, there is a very wide range of applications related to tribology.

The importance of tribological properties of mechanical systems is crucial nowadays, although it may be often overlooked. Wear is the major cause of waste of material and degradation of mechanical performance, and friction is directly related to significant global energy losses. About 30% of the energy resources in the world is spent in friction [3]. Studies conducted since the second half of the 20th century estimated that the effort to overcome friction would cause losses of about 1–5% of the Gross National Product of an industrialized country [1,4,5]. Besides, there are environmental issues associated with the disposal of lubricants used to reduce frictional losses.

This work is dedicated to the study of self-lubricant thin films for tribological applications. These films are layers deposited over the surface of a substrate, or bulk material, with the main purpose of enhancing (or adding) some properties to the composite system *substrate–coating* [6].

1.1 Adaptive solid lubricant coatings

Self-lubricant films have been in focus for several decades for their potential use in aerospace applications. The movable devices in this type of applications face friction and wear in the contact of moving parts, low-frequency vibrations and high loads which are, furthermore, repeated in extremely different conditions, e.g., from relatively high pressure and humidity on land during take-off, to low pressure and humidity in high altitudes [7,8]. Mechanisms in devices designed for outer space may face even more drastic conditions. Satellites operate in a temperature range typically from -100 to +100 °C, and shuttles are subject to terrestrial/space environmental cycling, where temperatures may exceed 1000 °C upon atmospheric re-entry [8].

For applications such as mechanical systems in outer space, it can be a critically important requirement that mechanical systems remain "dry", using liquid lubricants only when the interface in which they act can be completely sealed from the outside [9], while the pressure and temperature conditions make this even more difficult. Nevertheless, special types of liquid lubricants have been the predominant material for lubrication in aerospace systems [7,8]. As for solid lubricants, transition metal dichalcogenides (TMDs, which had also been used as additives for oil lubricants, providing significant wear and friction reduction [10,11]) were commonly used in space applications deposited by spray or vacuum deposition methods, applied as powders, or burnished [12]. However, these materials were soft and oxidized easily in air [7,13]. More advanced approaches were sought in an attempt to develop solid lubricants that could perform well enough in different environments, temperatures, and load conditions. This led to composites of oxides and TMDs (such as PbO/MoS_2 and ZnO/WS_2) [14,15] and metal-doped TMDs [16,17]; their deposition was made possible by advances in vacuum deposition methods. It also motivated the development of self-lubricant composites combining properties of solid lubricants and a supporting matrix, whose structure and mechanical behaviour could change according to the conditions of contact and environment to maintain good friction and low wear. For aerospace applications, the most obvious advantage of the versatility exhibited by adaptive coatings is that, if a coating displays good properties both in dry and humid atmospheres, the system may use only one type of solid (self-) lubricant.

Coatings which are able to adapt their properties to satisfy the requirements of the operating conditions are often called *adaptive* or *smart* coatings. Early examples were nanocomposite structures that combined carbides (TiC, WC) and TMDs (MoS_2, WS_2) embedded into amorphous

carbon matrices [7–9]. The development of doped TMD films led to increased load bearing capacity and improved adhesion, and thus they were able to provide an alternative for hard coatings, which do not usually exhibit low friction [18]. While the tribological performance of TMD-based films is particularly good in dry nitrogen or dry air (as caused by loss of humidity in elevated temperatures, for example), recent studies by Cavaleiro et al. have shown that this type of coatings can exhibit very low friction in humid air as well, due to their adaptive characteristic [19], and therefore the motivation for their use is not limited to environmental cycling or changing conditions. The properties of adaptive coatings, especially those combining transition metal dichalcogenides and amorphous carbon, will be detailed further.

1.2 Scope of the thesis

In this work, different compositions and systems of sputtered self-lubricating adaptive coatings, based on tungsten and molybdenum, were studied, deposited, characterised, and tested. The core objective of this study was to develop self-lubricant thin films based on molybdenum and tungsten disulfides or diselenides, doped with different elements. The tribological properties desired were improved hardness compared to undoped films, low friction, and high wear resistance. The focus was kept on understanding and improving their characteristics in humid air.

The thesis is divided into three parts. First, an introduction to the fundamental properties of the studied films, along with a description of the techniques of coating deposition and analysis (Chapter 2). Next, in Chapters 3–8 are presented experimental results and analyses of the different systems of films, organized according to their composing elements (i.e. base TMD and dopants) as follows:

- In Chapter 3, we study Mo-S-C films focusing on the influence of the concentration of carbon on their tribological properties. Several techniques are used to investigate the films' microstructure and changes in their bonding states caused by the dopants.
- In Chapter 4, we study a single composition of W-S-C focusing on the effects of sliding on the coating material, such as the influence of different contact loads on the changes caused on the surface of the wear tracks.
- In Chapter 5, we analyse W-S-Cr coatings, focusing on deposition procedures and on the characterisation of the as-deposited coating.

- In Chapter 6, an extensive examination of W-S-C-Cr coatings is presented, analysing the overall characteristics of the as-deposited coatings related to Cr content, as well as the tribological behaviour under different loads and durations. Furthermore, we study the effect of surface texture on a W-S-C-Cr coating's tribological behaviour.
- In Chapter 7, we examine films based on MoS_2 and WS_2 doped with carbon and titanium (Mo/W-S-C-Ti). These coatings are based on those presented in Chapters 3 and 4, therefore we analyse their mechanical and tribological properties focusing on the effects of adding Ti.
- In Chapter 8, we briefly examine coatings based on diselenides ($MoSe_2$ and WSe_2) doped with carbon, focusing on the characteristics they share with those based on disulfides.

Finally, in Chapter 9, we summarize and discuss the main results presented.

2 Fundamental concepts

2.1 Transition metal dichalcogenides (TMDs)

The films developed in the aim of the thesis belong to the class called transition metal dicalchogenides – films composed of sulfides, selenides or tellurides of tungsten, molybdenum or niobium. TMDs exhibit unique properties based on the high degree of anisotropy in their structures, in a kind of lamellar nature similar also to that of graphite, which is the basis for the good lubricating properties of these materials [5]. However, they may differ in lubrication mechanisms [13].

The basic structure of the TMD is a hexagonal cell (rhombohedral is also possible, but can be ignored for the purposes of this study) in which the metal atom sits in the middle of a 'sandwich', the top and bottom being the chalcogen atoms. Each metal atom is equidistant to six chalcogen atoms, and each chalcogen atom is equidistant to three metal atoms. The bonds within the sandwich structure are strong, but the bonds between layers – that is, the bonds between the chalcogens of adjacent cells – are very weak van der Waals forces. Given a polycrystalline structure composed of such cells, if the sliding against a partner takes place in a plane parallel to that of the TMD layers, the bonds between the cells are easily broken and the upper layers slide over the ones below. This *type I* configuration, with the basal planes of the crystallites parallel to the sliding surface, is favorable for low friction. If the basal planes are perpendicular to the sliding surface (*type II*), the self-lubricity is lost; however, it is still possible that the sliding process reorients the TMD material: the strong bonds between metal and dichalcogenide are not broken, but the cells are moved/rotated, so that the sliding itself causes a preferred orientation on the surface [20].

The hexagonal structure of MoS_2 is shown in Fig. 2.1. The layer of MoS_2 above is identical to the one below, but they are displaced laterally. The S atoms in one layer are vertically aligned between themselves and with the Mo atoms in the layer below, and vice-versa. Such configuration, referred to as 2H-MoS_2, is not the only possible phase for MoS_2; but since it is the most stable phase, it is usually referred to simply as MoS_2 [21].

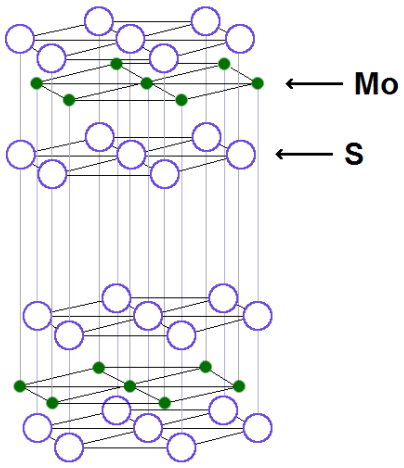

Fig. 2.1 Hexagonal structure of 2H-MoS_2 (adapted from [11]).

The low friction properties resulting from the typical "sandwich" structure of TMDs are not identical for all members of the TMD family. For example, niobium disulfide is outperformed by molybdenum disulfide. The most significant difference in their lattices is that, while Mo atoms in MoS_2 are positioned above S atoms of the layer below, in NbS_2 the Nb atoms from different layers are aligned [20]. This characteristic alone is sufficient to make the interaction between layers in NbS_2 stronger than in MoS_2, and therefore to increase friction and worsen the lubricating capacity. A rotational disorder between layers of MoS_2, leading to less intense interactions, has been associated with ultra-low friction [22,23].

In vacuum or dry atmosphere (e.g. dry nitrogen), TMDs display very low friction coefficients; sliding in ultra-high vacuum conditions even leads to superlubricity. The term applies to conditions where friction and resistance to sliding nearly vanish; the factors that contribute to friction are practically non-existent [5]. The mechanisms of superlubricity have been related to high anisotropy of surface contact [5,22,24,25].

The orientation of the basal planes is influenced by the deposition method, but it is of course probable, when dealing with non-ideal conditions, that the film will have both types of orientation. In this interpretation, it is considered that films of type I will have good self-lubricating

properties. However, the orientation that would be the best for lubricating properties on the surface would also be the one with the worst adhesion to the substrate. A common problem of pure sputtered TMD films is the formation of porous or columnar structures in the material [26]. The weak bonding in the interface between large crystallites with different orientations can be a cause of failure during sliding: when a force is applied on an inner structure along the direction where it resists strongly, it may end up 'pulling out' part of the material.

TMDs are very susceptible to oxidation, especially when the surface crystals are not in the preferred orientation described above, since the crystal edges are more reactive [27]. Porosity also promotes penetration of contaminants in gaseous state, such as oxygen or water vapour. Water molecules can react with dangling bonds at the edge of the crystallites, hindering sliding of one layer over another and their reorientation in the contact area. Furthermore, oxygen reacts very easily, substituting atoms of the chalcogenide in the TMD structure. Regarding the oxidation of molybdenum disulfide, it has been proposed by Fleischauer and Lince [28], and later shown by Joly-Pottuz et al. [29], that for very low amounts of oxygen an isostructural phase $MoS_{2-x}O_x$ is created which does not hinder the easy sliding. For higher concentrations of oxygen, the O atoms substituting S create notches and depressions in the layer structure; consequently, the interface between layers is less smooth (at the atomic level) and friction is higher. When the oxygen content increases even further, such defects are more widespread and the surface becomes more homogeneous, therefore friction decreases again until the level achieved for molybdenum oxide (higher than for MoS_2). Onodera et al. [30] studied the friction properties of MoS_2 sheets using a quantum-chemistry-based molecular simulation and found compatible results, noting moreover that the increase of friction in oxygen-containing films could be related to the reduction of S-S Coulombic repulsion.

Surface oxidation is strongly enhanced in exposure to humid air (in storage, for example). However, the process of sliding under a contact load can easily remove the surface oxides and create a pure-TMD tribolayer [19]. It should be noted that in most TMD films deposited by PVD techniques (and in all those presented in this work) there is oxygen in the as-deposited films, originating from the residual atmosphere in the chamber [19,29]. In the case of our films, the use of very porous WS_2 and MoS_2 targets in deposition which had been stored in open air contributed as well to the amount of oxygen in the chamber.

Another typical drawback of TMDs is their low load-bearing capacity. MoS_2 and WS_2 films typically have hardness values below 1 GPa. One way of solving this problem which has proved successful is alloying of TMDs with other elements or compounds.

2.2 Doped TMDs

The introduction of dopant atoms in the deposition of TMD films prevents the formation of large TMD structures in the film (i.e. large grain sizes) and hinders columnar growth. In some cases the resulting structure is fully amorphous, such as in the case of Mo-S-Pb [17] or W-S-N coatings [19]. This reduces the occurrence of failures due to columnar and porous structures, which improves adhesion and provides a level of protection against contamination [31,32] as described above. Furthermore, the more compact and denser structure improves the hardness of the film.

Studies developed at the University of Coimbra with tungsten disulfide (WS_2) alloyed with carbon and nitrogen showed increase of hardness achieved by doping of one order of magnitude and higher [33]. Those results also showed that the improvement in mechanical properties of WS_2 films when doping with carbon or nitrogen reached their peak at dopant content close to 50 at.%. These conclusions have been validated in later studies [34,35] as well as by other authors [36].

Increased hardness and density did not, however, directly account for the low friction observed. It has been suggested that if the formation of a porous structure is avoided, the coating will be less susceptible to contamination (especially from water and oxygen from the environment) which would deteriorate tribological properties. Contamination would also decrease in more disordered morphologies since preventing long-range order of the TMD phase would decrease the propagation of cracks on the film surface, a source of unsaturated bonds which react rapidly with the environment [27].

An alternative suggestion was that the dopant material, particularly in the case of carbon, would contribute actively to the decrease in friction – graphite would not only cause the changes in morphology described above, but moreover would interact with the sliding partner, thus acting also with its own low-friction characteristics – a concept of great interest especially for what was called the *chameleon effect*. The idea was that the benefit of doping TMD films with carbon went beyond enhancing their mechanical properties: these films would maintain the typical excellent tribological behaviour of TMDs when in dry air or vacuum; and in humid air, the good tribological properties of diamond-like carbon films (DLCs) would be predominant. Thus, the coating would change its characteristics depending on the environment [37]. Voevodin et al. developed such type of films (as WC/DLC/WS_2), performing sliding tests in cycling environment (dry and humid atmospheres, alternately) and showing that the tribological behaviour was indeed good, with friction coefficients as low as 0.02 during the dry cycles and about 0.10–0.20 during the high-

humidity cycles. The hypotheses made to explain the environmental adaptation of the coatings was that, in vacuum, the formation of WS_2 tribolayer would be predominant, but as the environment adopted humid conditions, the tribolayer would quickly oxidize, be destroyed, and replaced by graphite layers [7].

However, the hypothesis of the "chameleon" effect has not been supported by recent results. It seems more likely that the main contribution of dopants to the friction behaviour is related to facilitating the formation of a low-friction tribolayer consisting exclusively of TMD between sliding partner and coating. In other words, the carbon role in friction is only indirect by increasing coating hardness and density. Polcar et al. [38] have shown that wear track analysis from sliding tests in dry and humid air presented no significant difference and that in both conditions there was the formation of a TMD tribolayer. Similar results were obtained during this work, and will be discussed below.

2.3 Deposition methods

Sputtering is a method used either for cleaning surfaces or for physical vapor deposition (PVD). The target (solid) is placed in a vacuum chamber filled with an inert gas (typically Ar). By subjecting the gas to a strong electric field, electrons freed in the ionization process (a small number of atoms in the gas is ionized at any time) are accelerated, thereby colliding with and ionizing other atoms. Thus the plasma is generated [39]. The electric field can be generated by direct current (d.c.) or by radio frequency (r.f.) power sources. (In the case of r.f. sputtering, the acceleration can be directed by the alternating field because electrons and ions will not respond equally to the negative and positive semi-cycles.) The electric field accelerates the ions in the plasma towards the target, hitting it with high kinetic energy; if the ions are accelerated enough, the collisions eject atoms from the target. Magnetrons are used in deposition chambers to "trap" electrons near the surface of the targets, therefore increasing the probability that they will ionize further gas atoms.

By placing the targets of the material to be deposited face to face with the substrates where the deposition takes place, atoms ejected from the surface of the target will reach the substrate with enough energy to adhere to (or to be implanted into) the surface. With time, the substrate's surface will be coated with the material sputtered from the target. When more than one target is in position in the vacuum chamber, the coating will be a combination of those materials; such process

is called *co-sputtering*. Another way to add a material to the final composition is to introduce a reactive gas into the chamber during deposition. Its ions can be accelerated towards the substrate as well, similarly to what happens with the inert ionized gas; however, their main role is to react with atoms sputtered from the target.

During the sputtering process, there are several phenomena occurring at the same time. For example, Ar^+ ions and accelerated electrons may hit the substrate and eject atoms from the coating (*re-sputtering*), or ions and electrons may hit the surface of the target without enough energy to eject atoms, but heating locally the surface; the atoms sputtered from the target may suffer collisions (if the pressure is too high and the plasma too dense) and lose energy needed to reach the substrate and form a dense film. Thus it can be seen that conditions inside the chamber, such as the pressure and distance between target and substrate, influence the results of depositions. The final composition of the coating also depends on controlling adequately the deposition parameters: each material exhibits a different sputtering rate, therefore the electric field that accelerates ions towards a target must be controlled to have the desired deposition rate and, in case of co-sputtering, composition ratio. Although all tungsten and molybdenum disulfides presented in this work were sub-stoichiometric (i.e. with deficiency in sulfur) due mainly to re-sputtering and the influence of the residual atmosphere (see section 2.3), they still exhibited S/W or S/Mo ratios above a level where the self-lubricating properties are lost [11,34]. Moreover, for the purposes of tribological testing, W/Mo disulfides were the most crucial components in the material and were in fact detected near the surface, as will be discussed later. For the same reason, these coatings will be referred to as "doped TMDs" even when the TMD is not the major part of the chemical composition.

Fig. 2.2 represents schematically a deposition chamber to exemplify the co-sputtering method used in this work; in the case shown, the Edwards ESM 100 unit used to deposit WS_2 doped with C or C + Cr. The targets are made of chromium and carbon (graphite). Pellets of WS_2 are placed in the erosion zone of the C target, i.e. in the area where the sputtering occurs more intensely (due to influence of the electromagnetic fields). For a given set of deposition parameters, the ratio between Cr and WS_2 + C in the coating can be controlled by the individual powers applied to the targets. The ratio between WS_2 and C, on the other hand, is controlled by the number of pellets. In this work, the number of pellets was determined empirically to achieve the desired ratios. Finally, the S/W ratio on the film is sensitive to deposition conditions; re-sputtering, for example, is more likely to eject S from the substrate than W, since sulfur atoms are much lighter than tungsten atoms.

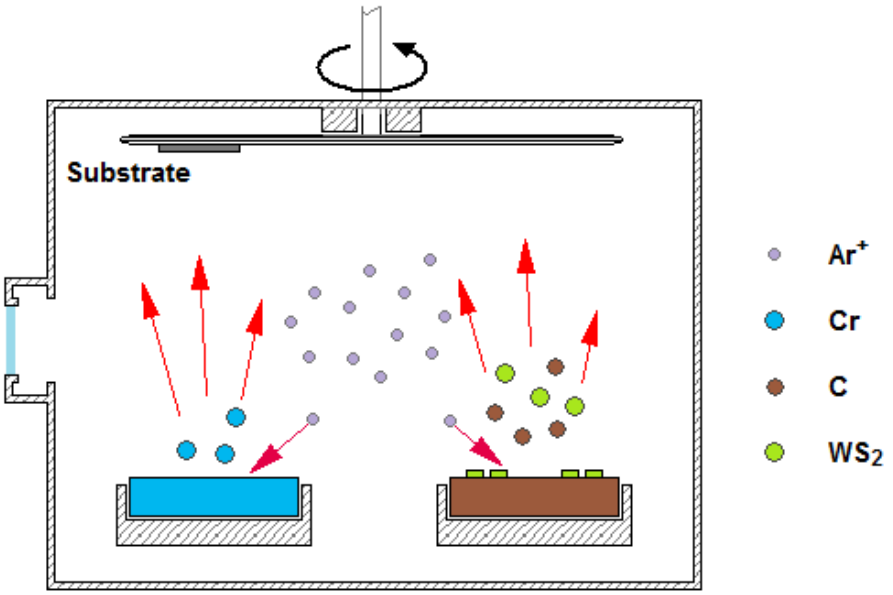

Fig. 2.2 Representation of a vacuum deposition chamber for magnetron co-sputtering.

The substrates are kept rotating above the targets so that they are constantly moving, passing above each target alternately. A multilayered structure is not formed if the rotation speed is high enough, when taking into account the coating growth rate: the samples do not stay above either target long enough for a multilayered structure to grow. The coatings deposited in the scope of this work were all deposited in such a way to avoid multilayers. For example, with the deposition rates obtained it would take approximately 1.2 seconds to deposit a single layer of MoS_2 (3.16 Å thick [11]) with the substrate static above an MoS_2 target, whereas in practice the substrates passed over both targets in the chamber in less than one second. The Hartec deposition chamber used for d.c. magnetron sputtering had a similar structure, with the targets positioned on adjacent walls and the substrates rotating around a central axis, and the same considerations apply as well.

2.4 Techniques of characterisation and analysis of thin films

The properties of deposited coatings were characterised by different analytical methods. This section provides a brief overview of the methods used to analyse the coatings presented in this work.

2.4.1 Electron probe microanalysis

Electron probe microanalysis (EPMA, also known as electron microprobe analysis) is a non-destructive technique used to determine the chemical composition of a material. The sample is bombarded with an electron beam, and so the material emits X-ray photons which are detected (see Fig. 2.3). The wavelengths of these X-rays are characteristic of the elements which emitted them, and thus the chemical composition of the sample can be determined.

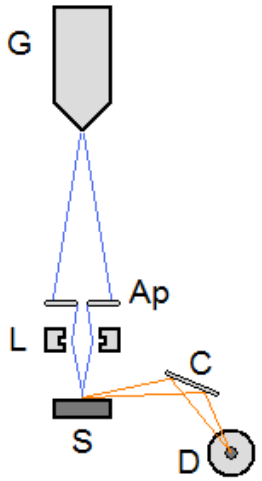

Fig. 2.3 Simplified schematic of electron probe microanalyser (adapted from [40]). *G*: electron gun; *Ap*: aperture; *L*: lens; *S*: sample; *C*: diffraction crystal; *D*: X-ray detector.

For a quantitative analysis, it is assumed that the composition of the sample material is homogeneous. The electrons bombarding the sample have energy of up to 30 keV [41,42]. The measurement is performed on a small volume and the penetration depth of the microprobe depends on the material, usually in the order of 1 μm [41]. It may be a problem for analysis if the film is thinner than the penetration depth, such that the substrate material influences the measurements; or if the material presents significant differences along the examined volume, as for example when the exposed surface of the film is heavily oxidized.

The determination of the composition is not straightforward: the intensity of the detected X-rays attributed to each element is compared with a standard, which is based on the results obtained from a material with a known amount of the same element. The amount of that element in the sample is determined from this comparison. Other factors may influence the measurements and must be considered before the final composition is determined, such as the absorption of x-

rays as they pass through the sample, or the fluorescence propagated out of the sample. These factors may be known and compensated in the standard, but can occur differently in the standard and in the sample; so their effect can be thought of as a background to the measurement that should be corrected when quantifying the data [40].

That is why, in our experimental results, it was not unusual for the final composition of the films analysed by EPMA to add up to an amount different than 100%, in atomic percentage (i.e. the percentage of atoms of a certain element relative to the total number of atoms). If this difference was too large (e.g. total composition below 95%), the measurement was discarded. Otherwise, the atomic percentages were corrected to 100%. In most cases, unless otherwise stated, the EPMA results presented here were weighed as a sum of all target elements: oxygen was excluded, since oxygen contamination on the surface was inevitable and always appeared in EPMA results. All EPMA results described in this work were obtained using a Cameca SX50.

2.4.2 Nanoindentation

Hardness values of the coatings were measured by depth-sensing indentation technique (nanoindentation). The indentation technique works by pressing a very hard tip into the coating, applying a controlled load. The depth of the penetration is measured. If the mechanical and geometrical properties of the tip are well known, then the area of the indentation produced on the coating can be calculated from only the penetration depth. The hardness H is given by

$$H=\frac{P_{\max}}{A_d}$$

where $P_{\max}$ is the maximum load applied, and A_d is the displacement area [43].

The evolution of load P and depth h, during loading and unloading, is also useful: the stiffness S of the material can be obtained from the tangential of the unloading curve, i.e. dP/dh. From this information, other mechanical properties can be calculated, such as the Young's modulus and elastic recovery [6,43,44].

The indentation technique is limited by the thickness of the material, so nanoindentation, which is essentially the same technique using small loads and depths, has become the predominant technique for hardness measurement of thin films [6]. The hardness values used in this work were always calculated from the average of at least 10 such measurements in 2 different locations on the surface of the coating. The equipment used was Micro Materials' NanoTest system.

2.4.3 Scratch test

Scratch tests were primarily dedicated to evaluate the adhesion of coatings to the substrates. The basic principle of the scratch test is to put an indenter (a hard diamond tip) in contact with the surface of the coating, apply a load to the indenter, and examine whether it causes the coating to present any failure (cracks, delamination, detachment from the substrate, etc.) The results referred to in this study, unless stated otherwise, were obtained with a CSM Instruments Revetest Scratch Tester by progressive load scratch test (PLST). In this type of test, the load increased linearly while the indenter moved across the surface at a rate of 10 N/mm. The scratches were then analysed under optical microscope and three-dimensional profilometer. The critical load is determined as the load at which adhesive or cohesive failures start to occur in the coating. Since local heterogeneities in the coating may contribute to the occurrence of such failures, the values of critical load presented here were averaged from a number of scratch tests (between 2 and 4) performed in different places. Another possible type of test is the constant load scratch test (CLST), in which several scratches are made under constant load at different locations on the coating. For each new scratch, the load is increased by one step [45].

It should be noted that a coating's behaviour during scratch test cannot be easily compared to other situations, under different geometries or types of loading, and quantitative values are representative only of the particular type of test from which they are obtained [6,46]. In particular, the conditions of the scratch tests in this work were rather different from those of the tribological tests. The scratch tests under same conditions allowed a first comparison between the adhesion of different coatings, but their results could not be translated directly into tribological tests.

2.4.4 Ball-cratering test

The main method for evaluating the thickness of the coatings was the ball-cratering test (also called *calotest*). It consists in rotating a steel ball with known diameter in contact with the coating. An abrasive solution is added to the contact area. This results in a depression on the contacted area in the shape of a spherical cap. If the test is long enough, the ball wears through the coating and reaches the substrate, so that the spherical cap is deep enough to wear the substrate as well. From a simple visual analysis of the worn cap, the thickness t of the coating can be calculated. This calculation is an approximation based on the assumption that the crater is much smaller than the radius of the ball. Using the parameters shown Fig. 2.4, the thickness is:

$$t=\frac{x\cdot y}{D}$$

Ball-cratering tests were carried out using a CSM Instruments industrial Calotest. Measurements were compared, when possible, with other values of thickness obtained from profilometry (in regions where the substrate was exposed) and SEM of cross-sections.

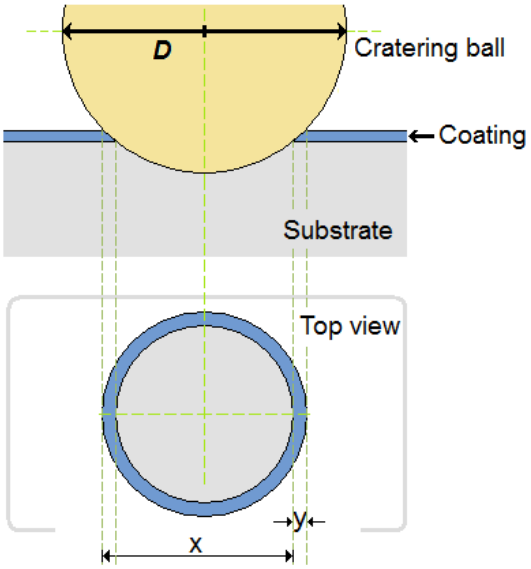

Fig. 2.4 Schematic of a ball-cratering test (adapted from [47]).

2.4.5 Sliding tests

Tribological tests were performed using a standard CSM Instruments pin-on-disc tribometer. In such an equipment, the sample is fixed on a planar support which rotates around a single axis (ideally; in practice, the surface of the sample may not be perfectly horizontal, and therefore a given point rises and descends periodically while the sample rotates). The pin is mounted on a lever and placed in contact with the sample, and a controlled load is applied on it (as illustrated in Fig. 2.5). The friction coefficient μ can then be determined by measuring the horizontal displacement of the lever arm. Its dimensionless value is given by

$$\mu=F/N$$

where F is the frictional force, parallel to the sliding, and N is the normal force, exerted by the load. In our tests, the friction coefficient was recorded with a frequency of 20 Hz – except when the rotation speed was lowered to acquire video recordings (see Chapter 6), in which cases the sampling

frequency was also lower. The values of μ used in this work, unless stated otherwise, were the mean values for the entire tests.

Despite the name, the *pin* can be of different shapes. Usually, a ball is used because of its simple geometry. In this work, all pin-on-disc tests were performed using 100Cr6 steel balls (with a diameter of 6 mm unless where noted) as static partners against the surface of the coated sample.

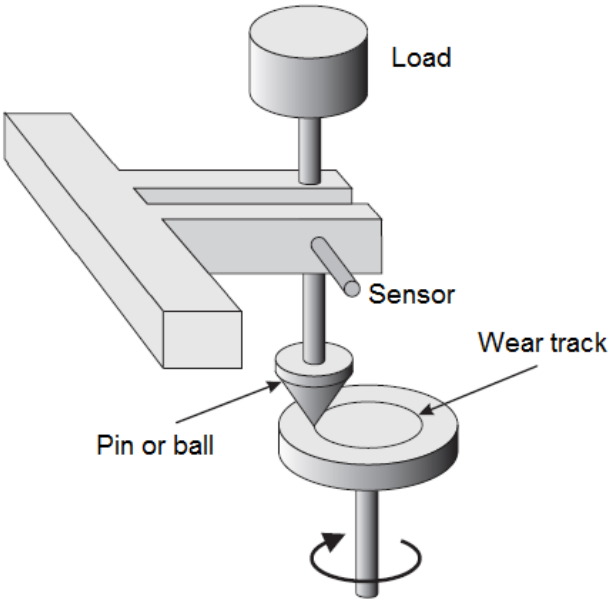

Fig. 2.5 Schematic of a pin-on-disc tribometer (adapted from [39]).

Several results can be obtained from the wear tracks produced during sliding tests, besides the friction coefficient. Wear rates can be calculated by

$$k = \frac{V}{S.L},$$

where k is the wear rate, V the worn volume, S the total running distance of the sliding, and L the load [33]; and are usually expressed in $mm^3/N{\cdot}m$ – unit of volume per unit of load per distance. The total length of the test can be calculated simply from the perimeter of the wear track multiplied by the number of cycles in the test. By measuring the area of the cross section of the wear track and multiplying it by the length of the track, the total worn volume is found [43]. In our experiments, this was usually done by measuring the cross section in four different locations in the wear track, by three-dimensional optical profilometry described below, and calculating the average cross-section area. The wear rates of the static partners were calculated similarly, by measuring the worn spherical cap and thus determining the worn volume.

2.4.6 Three-dimensional optical profilometry

The three-dimensional optical profilometer is based on white-light interferometry. In this technique, a light beam is reflected on the surface of the sample, detected and compared with a reference beam (which can be generated from the same source and separated from the beam that will reach the sample by a beam splitter). The topology of the sample will cause different path lengths of the reflected beam, which will cause different interference patterns to appear when the beams are combined and thus it is possible to characterise the topography of the surface. White-light interferometry makes use of the fact that the beam carries interference information in different wavelengths to achieve better resolution [41,48]. In the profilometer used in this study, a Zygo NewView 7200, the vertical resolution was of less than 0.1 nm, while the lateral resolution could be of as little as 0.52 μm [49]. The data were acquired for a field of vision of up to 1.40 × 1.05 mm, but it was possible to combine data from different measurements, of adjacent areas, to compose a larger 3D profile. Vertically, topological features of up to 200 μm could be measured.

The main limitation when performing profilometry of TMD coatings was the sensitivity to the reflected light. If the light intensity was too low, the device could not retrieve enough information about the surface. On the other hand, if the reflected light was too strong, the measurement saturated and again no useful data were retrieved. In many situations, it was impossible to measure the full profile of the surface when, for example, the wear debris was too opaque (low reflectance) at the same time as the wear track was too reflective (high reflectance). In such cases, part of the data was inevitably lost.

2.4.7 Raman spectroscopy

Raman spectroscopy is a non-destructive characterisation technique based on Raman scattering. The sample is irradiated by laser beams in the UV–visible range. The scattered light can be of two types: it may be elastically scattered, i.e. the scattered photons have the same wavelength as the incident beam (Rayleigh scattering); or the scattered photons can have lower or higher energy than the incident beam (meaning that energy was absorbed or lost by the sample). In the second case, the effect is known as Raman scattering.

If the sample is irradiated by monochromatic light of frequency ν_0, the Raman-scattered light will have frequencies $\nu_0 \pm \nu_m$ where ν_m denotes a vibrational frequency of a molecule [50]. The positive or negative sign will depend on the interaction of the incident light with the sample; if the

material absorbs energy, the scattered light will have energy $\nu_0 - \nu_m$, lower than the incident beam. If the material loses energy, the scattered light will have energy $\nu_0 + \nu_m$, higher than the incident beam. These two cases of Raman scattering are referred to as Stokes and anti-Stokes, respectively. The shifts in wavelength correspond to the excitation of molecular vibration modes or crystal phonons. They can be used for identification of substances, since they are specific for a material [51]. Raman scattering is usually a very weak phenomenon and it is challenging to achieve high sensitivity. The equipment must have a low-noise detector, and high laser intensity is usually better. However, high laser power may cause structural changes in the tested material, so the measurement parameters need to be adjusted to avoid it [50,51]. In practice, the acquisition time can be increased to compensate for low power, but this increases noise and the probability of interference by cosmic rays, which cause high-intensity narrow spikes to appear in the spectrum [52].

The optical mechanisms in the spectrometer allow the data to be collected by the same objective through which the laser beam reaches the sample. Fig. 2.6 shows a schematic configuration of a Raman spectrometer, where *BR* is a band-rejection filter which blocks the elastically scattered radiation, and the *detector* block includes implicit optical structures, such as an entrance slit to reduce stray radiation.

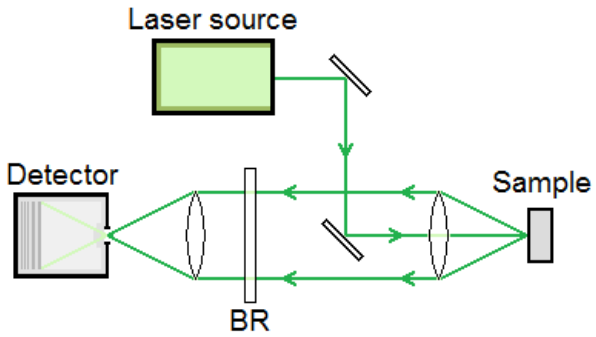

Fig. 2.6 Schematic of Raman spectrometer (adapted from [51]).

Associated with other analyses, Raman spectroscopy helped evaluate several properties of the deposited films. The appearance of characteristic peaks in the spectra helped evaluate the ratios of certain materials in the sample. Additionally, Raman spectra conveyed information regarding the crystallinity of the material, since more amorphous materials exhibited comparatively broader peaks. Raman spectroscopy was performed on a Horiba XploRA Raman microscope with DPSS of wavelength 532 nm.

2.4.8 Scanning electron microscopy (SEM)

Scanning electron microscopy is a technique of surface characterisation in which an electron beam is focused on the material and the signals resulting from the interaction of the beam with the surface are recorded. It allows imaging of the topography of the sample's surface with lateral resolution in the order of a few nanometers [39]. The electrons typically have energy of up to 30 keV [41] and the beam is finely focused by an electromagnetic field (or electromagnetic condenser lens). The probe (i.e. the focused beam) scans the surface of the sample, so the system acquires data sequentially, one point after another, in a pattern that is called *television raster*: the probe passes over all points in a line, then returns to the start, moves to the next line, and starts again. The image formed is thus called a *scanning image*, as opposed to an *optical image*, where the data is collected for the whole field of view at once.

The microstructural information collected by the system is provided mainly by the inelastic scattering processes occurring due to the interaction between probe and surface. The major source of data is usually secondary electrons emitted when the electron beam hits the surface, therefore it should be of little importance for the technique if the beam goes through the sample, even though it may reach the substrate [39,41]. The secondary electrons have low energies, so only those close to the surface are detected. Placing the sample in vacuum avoids their scattering by gas molecules, improving the measurements.

SEM measurements presented in this work were carried out using a Philips XL30 scanning electron microscope, in two different ways: either perpendicular to the direction of film growth, therefore analysing the morphology of a cross-section of the coating; or on the surface, to evaluate its topography. The cross-section measurements helped verify the compactness and amorphous characteristic of the films, while the microscopy on the surface helped analyse wear tracks and surface defects.

Besides the morphology, a range of signals can be acquired from the interaction of the beam with the sample to obtain other data, such as the characteristic X-rays emitted by the excitation of inner shell electrons. They are the basis of the analysis called *Energy Dispersive X-ray* spectroscopy (EDX or EDS), also used to evaluate the composition of the material, similarly to the EPMA described earlier. EDX data presented in this work were acquired by the same equipment as SEM data. Back-scattered electrons (i.e. electrons originating from the beam that are scattered back and can be detected) convey information about composition as well, due to the dependence of the number of back-scattered electrons to the density of the specimen – or more

specifically, to the atomic number of the atoms in it. Thus, back-scattered electrons can be used to determine local atomic number contrast, enabling distinction between different phases in the material [41].

2.4.9 Transmission electron microscopy (TEM)

Transmission electron microscopy works similarly to SEM, but the electron beam goes through the sample, which must be thin enough (typically below 0.1 μm [41]) for the electrons to pass without serious energy loss. If the beam is emitted from above the specimen, the information is collected below. The electron beam in TEM has higher energy, typically between 100 and 400 keV resulting in resolution high enough to image planes in a crystal lattice. The information is acquired from the primary electrons emitted by the beam and their elastic collisions with the sample. Therefore, this is not a surface characterisation technique, although the small thickness of the sample means that the results obtained with this method are very sensitive to surface characteristics. Since the electrons detected are all supposedly emitted with same energy and same acceleration, the resulting image is directly related with the material structure [39]. Contrary to SEM, the data is collected over the full field of view, forming an optical image.

This technique allows acquisition of the objects in real space as well as in reciprocal space, via the electron diffraction patterns. By collecting data closer to the sample, at the back focal plane instead of the image plane, a diffraction pattern is generated. It appears as a pattern of dots for single-crystal structures, or circles for amorphous materials [41].

The equipment used in this study was a Tecnai G2 transmission electron microscope.

2.4.10 X-ray diffraction (XRD)

When radiation incident on a material has a wavelength comparable to the size of its geometrical variations (the interatomic spacing of crystals), certain diffraction effects can be observed. X-rays with wavelength ≈ 0.1 nm can be used in this way to acquire information about the crystal lattice of a material [41,53]. The relevant phenomena for XRD are the elastic scattering of X-rays by the atomic structure, whereby the radiation wavelength λ is not altered. When the X-ray beam hits a crystalline structure, the reflected rays on the surface may interfere constructively or destructively with the rays reflected from layers below. The intensity of the outgoing rays, therefore, will depend

on three factors: the wavelength of the X-rays; the angle of incidence; and the distance between the planes. The condition for constructive interference is determined by Bragg's law:

$$n\lambda=2d\sin\theta$$

where n is an integer, λ is the wavelength of the radiation, d is the distance between the planes responsible for reflecting the beam, and θ is the angle between the incident radiation and the planes of the lattice, as shown in Fig. 2.7. The use of Bragg's equation requires several assumptions, such as the absence of absorption of energy by the lattice, thermal vibration, etc. Nonetheless, it is a good approximation to explain the results obtained with XRD [53].

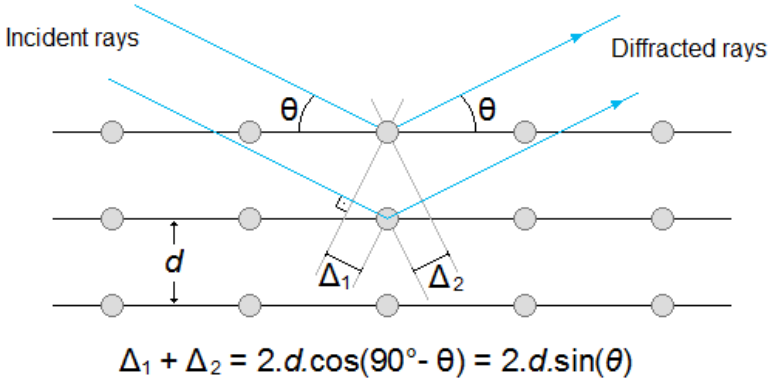

Fig. 2.7 Illustration of Bragg's law (adapted from [53]).

For XRD analysis, the radiation reaches the surface at varying incidence angles, and the intensity of the diffracted rays is measured for the whole range, recorded and plotted for a continuous range of incidence angles 2θ. The source of radiation, as well as the detector, must be kept at a fixed distance from the sample, to ensure that intensity variations result from interference caused by the sample geometry. In an X-ray diffractometer, the detector and the source must be at the same angle relative to the sample. In practice, this can be achieved by various methods – for example, if both the source and the detector move along a semicircle with the sample in the centre; or with the source fixed while the detector rotates around the sample, which itself rotates around a central axis [41,53]. An alternative configuration called *grazing incidence* uses very small incidence angles to acquire depth-resolved structural information [53], as well as to limit the penetration depth of the X-ray beam (in the case of thin films, it is possible that the substrate influences the spectra since X-rays can penetrate several microns into the sample [39]).

The data obtained from XRD spectra also convey other information about the structure

of the material. Small grain sizes and crystal lattice faults, as well as randomly-oriented grains, cause broad peaks in the spectra (as opposed to sharp, intense peaks resulting from single-crystal and preferentially-oriented structures) [53]. Additionally, the shift in the diffraction angle for known orientations is indicative (assuming the measurement is accurate) of mechanical stresses in the material: a small compression or tension in the grains will change their crystal lattice slightly, and this shifts the position of the peaks to lower (for compressive stress) or higher (for tensile stress) angle values [41,54,55].

The equipment used for most XRD measurements in this work was a Philips X'Pert diffractometer with Co(Kα) radiation (λ = 0.179 nm).

2.4.11 X-ray photoelectron spectroscopy (XPS)

XPS is also based on exposing the sample to X-rays, typically of energy higher than 1 keV [39]. The monochromatic photons in the incident beam are absorbed by the atoms in the sample, which ejects secondary electrons with energy equal to the difference between the energy of the incident photon and the energy needed to displace the secondary electron. The secondary electrons are detected, and the intensity of the signal over a range of corresponding binding energies composes the XPS spectrum. The excitation by X-rays may also cause energy transitions within the atom that lead to emission of Auger electrons, which also appear in the spectra but are not the main concern of XPS. Electrons emitted in layers deep within the material have small chance of reaching the surface and being detected, so this technique characterises only the few uppermost atomic layers [39,41]. Consequently, surface contamination influence the results very strongly, and usually the sample is sputtered with argon ions prior to measurement. Sputter-cleaning can lead to preferential removal of lighter elements in the material, which needs to be taken into account when analysing the results.

Since electrons are emitted from the inner shells, and different elements have different electronic binding energies, XPS can be used for elemental analysis. Nevertheless, changes in the chemical environment of the atom will influence the binding energy, so that photoelectronic emission from the same element in different binding states will generate (slightly) different peaks. (As a rule, binding with elements of higher electronegativity will shift the peaks to higher binding energy values.) Therefore, the technique is also useful for analysing chemical bonding [41,51], its main use in this work.

3 Mo–S–C (molybdenum disulfide doped with carbon)

Part of the content in this Chapter has been published in the paper:

> J.V. Pimentel, T. Polcar, and A. Cavaleiro, "Structural, mechanical and tribological properties of Mo-S-C solid lubricant coating", *Surface and Coatings Technology* vol. 205 (2011), pp. 3274-3279.

A series of Mo-S-C films with varying carbon content had been previously deposited at the Department of Mechanical Engineering, University of Coimbra, Portugal; its characterisation is part of this study. The films were deposited by r.f. magnetron co-sputtering from two targets, MoS_2 and C (graphite). The varying composition was achieved by varying the power applied to each target. The sputtering yield of MoS_2 is much higher than that of C, so the deposition rate decreased as the power ratio P_C/P_{MoS2} increased; as expected, the carbon content increased almost linearly with the power ratio, as shown in Fig. 3.1. Due to limitations of the deposition process (target heating limiting power to C target and minimum power required for MoS_2 target), the C content in the series could not be higher than 55 at.%. The S/Mo ratio in the composition did not show any direct relation to the power ratio. Chemical composition and power ratios are listed in Table 1. The characterisation of the films was carried out using the methods and equipment described above.

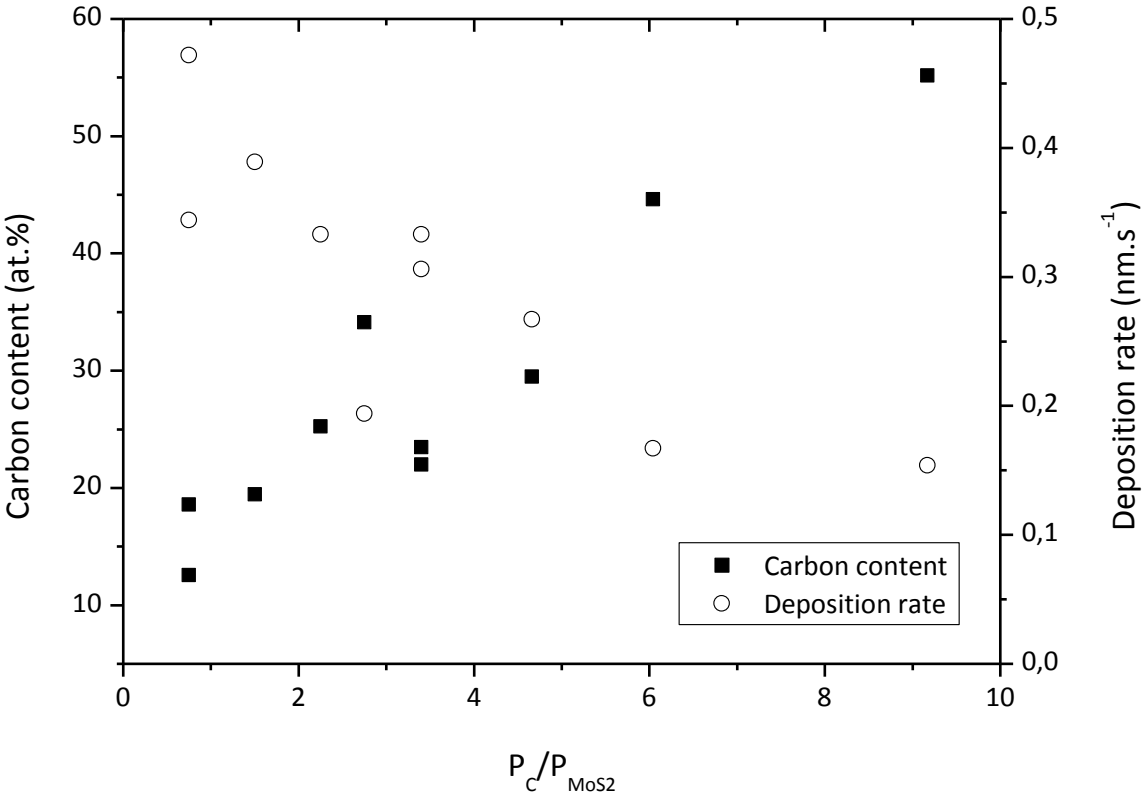

Fig. 3.1 Carbon content and deposition rate as a function of C/MoS_2 target power ratio.

Table 1 Deposition parameters, chemical composition and thickness of Mo-S-C coatings.

Target power		C/MoS_2 power ratio	Chemical composition (at.%)			Coating thickness (µm)
C	MoS_2		C	Mo	S	
0	200	--	2	37	61	3.8
150	200	0.75	13	35	52	3.1
150	200	0.75	18	30	52	3.4
300	200	1.50	20	30	50	3.6
450	200	2.25	25	31	44	2.9
550	200	2.75	34	26	40	2.1
550	162	3.40	23	34	43	2.2
550	118	4.66	30	28	42	2.4
550	91	6.04	45	21	34	1.8
550	60	9.17	55	17	28	1.2

Strong surface oxidation was typical of Mo-S-C films, not only in the instrumental analyses above but also visually: the coatings, metallic black after deposition, changed to a dark grey after several weeks. SEM observation of the surface, about three months after deposition, revealed small bubble-like structures, with diameter between 200–800 nm (Fig. 3.2). EDX analysis showed that they were composed of MoO_3. This oxidation layer could be easily removed with soft materials, such as cotton-wool, but was rebuilt after several days.

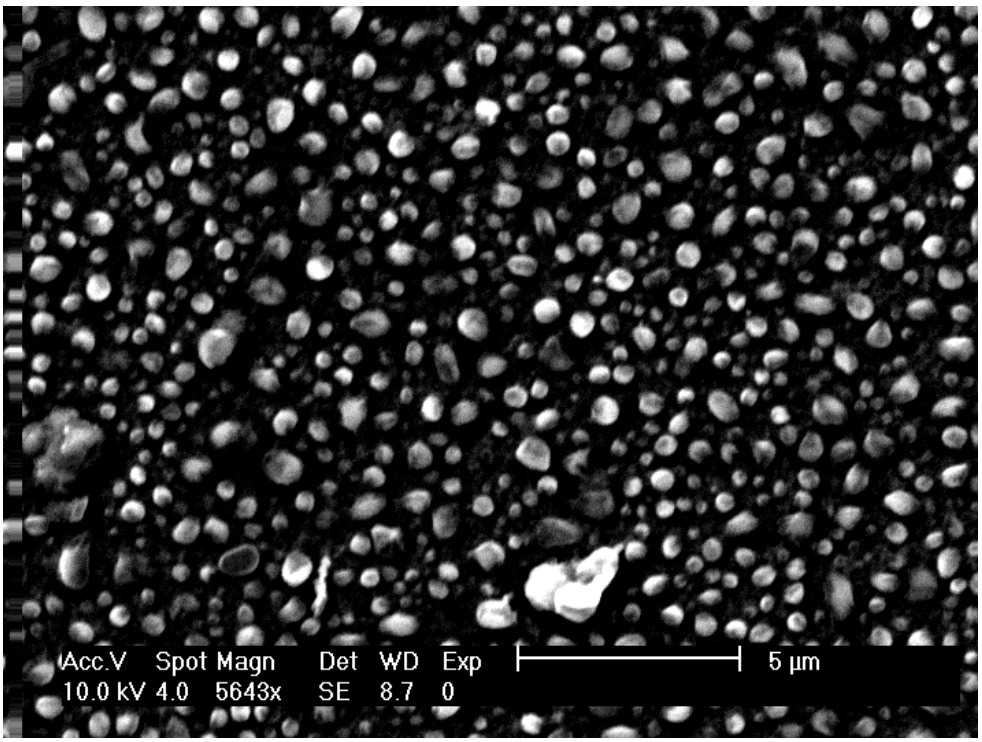

Fig. 3.2 SEM micrograph of oxidized surface of a Mo-S-C coating (18 at.% C).

The characterisation and testing of the films and the wear tracks was mainly focused on verification of the self-lubricant characteristic of the coatings and the effect of carbon content on tribological properties. Hardness values showed and almost linear increase with carbon content, from 0.7 to 4 GPa; the films were therefore harder than the reference pure MoS_2 (hardness 0.3 GPa). Tribological tests were performed in humid air and in dry nitrogen. The equipment did not allow perfect environmental isolation, so the nitrogen was actually mixed with humid air, and the tests started when the relative humidity (RH) stabilized at approximately 5%. The load in tests in dry nitrogen was 5 N, whereas several loads up to 30 N were used in humid air.

3.1 Analysis of chemical bonding and structure

XPS was used to analyse the surfaces as well as the material a few nanometers below, exposed after etching with Ar^+ ions for 5 or 10 minutes. The results showed strong oxidation on the surface, as evidenced by the peaks at binding energy (BE) ≈ 236.2 eV, attributed to MoO_3 [56], which were practically non-existent after etching. The dominant peaks in the Mo3*d* region corresponded to MoS_2 at binding energy 229.7 eV [57]. The small peaks at BE ≈ 226.7 eV were identified as possible molybdenum carbide according to Ref. [58]. The existence of Mo–C bonds was confirmed in the C1*s* spectra; the dominant peak corresponded to C–C bonds (at 284.4 eV) and a small shoulder appeared at BE ≈ 283.3 eV, the typical value for Mo–C bonds [59,60]. After etching and the elimination of Mo–O peaks, the relative intensity of Mo–S peaks increased, while that of Mo–C peaks decreased. This suggests that the molybdenum carbide phase resisted surface oxidation better than the MoS_2 phase at room temperature. In the S2*p* region, a peak was observed at 168.8 eV (the position of SO_2 [61]), which indicated that sulfur in the MoS_2 structure could be found in an oxygen environment, since the actual existence of SO_2 molecules in the material was highly unlikely. A weak peak corresponding to Mo–O bonds [62] was still observed in the O1*s* region, even after etching. It appears that the oxygen incorporated into the coating by contamination during and after deposition was bonded almost exclusively to molybdenum.

In XRD spectra, the main feature was the intense peak at 38°, corresponding to the (100) orientation of the hexagonal phase of MoS_2, superposed on an asymmetric broad peak which corresponded to the turbostratic stacking of (10*L*) planes, where $L = 0,1,2\ldots$, as observed by Lévy et al. for WS_2 and MoS_2 [63,64]. The shoulder in the spectra of the present Mo–S–C films was extended well above 50°, including the peaks at approximately 39° (101), 42° (102), 46° (103) and 52° (104). Besides these features, weaker MoS_2 peaks were visible, corresponding to (002) at $2\theta \approx 16.8°$, and (110) at 69°. The presence of molybdenum carbide could not be identified due to its positions overlapping with the observed peaks; moreover, the carbide grains (if present) should be very small.

In the Raman spectra of the films, there were two evident pairs of peaks, the first corresponding to vibrational modes of MoS_2 at approx. 370cm^{-1} ($E_{2g}{}^{(1)}$) and 410 cm^{-1} (A_{1g}) [65], and the second to the D and G peaks of carbon (at approx. 1420 and 1560 cm^{-1}) that usually appear in the spectra of sputtered carbon-based coatings [66,67]. The ratio of the peak areas I_C/I_{MoS2} showed a direct relation to the ratio of deposition powers, P_C/P_{MoS2}. Fig. 3.3 shows Raman spectra for

different carbon content and the relation between power ratio and peak ratio (in the inset). It can be seen that the MoS_2 peaks became broader for higher C content, which is an evidence of more amorphous structure. The increase of C content from 30 to 55 at.% did not significantly alter the D and G peaks, which would be an indication of structural changes in the carbon matrix [66–68]. In some spectra a very low and broad peak could be observed at approx. 820 cm^{-1}, which was identified as MoO_3.

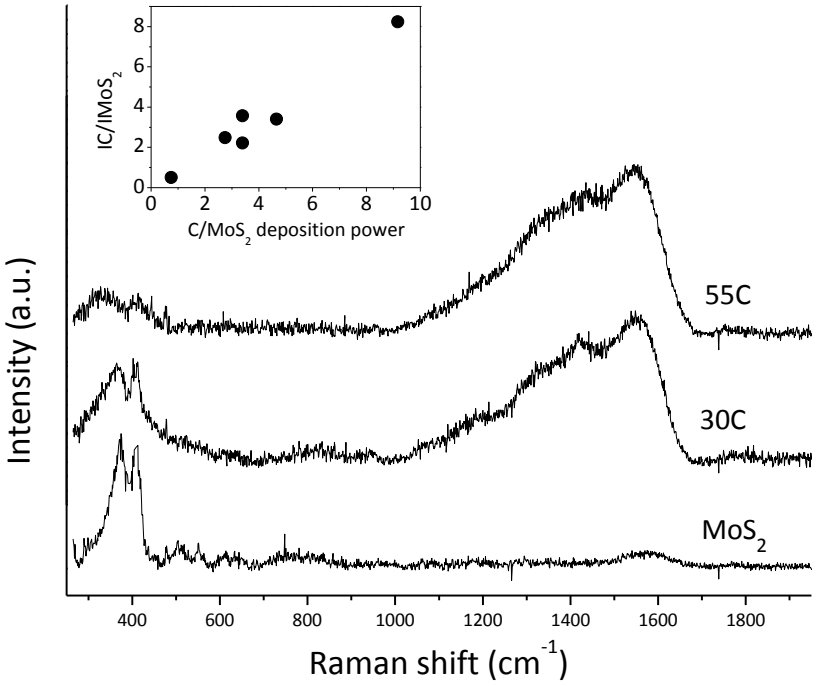

Fig. 3.3 Selected Raman spectra of Mo-S-C films.

3.2 Tribological properties

For low carbon content (below 30 at.%), the running-in process was characterised by high friction, which later decreased to lower stable values. The trends differed in high carbon content coatings: the one with 34 at.% C showed hardly any increase at all, reaching low friction values in the very first laps which were maintained throughout the tests. The coating with 55 at.% C achieved low friction very quickly, which then increased slowly until stabilizing. In Fig. 3.4 are shown friction curves for different compositions under the same conditions. The coating with the highest carbon content showed the lowest friction and the lowest wear rates for both the coating and the

counterpart. There was a wide variation of wear rates among the different compositions, from 0.28×10^{-6} to 16.6×10^{-6} mm^3/Nm (for coatings with 55 and 23 at.% C, respectively), with ball wear rates being one or more orders of magnitude lower.

Increasing load led to lower friction coefficients, as expected for TMD-based films: the contact pressure during sliding should promote the orientation of the material close to the surface and the formation of a tribolayer, as referred to in Chapter 2. It is interesting to note that a coating composed only of amorphous carbon typically exhibits the opposite trend (i.e. higher friction for higher load [35]), which already suggests that the frictional behaviour in the Mo-S-C films is determined mostly by the properties of MoS_2. The values of friction coefficient obtained (Fig. 3.5) fit a logarithmic relation reasonably well. Polcar et al. [34] proposed the equation $\mu = AL^B$ to describe the dependence of friction with contact load (L) for W-S-C films deposited by r.f. magnetron sputtering. In the equation, the constant A relates to the material and contact conditions; B relates to the length of the test, in particular the changes in the coating and formation of a third body due to repeated laps.

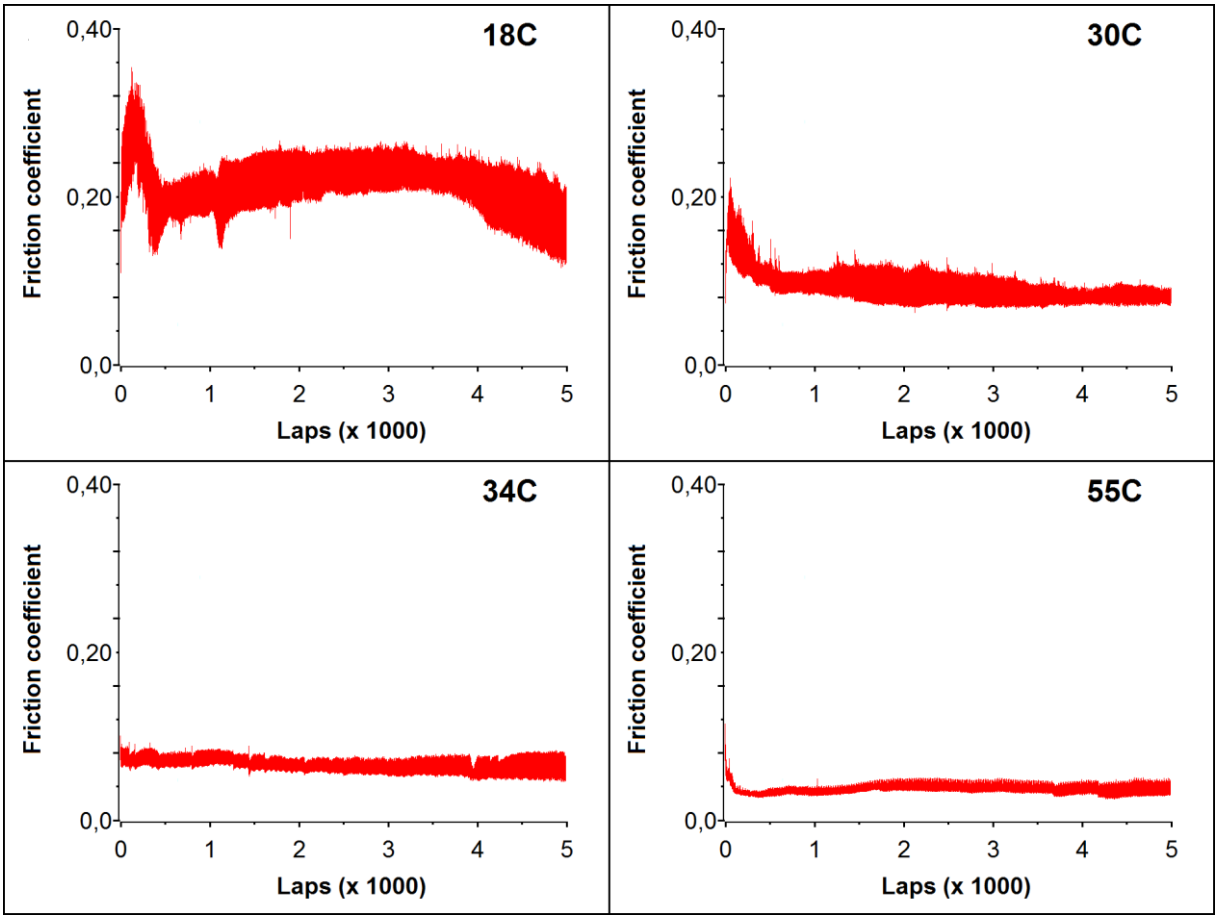

Fig. 3.4 Selected friction curves for different compositions of Mo-S-C under 18 N in humid air.

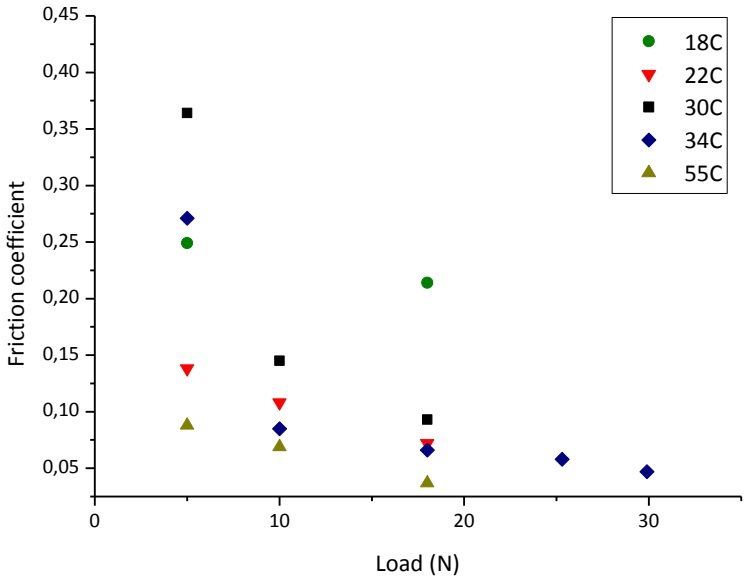

Fig. 3.5 Friction coefficient versus contact load for tests in humid air.

Raman spectra measured in different positions in the wear tracks showed almost identical peaks, contrary to other results such as for the W–S–C films presented in Chapter 4 of this work. It indicated that the tribolayer was very thin, and sub-surface reorientation (which would result in sharper peaks) was very limited or did not occur.

The coatings showed relatively low adhesion, and in some cases adhesion failures occurring during sliding probably led to higher friction and wear. It should be noted, however, that these failures did not provoke immediate increase of friction due to the self-lubricating characteristic of the films and material attached to the ball still maintained the lubrication function. EDX performed on the counterpart showed that the adhered tribolayer in the centre of the ball was very thin, but wear debris composed of Mo-S-C was found to be accumulated behind the wear scar. SEM micrographs of the wear track showed a very smooth surface with mild scratches.

Sliding in dry N resulted in very low friction coefficients, which were reached very quickly and stayed stable for the entire tests. There was no significant variation of friction or wear with carbon content above 18 at.%. The wear tracks produced in dry N for medium and high carbon content were even difficult to measure, since the worn volume was very low (as can be seen in Fig. 3.6). The values obtained in tribological tests in dry nitrogen were comparable to results in the literature [11,69,70], and Mo-S-C films clearly outperformed pure MoS_2.

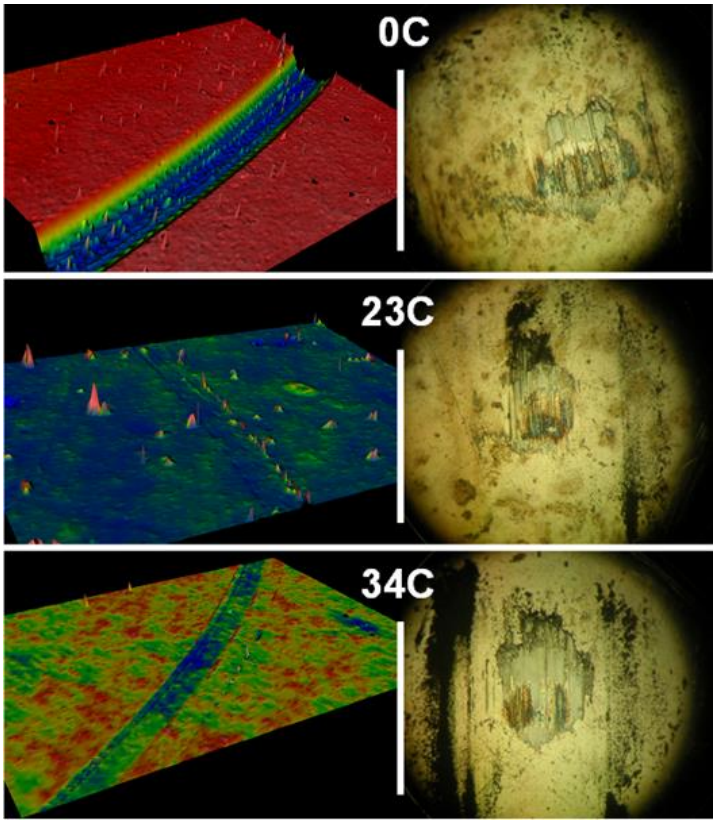

Fig. 3.6 3D images of wear tracks (left) and optical images of the ball wear scars (right), for reference Mo-S (0C) and Mo-S-C coatings with 23 and 34 at.% C, after sliding in dry N.

4 W–S–C (tungsten disulfide doped with carbon)

Part of the content in this Chapter has been published in the paper:

> J.V. Pimentel, T. Polcar, M Evaristo, and A. Cavaleiro, "Examination of the tribolayer formation of a self-lubricant W–S–C sputtered coating", *Tribology International* vol. 47 (2012), pp. 188-193.

A series of tungsten disulfide coatings alloyed with carbon was deposited by d.c. magnetron co-sputtering from two targets, WS_2 and graphite. From that series, one composition was characterised and analysed as part of this study. This series was based on promising results from depositions of W-S-C films by r.f. magnetron sputtering, either in Ar/CH_4 atmosphere [32,33,71] or using pellets of WS_2 placed on the erosion zone [34,35]. The second approach was deemed more successful due to elimination of hydrogen contamination, exhibiting good tribological performance. Its highest hardness was achieved for carbon content of approximately 40 at.%.

The composition chosen from the series deposited by d.c. magnetron sputtering for characterisation and tribological testing was one with a carbon content of 42 at.% and an S/W rate of 1.26. The coatings were deposited by co-sputtering a WS_2 target and a C target, with power ratio $P_{WS2}/P_C = 1.9$. They were approximately 2.4 μm thick, with hardness of 9 GPa. The adhesion was sufficient for tribological tests, with critical load measured by scratch test higher than 9 N, an improvement compared to pure WS_2 films [71].

All tribological tests were performed in humid air (relative humidity 30%) using 100Cr6

steel balls with a diameter of 6 mm, cleaned with acetone prior to the start of the test. The linear speed was 10 cm/s. Three main sets of tests were performed: in one set, all tests were carried out for 5000 cycles, each test with a different contact load, in the range 1.0–50.8 N. In another set of tests, the load was kept constant, but the number of cycles varied from 100 up to 50000.

The third set was actually a special procedure during a single tribological test. In order to better understand how the friction mechanisms evolve during sliding, the rotation of the sample was paused every few laps and Raman spectroscopy was performed in the wear track. This required an external lens connected to the Raman spectrometer via optical fiber. The test configuration was not demounted and the sliding continued after the spectrum had been acquired. After a few more laps, it was paused again, and Raman spectrum was acquired again. In such a way we could consider Raman spectra as a *quasi in-situ* identification of the structural changes in the wear track.

4.1 Friction and wear behaviour

The friction coefficient was lower than 0.2 for all of the conditions described. The set of tests with varying load permitted a qualitative and quantitative analysis of the influence of the contact pressure. The friction coefficient μ decreased with increasing load according to the equation $\mu = AL^B$ described earlier. In the present case, the experimental data for the friction coefficient fit the equation well with $A = 0.19$ and $B = -0.46$, as shown in Fig. 4.1 (note the logarithmic scale).

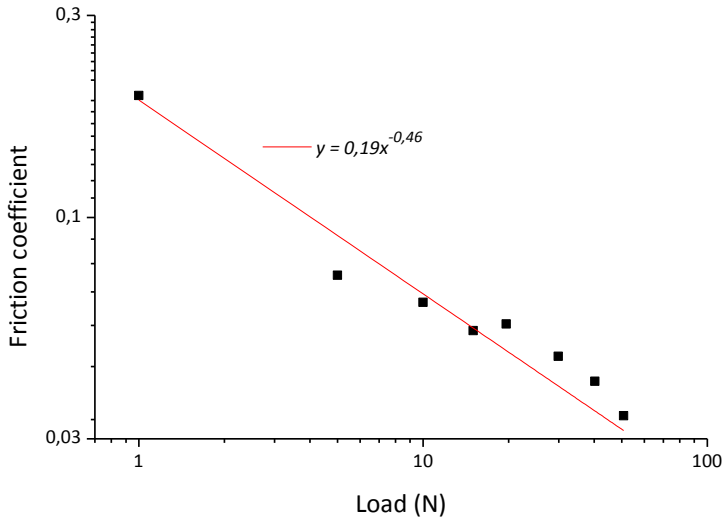

Fig. 4.1 Friction coefficient versus contact load.

The wear rate of the coatings was low and also decreased with load (although the worn volume increased), as shown in Fig. 4.2. Analyses of the wear tracks by SEM and 3D profilometry showed that the wear tracks produced by lower loads were smooth and shallow. For higher loads, however, they became rough and deeper (see Fig. 4.3).

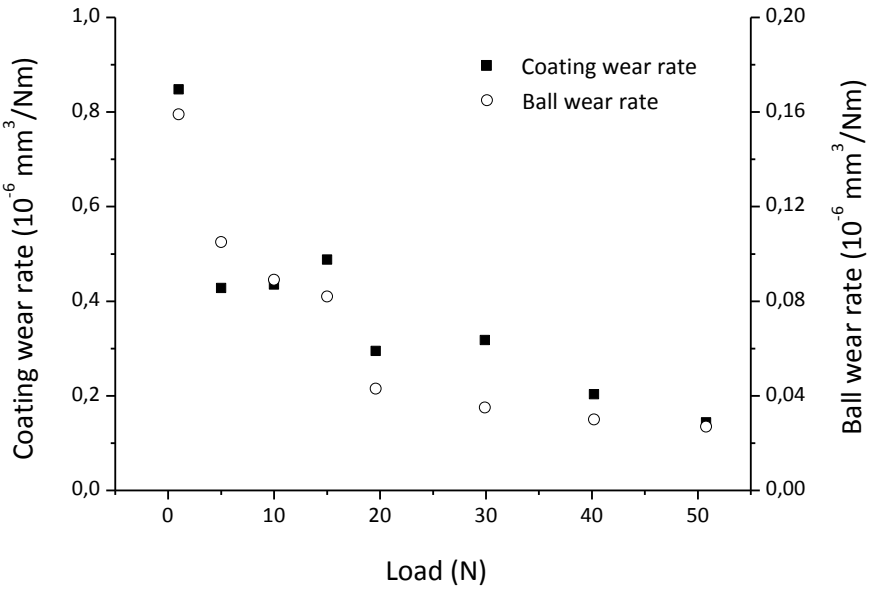

Fig. 4.2 Wear rate versus load.

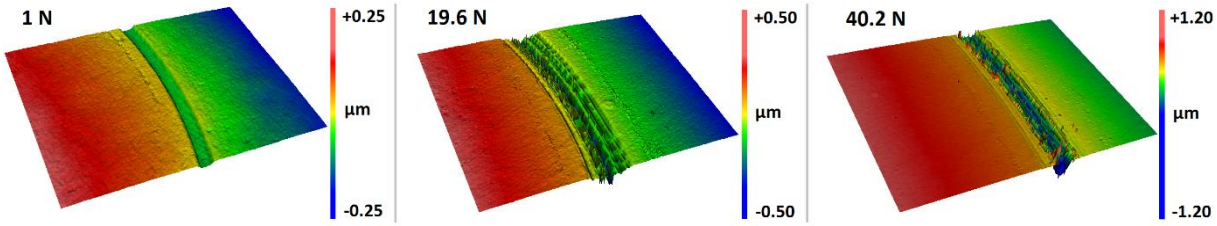

Fig. 4.3 3D profiles of wear tracks produced under different loads.

Observation of the frictional behaviour during run-in showed that high values of μ occurred in the first couples of laps, then the friction dropped to a lower level, and afterwards stabilized in a steady-state regime. Tests with varying load revealed that this stabilization happened much faster for higher loads, as can be seen in the comparison shown in Fig. 4.4. Moreover, by increasing the length of sliding tests it was possible to observe that the friction coefficient remained constant in the steady state till approximately 10 000 laps, where it started to increase. Fig. 4.5 shows the friction coefficients for tests with different durations.

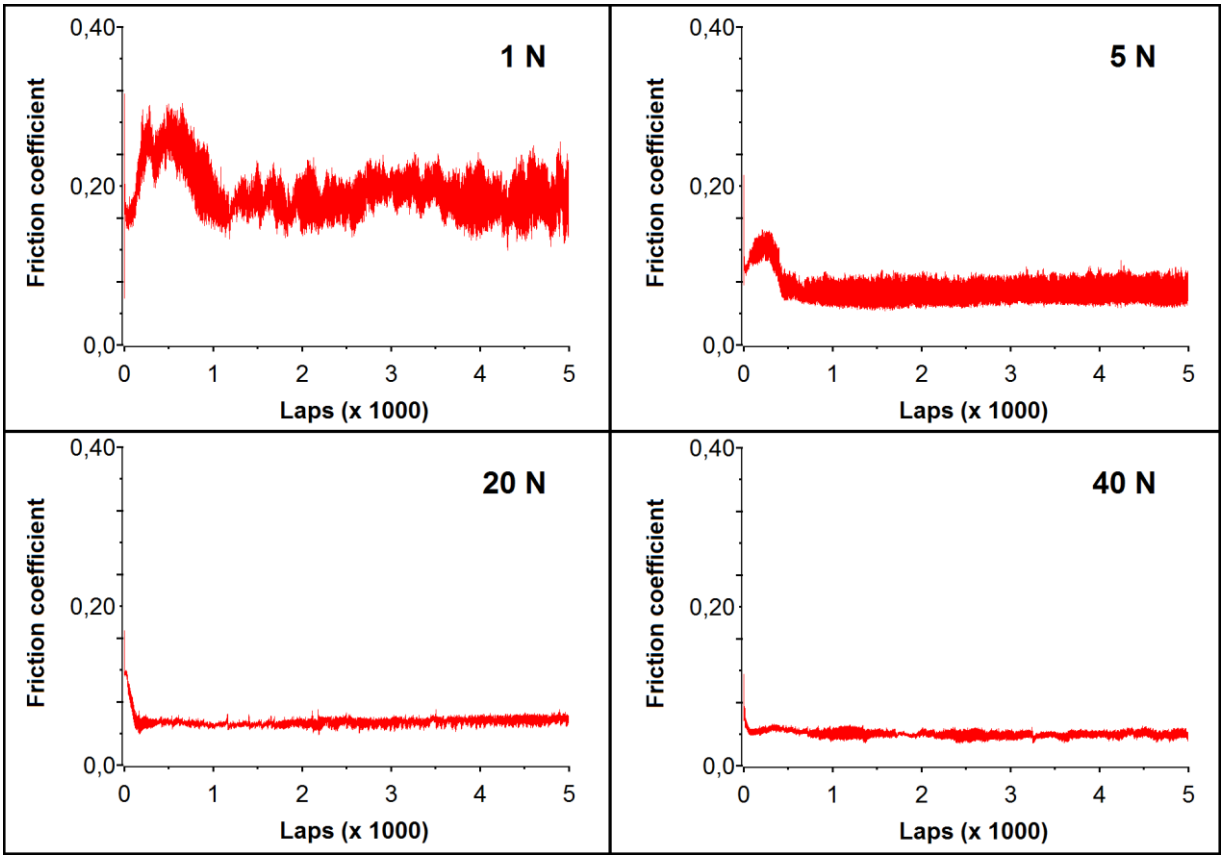

Fig. 4.4 Selected friction curves from sliding tests under different loads.

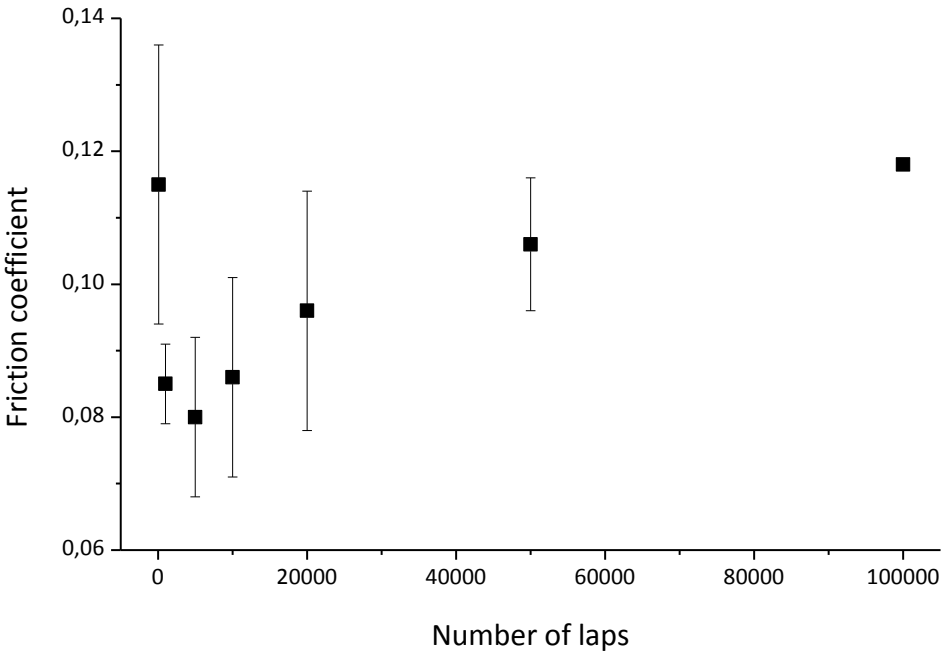

Fig. 4.5 Friction coefficient from tests with different number of cycles.

4.2 Structural analysis by X-ray microdiffraction

X-ray microdiffraction was aimed at the structural analysis of as-deposited surface and two wear tracks, produced by sliding under different loads (20.9 and 40.2 N). The measurement on the wear tracks was intended to verify whether significant structural changes caused by sliding could be observed. There were two predominant features in the XRD spectra acquired (shown in Fig. 4.6): first, the intense, sharp peaks that appear at $2\theta \approx 45°$ and smaller peaks to the left. These originated from the substrate and were not particularly relevant to our analysis. The second dominant feature in the spectra was the broad peak at $2\theta \approx 34°$ showing a broad shoulder to higher 2θ values, indicating a turbostratic stacking of (10*L*) planes [63,64]. The spectra could not be used to identify the presence of carbides in this case either, since the position of tungsten carbide peaks would overlap with those associated with the (10*L*) planes of WS_2, especially since small grain sizes would be expected [31,72].

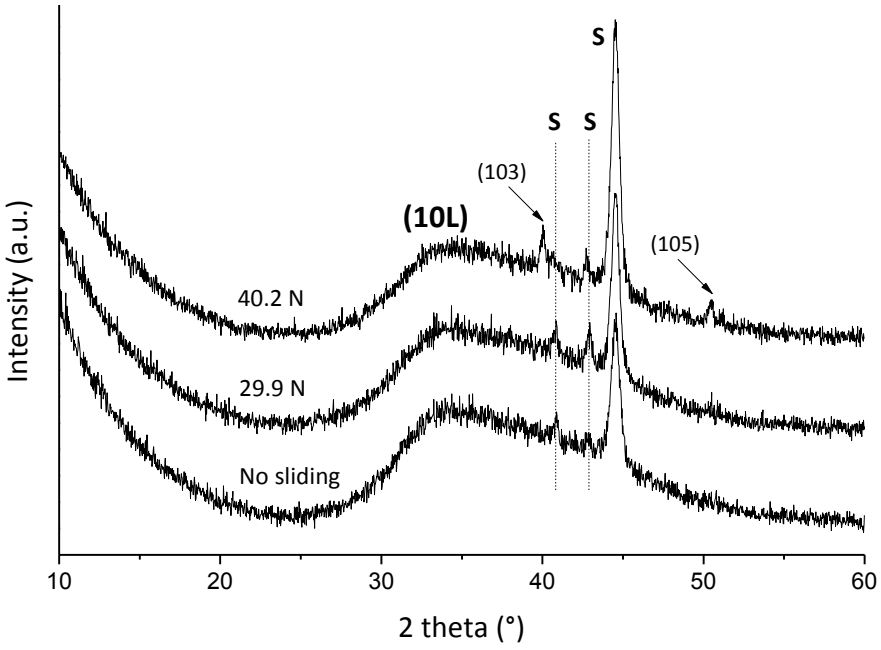

Fig. 4.6 Selected XRD spectra of W-S-C film surface and wear tracks.

There were small peaks in the spectrum obtained for the track produced by sliding under 40.2 N which were identified as WS_2 phase with (103) and (105) orientation. For the track produced with 20.9 N load, only a small decrease in intensity for (10*L*) was observed. There were no visible vestiges in the spectra of (002) orientation in the wear track, which would represent the

reorientation of the basal planes to a type I configuration, as observed by Hirvonen et al. for pure MoS_2 [73]. They have also observed a densification of the material with the sliding process, and a consequent increase in hardness values inside the wear tracks. For our films, hardness measurements were carried out both on the as-deposited surface and on wear tracks, but no significant difference was found (Fig. 4.7). It is likely that, since our coatings were already dense in the as-deposited state, re-orientation caused by the sliding process was only superficial and did not affect the mechanical properties of the film. This idea is supported by the lack of significant change in the XRD results.

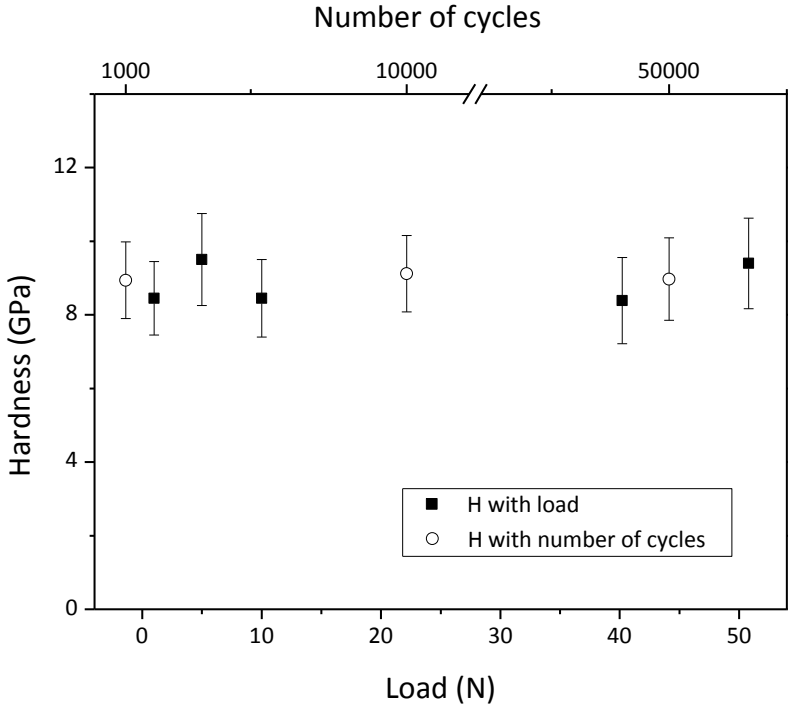

Fig. 4.7 Relation between hardness, load, and number of cycles.

4.3 Analysis of X-ray photoelectron spectra before and after sliding

In Ref. [74], Cohen et al acquired XPS spectra of WS_2 inside and outside a wear track and observed differences in oxidation of the material related to the acquisition position. XPS measurements of

our W-S-C films were also carried out on the free surface and inside one of the wear tracks (produced by sliding under a load of 50.8 N). However, due to the large spot size of XPS, results from the wear track spectra were in fact summarizing both areas. The chemical compositions evaluated by XPS were, indeed, practically identical inside and outside the wear track. To remove contamination, the surfaces were etched by sputtering before measuring the XPS spectra. The etching procedure was carried out for different durations in different areas, reaching depths of 5 and 15 nm (verified by 3D profilometry). Contamination by carbon, appearing as C–C peak at binding energy BE ≈ 284.5 eV is commonly used as reference for calibrating the measurements [50]. However, because the carbon in the coating could influence this peak, the O1*s* peak at 531.0 eV was used instead.

The W4*f* region of the as-deposited surface is shown in Fig. 4.8. The predominant doublet corresponded to W–S bonds (BE ≈ 31.6 to 33.6 eV). A second low-intensity doublet had to be included, at BE ≈ 35.6–37.8 eV, to fit the peaks adequately and was attributed to W–O bonds. Since the spectra fit well, there was no need to assume the contribution of peaks corresponding to W–C bonds, which would appear in this same region [75], contributing to the spectra. This is not, however, sufficient reason to exclude the possibility on W–C bonds existing in the film.

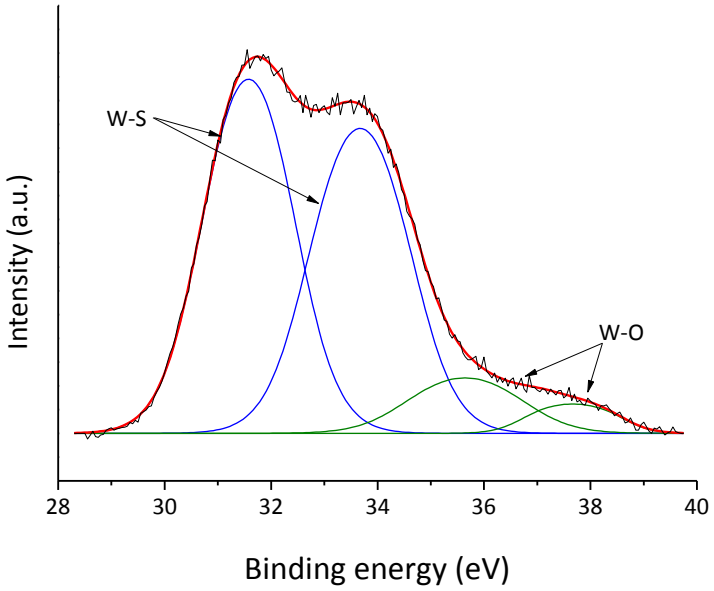

Fig. 4.8 XPS peaks acquired on the free surface in the W4*f* region.

In the S2*p* region (shown in Fig. 4.9), W–S bonds were indicated by the peaks at BE ≈ 162.0 eV. The smaller shoulder at approximately 163.7 eV is sometimes associated in literature with elemental

sulfur, which might have condensed on the surface of the film in the deposition process after there was no more power applied to the WS_2 target [76]. However, since the coatings were sputtered prior to the XPS measurements, elemental sulfur on the surface should have been eliminated, although vestiges could persist. Another possible explanation for the low shoulder is that it was due to S–C bonds, indicating that part of the sulfur in the film was in a carbon environment [31,77].

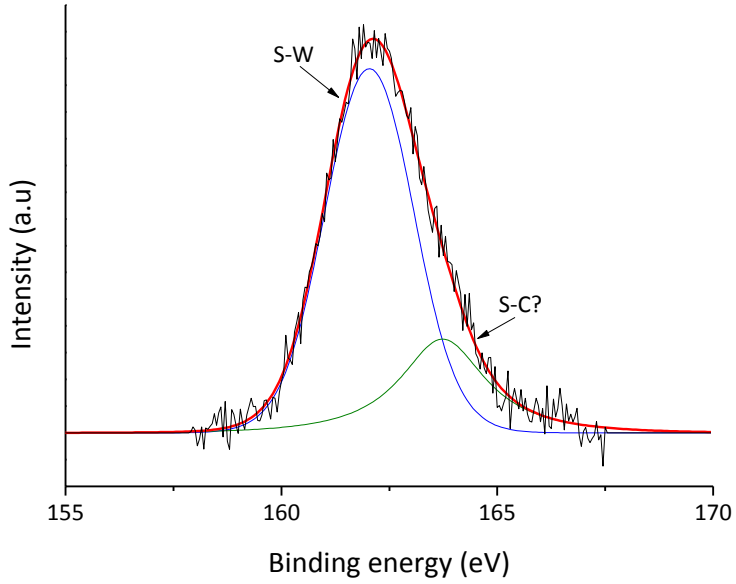

Fig. 4.9 XPS peaks in the S2*p* region.

4.4 Raman spectroscopy

Raman spectra of W-S-C films were characterised by two main regions of interest: peaks corresponding to WS_2 Raman modes that appeared prominently at approximately 307 cm^{-1} (E_{1g}) and 421 cm^{-1} (A_{1g}); and carbon D and G peaks, which appeared at approximately 1415 and 1570 cm^{-1}, respectively. The deconvolution of the peaks was rather difficult, since laser power had to be kept low consequently the spectra were noisy (a common problem of TMD-based solid lubricant materials). Therefore, the individual peaks in the WS_2 and C regions were not well differentiated, and only their total area was considered for quantitative analysis. Raman spectroscopy was carried out on the free surface and on different positions inside the wear tracks produced by 5000-lap tests. The ratio I_C/I_{WS2}, of the total area of carbon peaks divided by the total area of WS_2 peaks, varied

significantly with the position in the wear track, as shown in Fig. 4.10. The inset in Fig. 4.10 illustrates the positions where the spectra were acquired, from the outside (*I*) to the centre (*IV*). It can be seen that the ratio decreased progressively from the free surface towards the centre. These results evidence the formation of a WS_2-rich tribolayer as a result of sliding, and that it was influenced by the contact pressure.

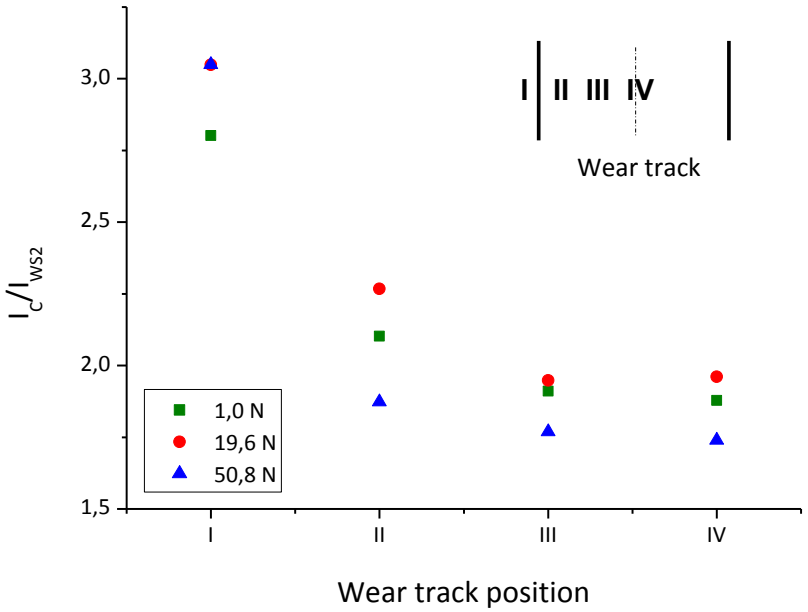

Fig. 4.10 Raman peak ratios according to position in the wear track.

Spectra were acquired in a similar way for the wear tracks produced by tests of different lengths under a 5 N load. In this case, the spectra were measured in the centre of each wear track. From the results, shown in Fig. 4.11, it can be seen that there was an immediate drop in the I_C/I_{WS2} value, which increased slightly for longer tests. The spectra acquired from the debris attached to the balls after the end of each test were always richer in C than the spectra acquired from the wear track (the I_C/I_{WS2} ratio was about one order of magnitude higher). This build-up of carbon on the attached layer on the ball could help explain the slow increase in friction in the steady-state of sliding. However, it could also be caused simply by progressive wear of the coating and also of the static partner – with more material worn out from the ball, the contact area increases, which under constant load means the decrease of the contact pressure. As described above, the decreasing contact pressure leads to a higher friction coefficient. The relevance of the carbon attached to the counterpart on the frictional behaviour of W-S-C coatings has to be studied more in detail in our future work.

To better examine the changes taking place in the beginning of the sliding process (i.e. the running-in process) that resulted in such drop of the friction coefficient in the first cycles, *in situ* spectroscopy was carried out as described earlier. The I_C/I_{WS2} ratio and friction coefficient for the first hundreds of laps are shown in Fig. 4.12. The peak ratio decreased rapidly in the first laps (as did the friction coefficient). The peak ratio then starts to increase monotonically after about 100 laps. Friction decreased rapidly in the first few laps due to the polishing of asperities in the film surface. The formation of a tribolayer took place in these first laps, by material transfer to the ball surface. With higher contact pressure, the initial wear was higher and therefore the tribolayer was formed more quickly. These observations agree with the friction curves shown above in Fig. 4.4.

The *in situ* test performed on the running-in process was repeated after the sliding exceeded 1000 laps. Raman spectroscopy was thus performed at 1000 laps, 1005 laps, and so on. The spectra acquired in this case did not show any significant change, demonstrating that the stopping and restarting of the sliding process was not responsible for the changes observed in the wear track before, confirming that such changes occurred indeed as consequence of running-in.

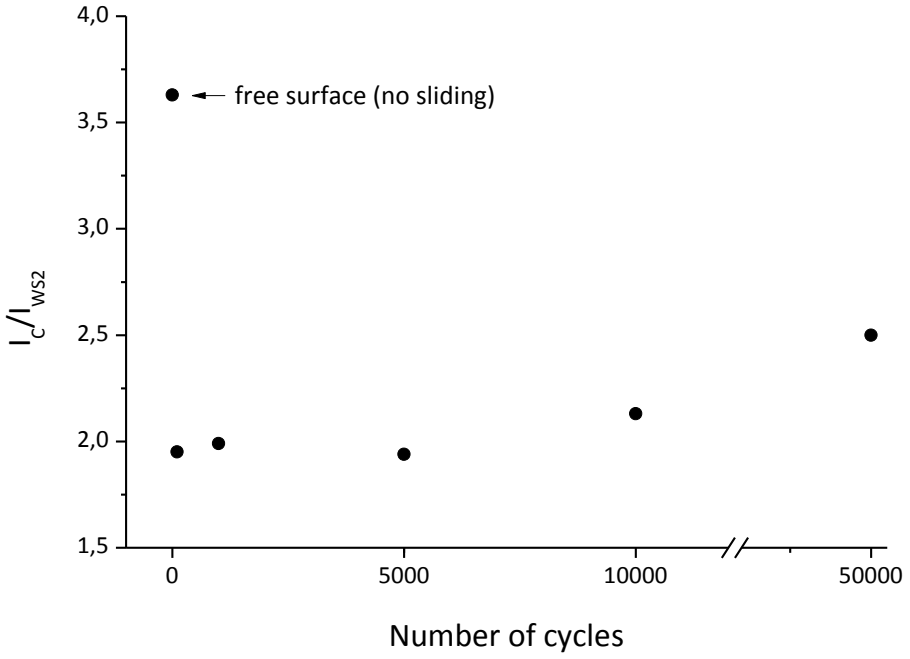

Fig. 4.11 Peak ratios as function of number of test length.

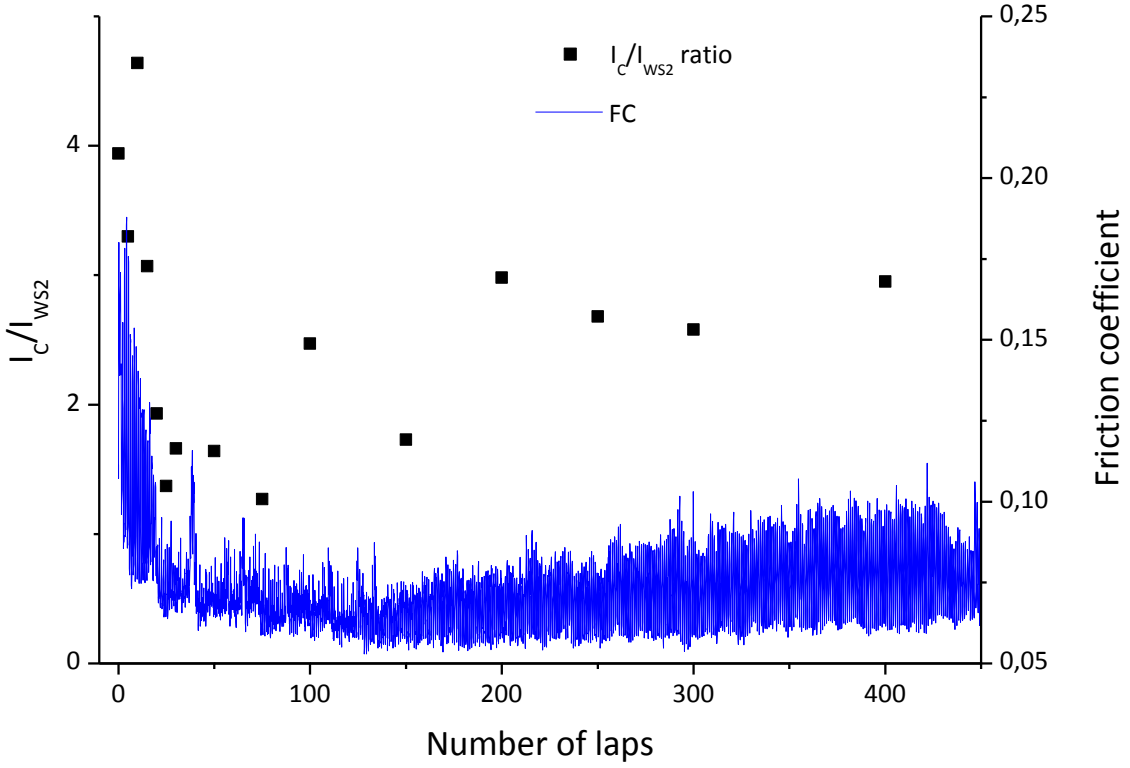

Fig. 4.12 Raman peak ratios and friction coefficient during running-in.

4.5 Comparison with other deposition methods

Table 2 presents a comparison of the main tribological results of these W-S-C films with others deposited by different methods. The tribological results for W-S-C films deposited by r.f. magnetron sputtering of a WS_2 target in CH_4 reactive gas are presented in Ref. [32] , whereas the tribological performance of films deposited by r.f. magnetron of a C target with WS_2 pellets were studied in Ref. [34]. Friction coefficients are presented for pin-on-disc tests using 5 N load in humid air for 5000 cycles. It is clear that co-sputtering produces W-S-C films with the lowest friction coefficient and the highest wear resistance. It is a very promising result from an application point of view, since d.c. sputtering is a simple and cheap deposition method compared to r.f.

Table 2 Comparison of tribological results for W-S-C deposited by different methods.

Deposition	**Friction coefficient**	**Wear rate ($10^{-6}mm^3/Nm$)**	**Hardness (GPa)**
r.f. sputtering in CH_4 reactive gas [32]	0.20	1.50	5.4
r.f. magnetron sputtering with WS_2 pellets [34]	0.20	0.55	10.0
d.c. co-sputtering	0.08	0.45	9.0

5 W–S–Cr (tungsten disulfide doped with chromium)

W-S-Cr films were deposited by d.c. magnetron co-sputtering, using one WS_2 target and one Cr target. The steel substrates prepared for deposition were polished with 3 μm-grain diamond solution. All substrates used – steel and silicon – were cleaned in ultrasound submerged in acetone and in ethanol, standard procedures adopted for all substrates in this work. Later, they were heated and cleaned inside the vacuum chamber by ion beam sputtering for 20 minutes prior to the start of deposition, a procedure adopted for all d.c. sputtering depositions. The films selected for further characterisation and tribological testing had chromium content measured by EPMA of up to 53 at.%; the metal content was almost linearly related to the power ratio of the targets (see Fig. 5.1).

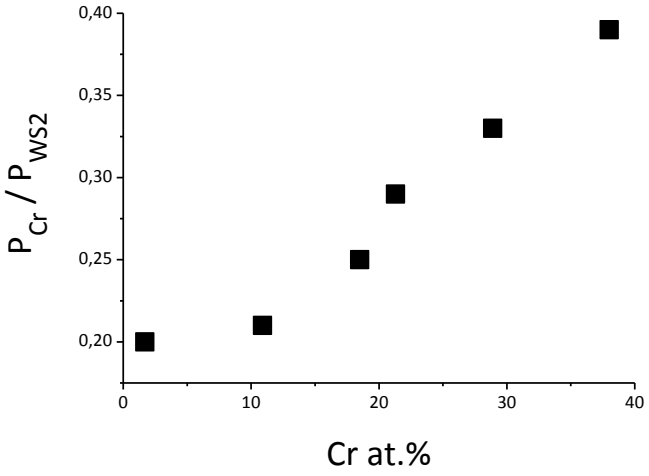

Fig. 5.1 Cr content versus target power ratio.

The chemical composition of the film with second highest Cr content could not be measured adequately (due to limitations explained in section 2.4.1). Its Cr content was estimated, from deposition parameters compared with other coatings in the series, to be approximately 38 at.%. It was observed that the adhesion of the coatings in this series was generally better for lower Cr content.

5.1 Mechanical and tribological properties

The coatings selected as viable for further testing had hardness between 2 and 9 GPa, with the majority of the compositions exhibiting hardness around 7.4 GPa. Although most of the coatings with lower hardness also had low Cr content (as somewhat expected, since pure WS_2 films are softer than doped ones studied so far), hardness values did not show any direct relation to chemical composition. However, there is evident effect of the pressure in the chamber during deposition. All coatings deposited in pressures lower than ~4.5×10^{-3} mbar exhibited hardness around 7.4 GPa, regardless of Cr at.%. Those deposited in higher chamber pressures displayed hardness values below 3.5 GPa (see Fig. 5.2). Fominski et al. [78,79] have studied the deposition of WSe_x- and $MoSe_x$-based thin films by pulsed laser deposition (PLD). Their results indicated that simple controlled variations in deposition parameters, in particular the inert gas pressure, could significantly alter the films, resulting in different chemical composition, structure, growth orientation of crystallites, the presence of large particles, etc. Moreover, they were able to develop models and simulation that predicted successfully the properties of films prepared by PLD [80].

Although our W-S-Cr coatings exhibited low friction in pin-on-disc tests performed in humid air, their friction coefficients were higher than those of W-S-C films tested under comparable conditions. Testing the W-S-Cr film with estimated 38 at.% Cr resulted in a mean friction coefficient of 0.11, while a W-S-C film with 42 at.% C showed friction coefficient of 0.07. The wear rate of W-S-Cr coatings was about one order of magnitude higher than that of W-S-C. It is therefore not surprising that few of the compositions survived 5000-cycles tribological tests with 5 N load, although the friction coefficient dropped to steady-state low values very quickly. It is very probable that low adhesion contributed to the high wear rates, due to the propagation of cracks and the removal of sections of film all the way to the substrate.

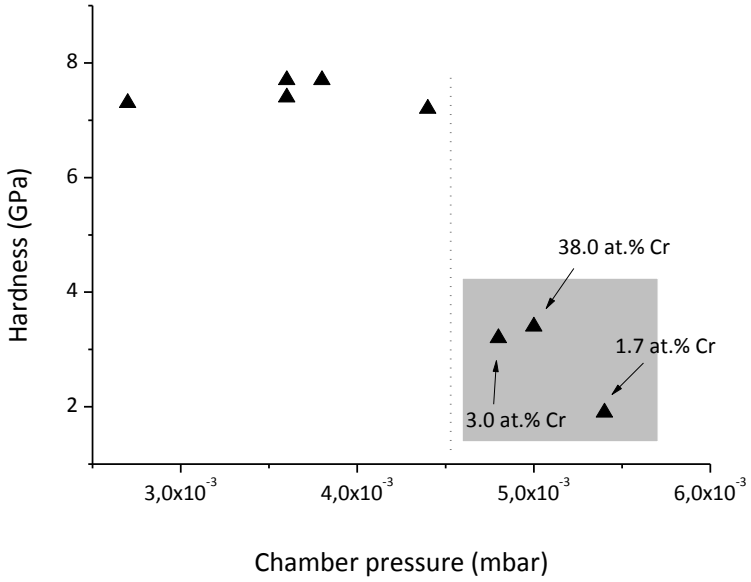

Fig. 5.2 Relation between pressure during deposition and the achieved hardness of the films.

The tribological behaviour of the W-S-Cr coatings had characteristics similar to other TMD-based systems, such as a decrease in friction coefficient (and wear rate) with increasing load. Furthermore, the friction curves could be divided into a) a running-in process with higher friction ($\mu \approx 0.15$) lasting some hundreds of cycles; and b) a steady state with lower friction. Although there was no significant relation between Cr content and mean friction coefficient, the friction curves exhibited different characteristics: in low Cr content films, the running-in process lasted a few hundred laps, while on films with higher Cr content it stabilized much faster – in less than 100 laps (see Fig. 5.3).

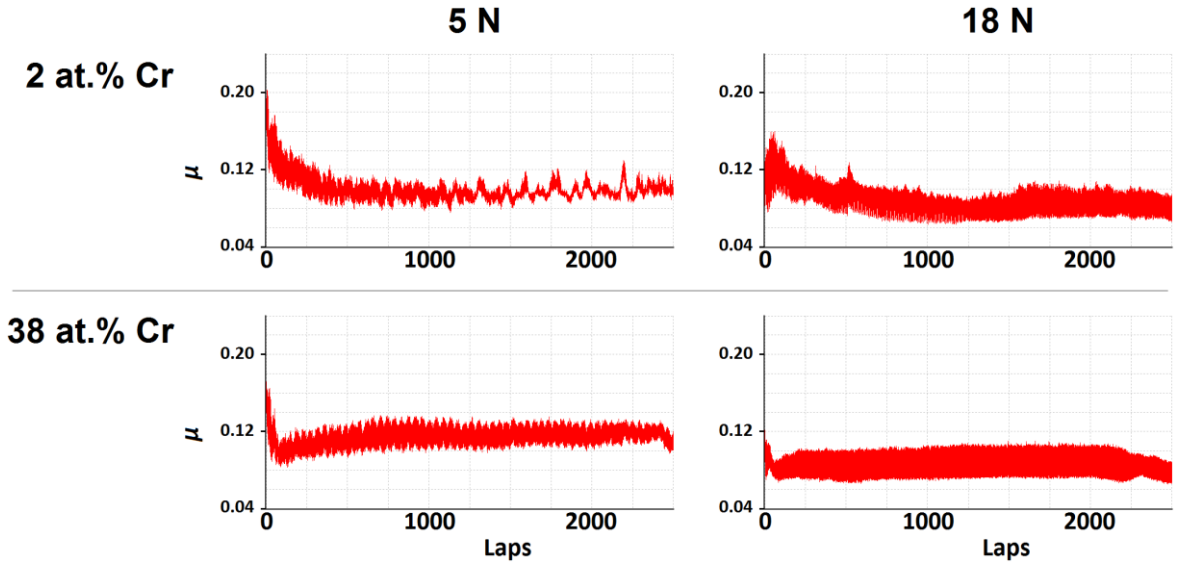

Fig. 5.3 Selected friction curves of W-S-Cr films.

5.2 Microstructure and chemical bonding

Comparison of XRD spectra of W-S-Cr and W-S-C films showed similarities in both cases, with relatively featureless spectra, in which the absence of sharp peaks evidenced amorphous films. For both systems, the dominant peaks were broad, related to stacking of planes. The main difference could be seen from the shape of the spectra: for W-S-C, there was an elongated shoulder extending from (100) to higher 2θ values; in W-S-Cr spectra (shown in Fig. 5.4 for different Cr content), however, the resulting peak was nearly symmetrical, although still broad. It indicated that the hexagonal phase was not so preferentially oriented. The resulting spectra were built from the overlapping of peaks representative of different orientations – with the most intense being (103), at $2\theta \approx 46.3°$. Obviously, very small grains with (103) orientation would yield identical spectrum; however, the presence of such microstructure is extremely unlikely. Scharf et al [81] observed very similar characteristics in the XRD spectra of Ti-doped tungsten disulphide films for various amounts of co-sputtered Ti (up to 35 at.%), attributing the changes in microstructure to Ti preventing the formation of crystalline WS_2.

SEM measurements were carried out to evaluate the morphology and to verify the featureless characteristic. However, the low energy used (because of temporary limitations in the equipment) prevented high-resolution imaging; therefore the absence of visible columnar or porous structure in SEM results (as in Fig. 5.5) is not strong evidence.

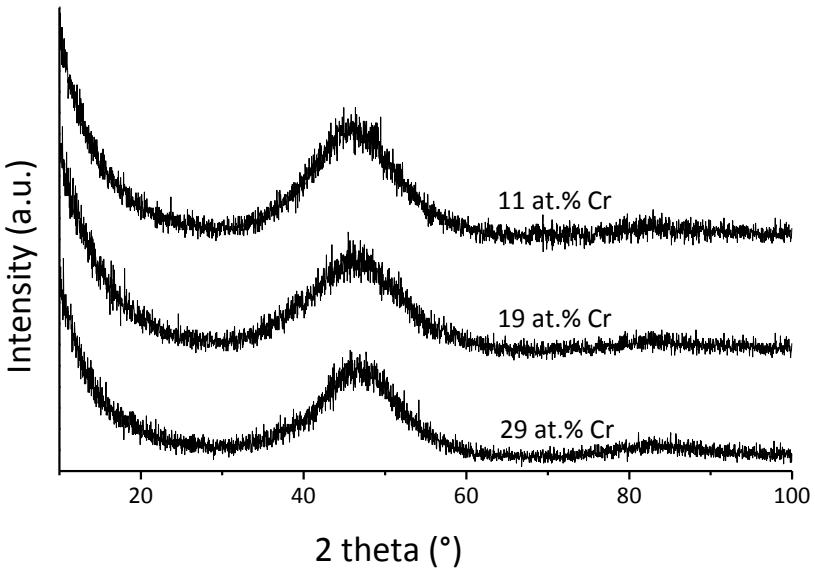

Fig. 5.4 Selected XRD spectra for W-S-Cr films.

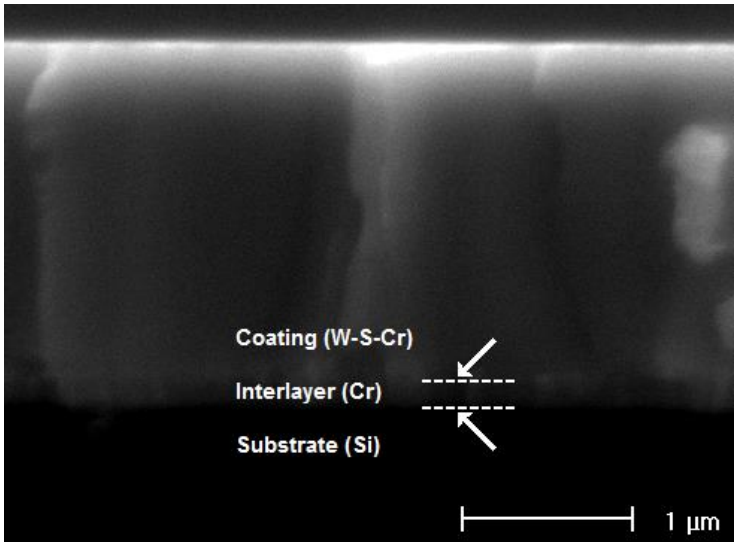

Fig. 5.5 SEM image of a cross-section of the W-S-Cr coating with 29 at.% Cr.

In the Raman spectra of W-S-Cr films (Fig. 5.6), the region associated with WS_2 had a different shape than expected. The broad elevation between ~230 and 450 cm^{-1} was possibly due to WS_2 broad peaks overlapping with a peak of Cr_2O_3 at approximately 350 cm^{-1} [82]. The sharp peak at 475 cm^{-1}, which is also associated with Cr_2O_3 [83], supported this interpretation. An additional weak peak related to chromium oxide could be expected at 550 cm^{-1}, although it could not observed above the noisy background.

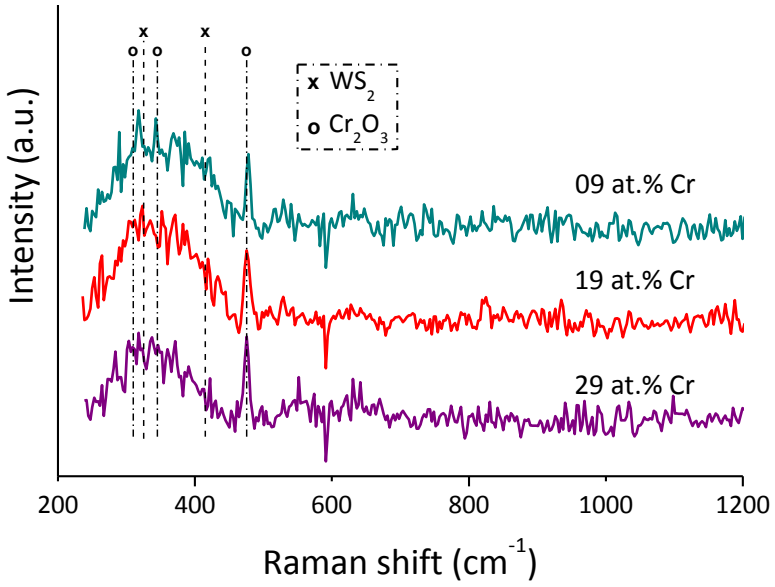

Fig. 5.6 Selected Raman spectra of W-S-Cr films.

The region of the spectra below 200 cm^{-1} exhibited a very broad elevation; however, this region is generally not assessed or no significant peaks are present. In fact, in previous results from Polcar et al., instrumental limitations prevented this region from even being measured [35,38], so comparisons to previous results is not possible. The shapes in this region might be due to second order Raman peaks [84], although such peaks are supposed to have intensity orders of magnitude lower than the usual peaks associated with WS_2.

6 W–S–C–Cr (tungsten disulfide doped with carbon and chromium)

Part of the content in this Chapter has been submitted to *Surface and Coatings Technology* in March, 2013, as:

> J. V. Pimentel, M. Danek, T. Polcar, and A. Cavaleiro, "Effect of patterned surface on the tribology of W-S-C/Cr self-lubricant coatings"

The deposition of tungsten disulfide doped with carbon and chromium was carried out by r.f. magnetron sputtering. Despite the similarity with the previously presented W-S-C and W-S-Cr systems, there were technical limitations of the d.c. magnetron sputtering chamber which made it impossible to deposit more than two materials (two targets) at once. In the r.f. chamber, however, while only two targets were used, the desired composition could be achieved by using a chromium target and a graphite target, with pellets of WS_2 spread evenly in the erosion zone of the C target. The number of pellets was controlled and determined after a few test depositions to achieve the same carbon content as the reference W-S-C coating, i.e. approximately 40 at.%. The C/WS_2 ratio was fixed, determined by the number of pellets, and the relative Cr content was controlled by the power applied to each target. To obtain the different Cr contents in this series, the deposition power ratio P_{Cr}/P_{C+WS2} was varied in three steps: 0 (no power in the Cr target, i.e. reference W-S-C coating), 0.8, and 0.13. The depositions with Cr were repeated to obtain a large set of samples with the same characteristics. EPMA results showed that the process is repeatable by using the same deposition parameters (see Table 3, where i, ii, iii denote different depositions).

Table 3 Chemical composition of W-S-C-Cr coatings.

Deposition		Chemical composition (at.%) - EPMA					Chemical composition (at.%) - XPS				
		W	S	C	Cr	O	W	S	C	Cr	O
0Cr		23.6	29.8	42.0	0.6	4.2	38.7	20.0	40.0	0.0	1.3
7Cr	i	20.3	25.1	40.4	7.0	7.2	34.0	20.5	33.4	6.8	5.3
	ii	19.1	26.6	38.2	7.0	9.1					
13Cr	i	17.4	23.0	37.7	13.4	8.5	32.0	17.0	33.1	12.0	5.9
	ii	18.5	24.1	35.8	13.5	8.1					
	iii	18.2	22.4	38.1	13.5	7.8					

Prior to the coating deposition, the substrates and targets were sputter-cleaned. The plasma was established close to the substrates electrode for 20 minutes. A chromium interlayer was deposited on the polished steel and Si substrates with the substrates stationary over the Cr target for 10 minutes, resulting in an interlayer approximately 350 nm thick. The coatings were deposited immediately afterwards (the chamber was not opened) with the samples rotating above both targets. Each deposition for coatings with Cr took 150 min, resulting in films between 1.7 and 3 μm thick. The deposition time was adjusted after the first deposition of the series (with no power in the Cr target), in which the thickness of the interlayer was measured as 450 nm and the coating thickness was 1.8 μm. The image shown in Fig. 6.1 was generated from SEM analysis of the cross-section, highlighting the interlayer. The vertical shades are not related to a columnar structure in the material, but instead are due to the imperfections in cutting and breaking the silicon wafer.

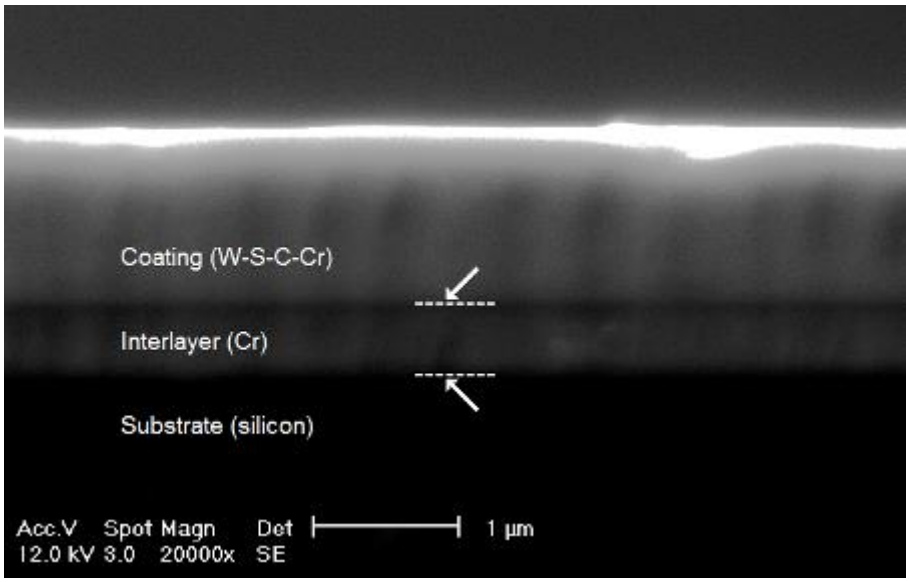

Fig. 6.1 SEM image of a W-S-C-Cr film cross section.

The substrates used were pieces of Si wafers and polished steel substrates (Ra < 30 nm, diameters of 50 and 22 mm), including steel substrates with different patterns of grooves produced by micromachining. The investigation involving surface patterns was focused on their effect on steel substrates covered by a relatively thick self-lubricant coating – in particular, to verify the effect of the rough patterning on the coating's tribological performance. Six different patterned substrates, labeled *A* to *F*, were prepared. Their distinguishing characteristics were as follows (see also corresponding diagrams in Fig. 6.2):

- A (diameter 50 mm): 6 equally-spaced grooves, approx. 45 μm wide, distributed radially;
- B (50 mm): 6 equally-spaced grooves with varying widths (85 – 170 μm), distributed radially;
- C (22 mm): 80 parallel grooves, approximately 50 μm wide;
- D (22 mm): 80 parallel grooves perpendicular to another 80 parallel grooves, each approximately 50 μm wide, forming a checkered pattern;
- E (22 mm): 240 grooves, each approximately 50 μm wide, distributed radially;
- F (22 mm): 30 grooves, each approximately 45 μm wide, distributed radially over about 25% of the surface.

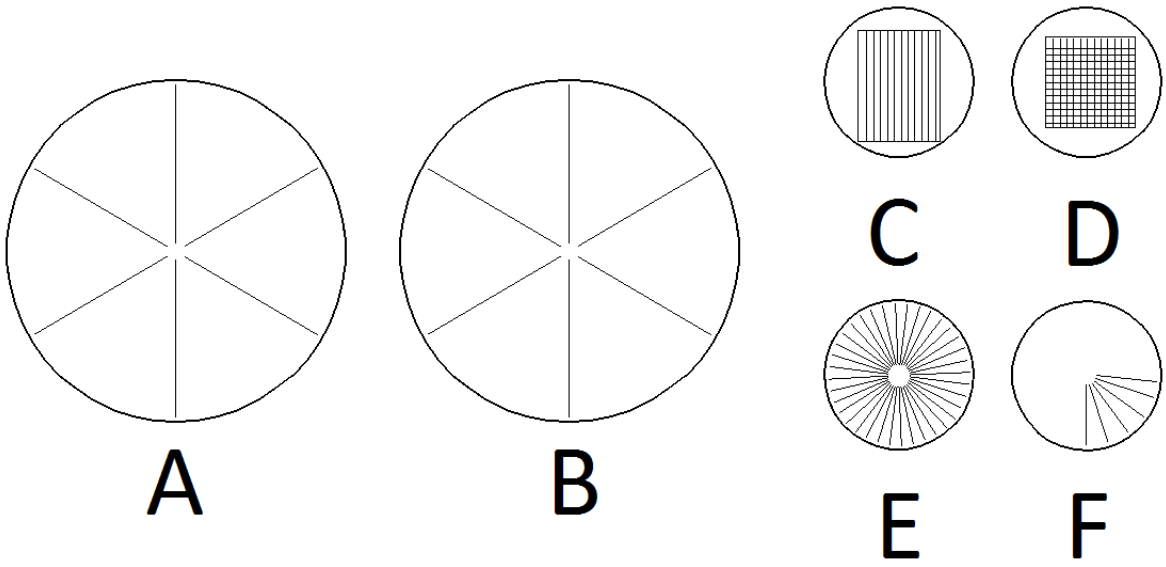

Fig. 6.2 Different patterns on the prepared samples.

On the patterned substrates was deposited the coating with the highest Cr content. Three-dimensional profilometry performed on selected spots on the grooves, before and after deposition, showed that the coating copied the surface features, as exemplified in Fig. 6.3.

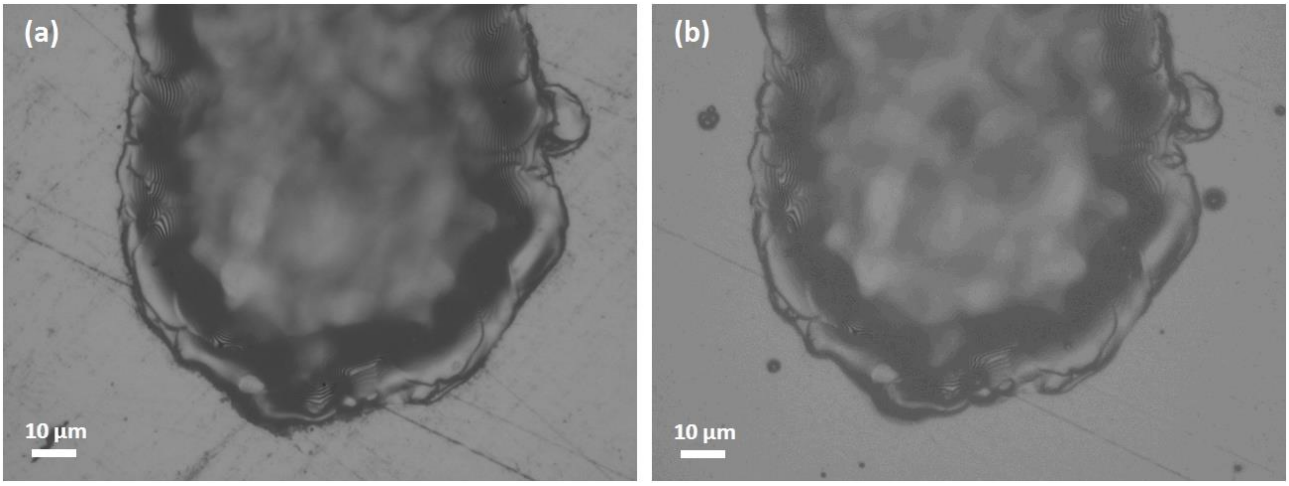

Fig. 6.3 Tip of a groove (a) before and (b) after coating deposition (sample A).

Patterning surfaces can facilitate sliding, particularly in the presence of lubricants. Cavities and grooves can act as fluid reservoirs and increase the wetting of the surface by a lubricant [85,86]; controlling the hydrodynamic pressure can also increase the load carrying capacity and lower friction [87,88]. Furthermore, grooves on the surface can trap wear particles and reduce abrasion and ploughing friction [87]. The effects of surface patterning have been studied extensively also for applications of solid lubricants. An approach often taken is the creation of grooves, which are then filled up with a deposited self-lubricant solid material. Voevodin et al. [89] prepared Ti-TiC-DLC films with grooves filled with MoS_2; they deposited also TiCN coatings with laser-produced micro-reservoirs, which were filled with MoS_2- and graphite-based solid lubricants by burnishing or sputtering [90]. Later, a similar approach was used to produce TiAlCN films with MoS_2-filled pores [91]. Zimmerman et al. [92] studied TiN hard coatings with micro-reservoirs filled with different types of solid lubricants. The results of those studies showed that solid lubricant reservoirs could reduce friction under certain conditions, although increased coating lifetime and wear resistance could be considered as the main advantage. Moshkovith et al. [93] produced patterns on steel surfaces and then burnished them with MoS_2 particles, achieving with contradictory results since the lifetime of the samples was extended, but the friction was higher compared to non-patterned samples. However, it must be noted that, unlike the present work, the majority of the studies cited above dealt essentially with very thin layers of solid lubricant just to fill up the patterns produced on another coating material.

Tribological measurements were carried out in humid air. Contact loads varied in the range 1–15 N and three test lengths were used: 1000, 5000 and 50000 cycles. Additional tests were

performed using the adapted system for *in situ* Raman spectroscopy referred to in Chapter 4, used specifically in this case to acquire video recordings of the wear tracks during the sliding process. These tests were performed at lower speeds, to improve the quality of the captured images, and with shorter arbitrary durations, as recording long tests generated a very large amount of data.

Wear rates of the coatings and balls were determined as the worn volume (measured by 3D white light profilometer) per sliding distance per load. However, the wear was often evaluated using only the cross-section area of the wear track, as described in section 6.5 below.

6.1 Chemical composition

The chemical composition of the final W-S-C-Cr coatings (calculated including oxygen) showed 36 to 42 at.% C and up to 13.5 at.% Cr. The S/W ratio depended mostly on deposition conditions, as described in Chapter 2, and was kept in between 1.2 and 1.4. The chemical composition was measured both by EPMA and XPS for comparison, since each method presents its own limitations. Etching of the surface performed prior to XPS measurements usually leads to a preferential removal of sulfur, resulting in lower sulfur content in the measured composition [94]. The preferential removal could be minimized by reducing ion energy, although in such case the etching would be extremely long. EPMA measurements, on the other hand, could overestimate the chromium content since the penetration depth (approximately 2 μm) is close to the thickness of the films, therefore the Cr interlayer could contribute to the results. This was observed in the case of the coating with no Cr, 1.7 μm thick, where the Cr detected originated from the interlayer. The other coatings, with approximately 7 and 13 at.% Cr (denominated 7Cr and 13Cr, respectively), had thickness close to 3 μm, therefore the signal from the interlayer should be negligible.

The contribution of oxygen to the chemical composition followed the same trend both in EPMA and XPS, increasing with increasing Cr content. For XPS measurements, the surface was ion-bombarded prior to analysis (etching away approximately 5 nm of the film) in order to remove surface contamination; so it can be assumed that the oxygen detected was due to the deposition process and not to later exposure to air. The fact that XPS showed lower O content values could indicate that the concentration of O was lower near the surface than further inside the film. Even though there was inevitably some residual atmosphere left in the chamber, it should be noted that the targets (especially graphite and WS_2) were porous and also released oxygen into the chamber

when sputtered. As the deposition proceeded, the amount of contaminants from the targets decreased; therefore the oxygen contamination in the coatings was indeed expected to decrease during the deposition process.

6.2 Mechanical properties and microstructure

The hardness of W-S-C-Cr films was between 4.9 and 7.2 GPa. The critical load L_{C2} was between 12 and 23 N, which was considered sufficient for tribological tests. Both hardness and adhesion increased with increasing Cr content (see Fig. 6.4). The increase of hardness has been observed for other co-sputtered films based on doped WS_2 and MoS_2, as shown above, and explained by the introduction of the dopant making the films more amorphous, reducing columnar morphologies and avoiding pores and voids. However, it can be noted in the case of the W-S-C-Cr series that in the coating without Cr (i.e. W-S-C) the co-deposition with C had already presented significant improvements over pure WS_2, although it was the softest of the series. Investigation by TEM of a W-S-C film had revealed randomly oriented and separated WS_2 platelets dispersed in the carbon matrix [34], which could slip easily and reduce hardness. Alloying W-S-C with Cr could therefore transform nanostructured films into amorphous material, as was verified by TEM (see Fig. 6.5) in a series of analyses performed by the Applied Materials Science group at the Department of Engineering Sciences of Uppsala University, Sweden, and published in [95].

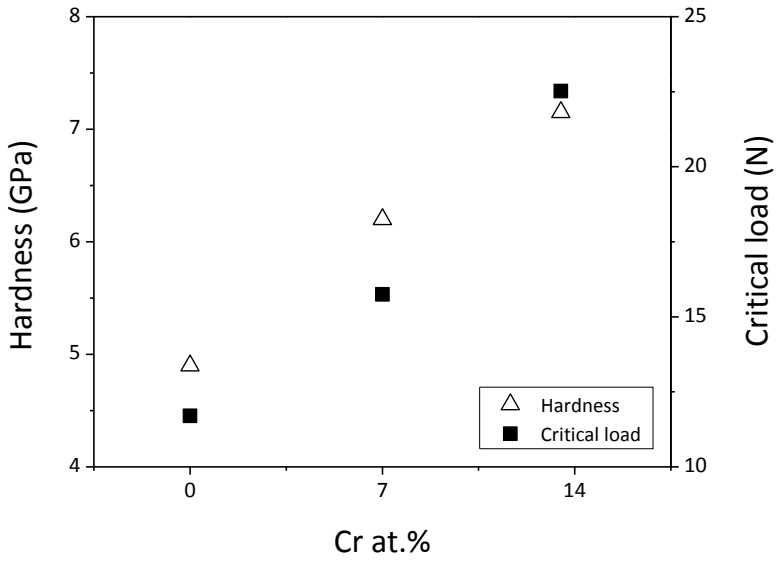

Fig. 6.4 Hardness and critical load for different Cr contents.

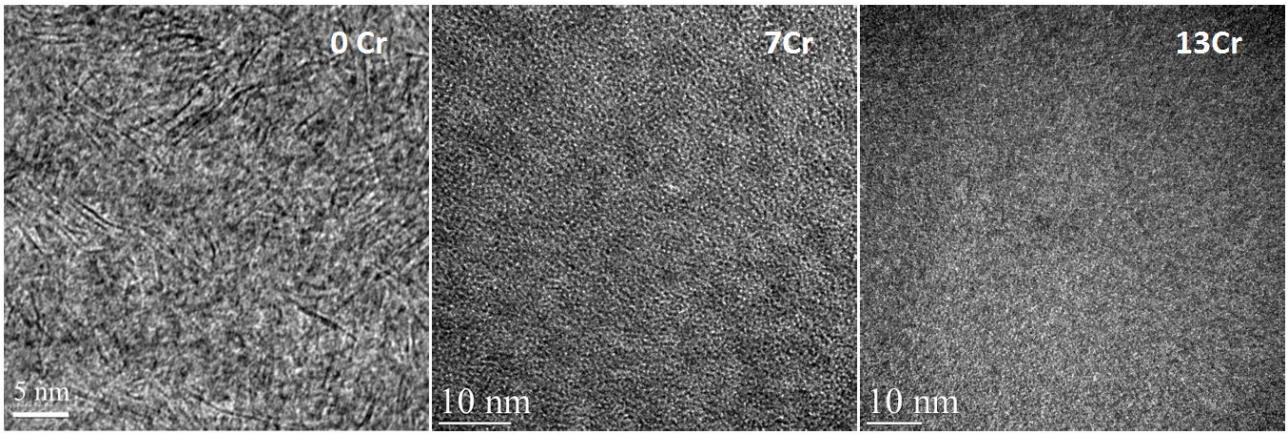

Fig. 6.5 TEM images of different compositions (adapted from [95]).

XRD analysis in grazing incidence configuration showed only a flat spectrum typical of amorphous films and confirmed the TEM observations indicating loss of crystallinity. As a consequence, the easy shear of WS_2 platelets in the W-S-C film was eliminated and the hardness increased. While nanocomposite W-S-C films with hard tungsten carbide and tungsten disulfide nanograins embedded into amorphous carbon matrix can exhibit hardness above 10 GPa, the W-S-C-Cr coatings presented were still significantly harder than pure sputtered WS_2 films [7,35].

6.3 Chemical bonding

6.3.1 XPS

XPS was first carried out on the as-deposited surfaces and, then, again after 48 seconds of sputter cleaning, which removed approximately 5 nm of coating material. A strong oxidation observed on the surfaces almost disappeared after etching. Fig. 6.6a shows W4*f* spectra taken after sputter-cleaning. The pair of peaks at approx. 31.9–34.1 eV was identified as a superposition of two pairs, corresponding to W–S bonds at 31.9–34.1 eV and W–C bonds at 32.4–34.6 eV. A reasonable fit could be achieved by deconvoluting the region even without attributing the W–C peaks; however, that would not satisfy the conditions suggested in Ref. [77]: a chi-squared value greater than 4 means more peaks are required for an adequate deconvolution, and a chi-squared value lower than 2 indicates a very good deconvolution. The presence in the C1*s* region of a peak attributed to W–

C bonds supported the four-peak deconvolution of the W4*f* spectra. The broad elevation at approximately 590–602 eV was attributed to satellite peaks [96]. Finally, W–O bonds were observed. As described in section 6.1, the main source of the oxygen detected in XPS was the contamination from the porous carbon target and tungsten disulfide pellets.

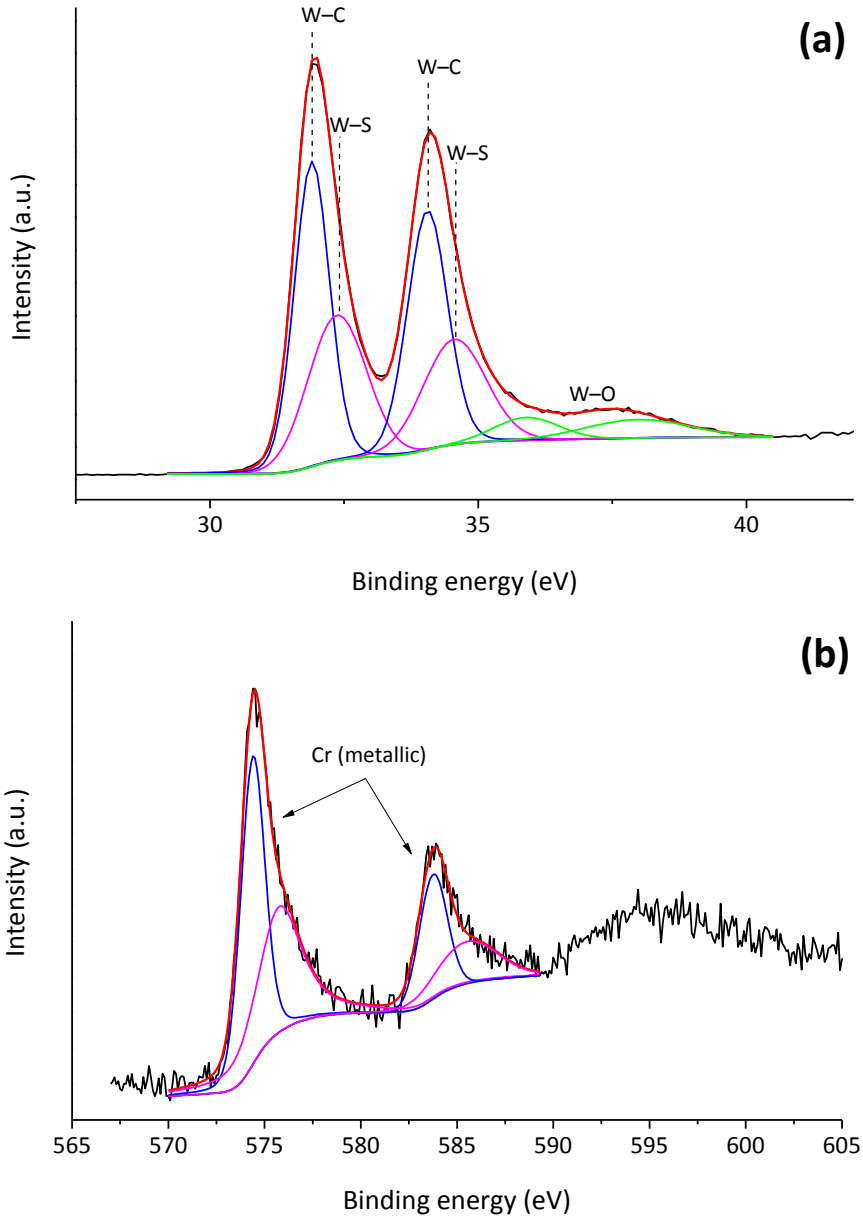

Fig. 6.6 XPS spectra of the as-deposited surface of 13Cr. a) W4*f*; b) Cr2*p*.

The Cr2*p* region of the XPS spectra (Fig. 6.6b) featured a pair of peaks at 574.4 and ~583.7 eV close to expected positions corresponding to metallic Cr (574.1 and 583.4 eV [77]). The possibility of this pair corresponding to Cr_2O_3, which shows peaks at relatively similar positions, was ruled

out by the peak separation (9.3 eV for metallic Cr, 9.7 eV for Cr_2O_3). It is possible, however, that very weak peaks at the positions associated with Cr_2O_3 (576.6 and 586.3 eV) were present, but should not have contributed significantly to the spectra. Unfortunately, we could not rule out the presence of Cr–C bonds or quantify their contribution, since their expected peaks are very close to that of metallic chromium.

The positions observed in the Cr2*p* region were also close to those characteristic of Cr–S and Cr–W, which pointed to the possibility of having Cr bonded to all those three elements – not surprising when considering the amorphous nature of the films. Nevertheless, the W4*f*, C1*s* and S2*p* spectra of all three film compositions were almost identical, whereas any strong contribution of Cr-related peaks to these regions (such as chromium carbide in the C1*s* region) should have been obvious when comparing the spectra of films with and without Cr. Therefore, it appears the alloying of W-S-C film with chromium did not change the bonding state of the film.

6.3.2 Fourier transform infrared spectroscopy (FTIR)

Fourier transform infrared spectra were also acquired from the W-S-C-Cr films. The principle of the FTIR technique is similar to Raman spectroscopy, with the key difference that the data is collected over a wide spectral range. The analysis of the acquired FTIR spectra was not very straightforward since the signal was noisy with a strong background (see Fig. 6.7). One feature in the spectra that was clearly distinguishable from the background was the region from 900 to 1300 cm^{-1}. Two prominent peaks observed at approximately 980 and 1260 cm^{-1}, along with the small peak at 1140 cm^{-1}, were similar to those associated with tungsten bonded to carbon [97]. However, peaks at 1079 and 983 cm^{-1}, as well as a broad band from 500 to 1000 cm^{-1}, are associated in literature to W–O bonds [98]. The proximity of these values made it hard to determine whether either alternative should be dismissed in favour of the other. In Ref. [99], a sharp valley at 1633 cm^{-1} was identified in the spectrum of WS_2, but it is hard to compare it with the results obtained in this work since the background noise in the entire region 1400–1800 cm^{-1} was particularly high. For the same reason, it was not possible to determine the presence of Cr_2O_3 peaks at 1450 and 1490 cm^{-1} [100] and C–C bonds at 1640 cm^{-1} [101].

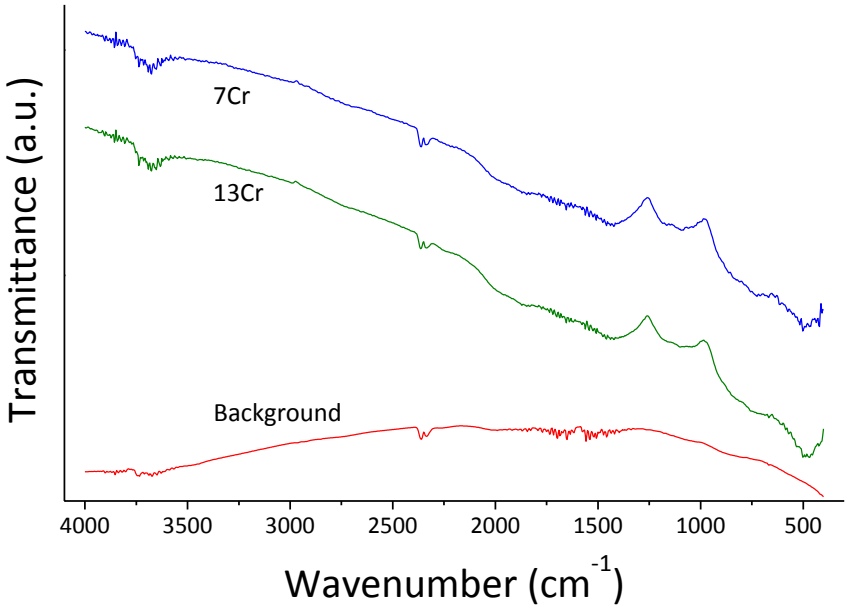

Fig. 6.7 FTIR spectra of W-S-C-Cr films.

6.3.3 Raman spectroscopy of the as-deposited surfaces

The predominant features expected in the Raman spectra of as-deposited W-S-C-Cr coatings shown in Fig. 6.8 were divided in two regions: i) in the range from ~1100 to 1700 cm^{-1}, two major peaks corresponding to the D and G peaks commonly observed in the spectra of carbon-based sputtered coatings; ii) in the range from ~230 to 470 cm^{-1}, peaks corresponding to WS_2 and chromium oxide. The spectra of Cr_2O_3 usually show a pair of weak peaks at approximately 305 and 350 cm^{-1} [83,83,102,103], which is very close to WS_2 peaks typically expected at approx. 307 cm^{-1}, 356 cm^{-1} and 421 cm^{-1}.

In the W-S-C-Cr series, the WS_2 peaks could be distinctly observed in the coating without Cr, but with the increase of Cr content the region was distorted and only vestiges of WS_2-related peaks could be made out. The change in shape could be due to the broadening of WS_2 Raman modes, related to the presence of structural defects and/or stress gradients in the scattering volume [104]. The results of Raman spectroscopy therefore agree with TEM observations: the broad WS_2-related peaks observed indicated a low structural quality of the WS_2 phase in the coating without chromium and the amorphous nature of the coatings with higher Cr content. Moreover, the I_D/I_G ratio of the carbon-related peaks, an indication of disorder in the material, also increased with Cr content.

A second reason for the distortion of the WS_2 region would be the overlapping of additional peaks (particularly Cr_2O_3, mentioned above) with those of WS_2. However, we did not expect a strong contribution of Cr_2O_3, given the low oxygen content in the coatings and the absence of significant Cr–O bonds in the XPS spectra. In fact, there was barely any evidence of other Cr_2O_3-related features: no peak could be observed at 475 cm^{-1}, and although a weak peak close to 550 cm^{-1} was visible in some of the Raman spectra, it was hardly identifiable above the noise level (which was relatively high due to low laser power).

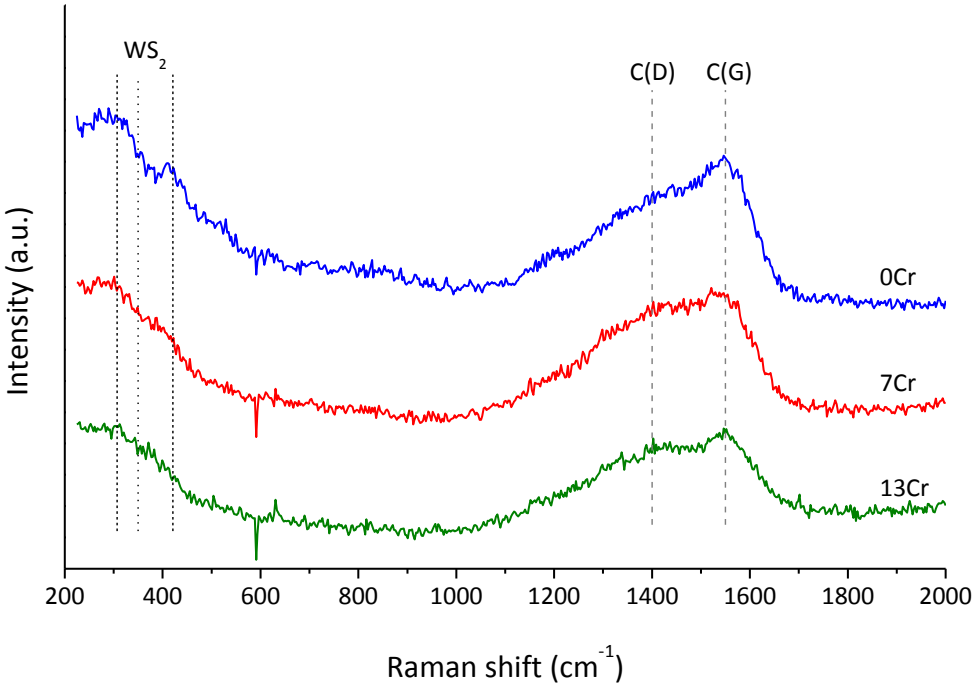

Fig. 6.8 Raman spectra of as-deposited W-S-C-Cr coatings.

6.4 Tribological properties of non-patterned samples

Pin-on-disc sliding tests were firstly carried out on flat (i.e. non-patterned) samples using different loads (from 1 to 15 N). The friction coefficient decreased with increasing contact load (as shown in Fig. 6.9 for different compositions) – a behaviour in a good agreement with other doped-TMD systems, indirectly indicating that the formation of a WS_2-rich tribolayer was promoted at high

contact pressures [19]. An investigation of the wear tracks indicated that the tribolayer was mostly amorphous tungsten and chromium oxide with small areas containing WS_2 platelets. Furthermore, a thin layer of (002) oriented WS_2 was found below the outermost surface, at the interface between the coating and the tribolayer [95] (its formation will be further discussed on Chapter 9).

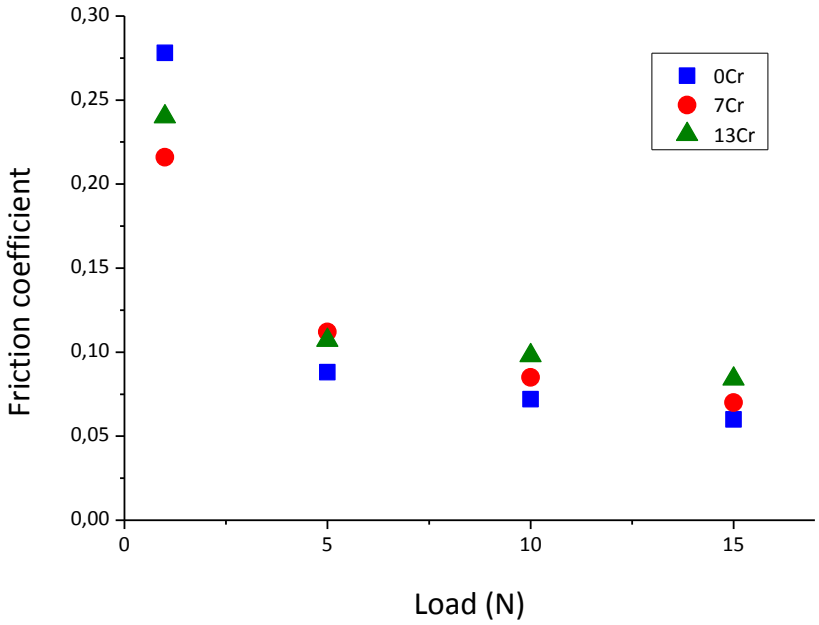

Fig. 6.9 Friction coefficient versus load.

As with other systems studied, the friction coefficient was usually high in the very first few cycles of pin-on-disc tests due to polishing of asperities and removal of superficial oxidation from contact area. After some tens of cycles, the friction values decreased as the tribolayer was formed. The friction coefficient usually reached a minimum at a few hundred cycles and then stabilized at a low-friction level typical of steady-state wear regime. The shape of the friction curves during running-in was similar to those observed in W-S-C films (see Chapter 4). The average friction coefficient increased with the addition of Cr, although it was lower compared to undoped WS_2 films under all test conditions [34]. In the coating with the highest Cr content, the friction coefficient in the initial stages was around 0.3 and the wear resistance was also the lowest of the compositions tested. Fig. 6.10 shows wear tracks produced under the same test conditions for different compositions and corresponding ball scars. Wear tracks on 13Cr had visible scratches in the direction of sliding and were deeper, reaching depths around 1.5 μm (approximately 70% of the thickness of the film). The wear rates of the contact partners were very low, particularly in the case of the intermediate Cr-content film.

Longer tests (50 000 cycles) were carried out for a better estimation of the evolution of wear during sliding. The coatings survived these endurance tests with no problems. The wear rates of the coatings were very similar after 5000 or 50 000-cycle tests. In fact, the 7Cr film showed lower wear rate after 50000 laps; since the worn volume was not much greater, the calculation of wear rate (which takes into account worn volume per sliding distance per load, as described in Chapter 2), yielded a lower value. These results indicate that the majority of the worn volume is produced during initial stages of sliding, whereas the wear is very low during steady-state regime.

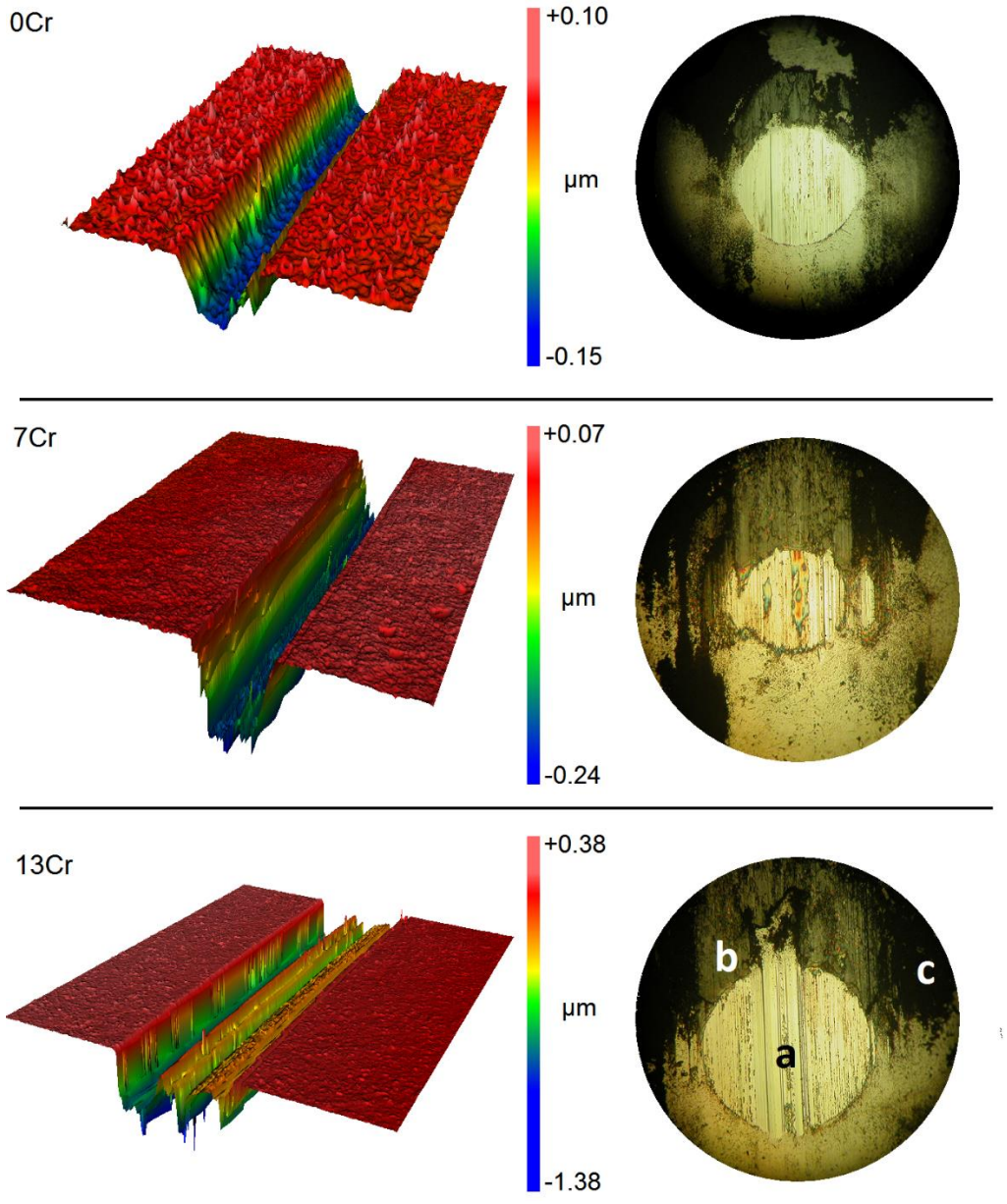

Fig. 6.10 Images of the wear tracks (by 3D profilometry) and ball wear scars (by optical microscope). On the ball corresponding to 13Cr are illustrated spots where Raman spectra were acquired.

Tribological tests in dry air (RH ≈1%) were performed on these samples by the Applied Materials Science group of Uppsala University. All such tests were carried out using a 10 N load and 10000 cycles. From these tests it could be observed that the friction of the 0Cr film started decreasing almost immediately (similar to what was observed in humid air), while the friction of the Cr-containing coatings showed a slow increase before dropping to steady-state levels. Nevertheless, the running-in processes of all three coatings had similar lengths, close to 2000 cycles. For all tests in dry air, the friction coefficient in the steady state was very low, in the range 0.018–0.025 [95].

6.4.1 In situ monitoring of the wear track

The adaptation of the equipment allowed an *in situ* video monitoring of the surface during sliding. Although these observations could not be as detailed as the 3D profilometry, they allowed some interesting observations. The wear tracks of W-S-C-Cr films were quite irregular – there were scratches and the cross-section was seldom circular – therefore we could not make accurate calculations of the wear rate only from the top imaging. Nonetheless, it was possible to verify that the width of the wear track expanded rapidly in the first tens of laps, then widened very slowly. Fig. 6.11 shows the same region in a wear track on 7Cr in two different moments – after 100 and 500 cycles. It could be observed in this case that the width of the wear track after 100 laps was approximately 95% of the width after 500 laps. In comparison, in another test under the same conditions (except for higher linear speed), after 500 cycles the friction curve had already stabilized at approximately the same value it would maintain until 5000 cycles, and the sliding process could be considered to have reached the steady state.

The tests using video monitoring were performed with different speeds. In the case described, the first 75 cycles were carried out very slowly at 0.54 cm/s, while recording; then the speed was increased to 15 cm/s (a normal value for our pin-on-disc tests), to continue the running-in process; and then after the 500th cycle, another 25 laps were carried out at 0.54 cm/s. In Ref. [35] the effect of sliding speed on friction was analysed for W-S-C films. It was shown that decreasing the speed reduced frictional heating and caused an increase in friction. Such effect is hardly significant for small variations in linear speed; however, in the present case the difference is very large, therefore it was expected that the slow cycles would exhibit higher friction. This expectation was supported by the results: in the last 50 cycles at 15 cm/s (i.e. cycles 450–500), the mean friction coefficient was quite stable at 0.09. In the following 25 cycles at 15 cm/s, the friction coefficient was 0.13. There was no reason to assume any other cause other than the decrease of sliding speed.

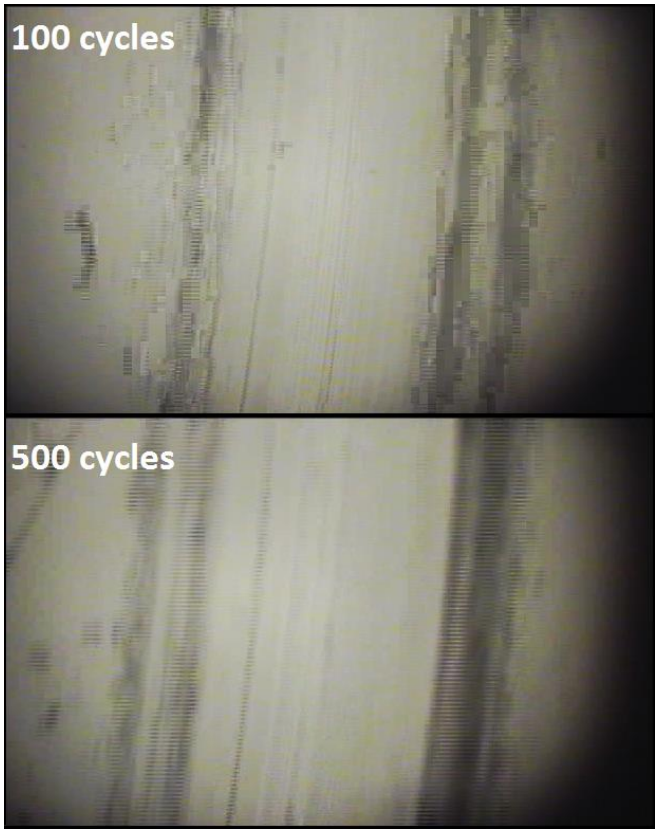

Fig. 6.11 Wear track on 7Cr, after 100 and 500 cycles.

6.4.2 Raman analysis of the wear tracks and sliding partners

The study of C-doped WS_2 films had shown that the running-in process was characterised by carbon being quickly worn away and a thin tribolayer, composed mainly of tungsten disulfide, being formed at sliding interface. Furthermore, the formation of the low-friction tribolayer was enhanced at higher contact pressures. This effect was evidenced, among other analyses, by *in situ* Raman spectroscopy inside the wear tracks during and after the running-in process.

In the case of W-S-C-Cr coatings, the overlapping of WS_2 and Cr oxide peaks in the Raman spectra (described above for W-S-Cr) could also influence the ratio I_C/I_{WS2}. For the same reason, it was not possible to determine from Raman spectra whether chromium oxide was present in the tribolayer. Its contribution should be limited, since the region in question was almost identical in spectra measured inside or outside the wear track. Therefore, the total areas for the WS_2 region (~230 to 470 cm^{-1}) and the C region (1100 to 1700 cm^{-1}) were compared for spectra acquired in the middle of the wear tracks produced with different loads. A clear trend could be observed with the contribution of C peaks to the spectra decreasing when higher loads were applied, see Fig. 6.12.

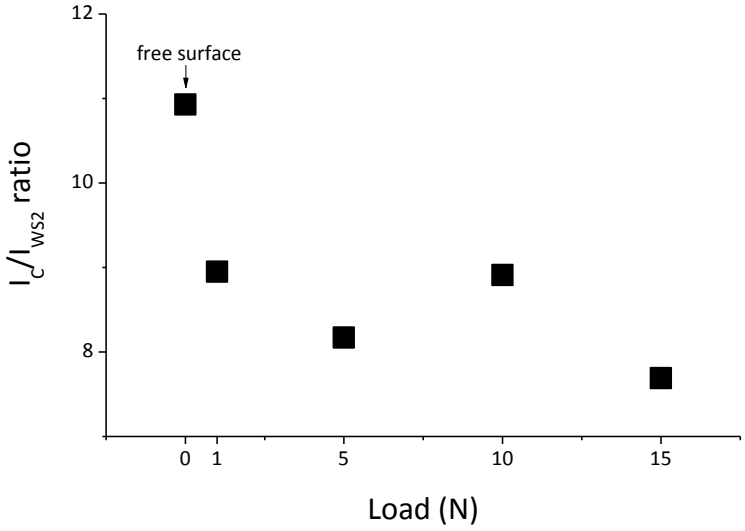

Fig. 6.12 I_C/I_{WS2} Raman ratios versus contact load, 13Cr coating.

Further evidence of the tribolayer composition came from the Raman spectra of the debris attached to the wear tracks and ball wear scars. The material adhered on the balls could be divided into three groups, based on its position in relation to the wear scar. In the ball image of 13Cr (shown in Fig. 6.10), the positions of Raman measurements are indicated: (a) – very thin layer on the wear scar; (b) – debris attached to the front of the wear scar; and (c) – debris scattered on the sides of the wear scar. Raman spectra of balls scars produced with different load usually displayed similar characteristics (with the occasional exception of the layer at the centre, which was not always measurable). The spectra shown in Fig. 6.13 illustrate the differences between adhered debris in point (c), which is significantly richer in carbon, and point (b), which is richer in WS_2. Peaks corresponding to carbon were relatively weak in the spectra acquired at the centre of the scar, point (a). A large asymmetrical peak at ~940 cm^{-1} was attributed to iron oxides originated from the ball material. The differences in the spectra show that the tribomaterial produced under sliding is more ordered than the as-deposited film, as evidenced by the sharper WS_2 peaks typical of an ordered structure. Furthermore, the separation of the C region into more distinct peaks indicate a structural change (graphitization) of carbon as well, although it is important to note that the carbon-rich debris was not found in the contact. Therefore the results indicated, as observed before with W-S-C, that the sliding process promoted the formation of a well oriented WS_2-rich tribolayer.

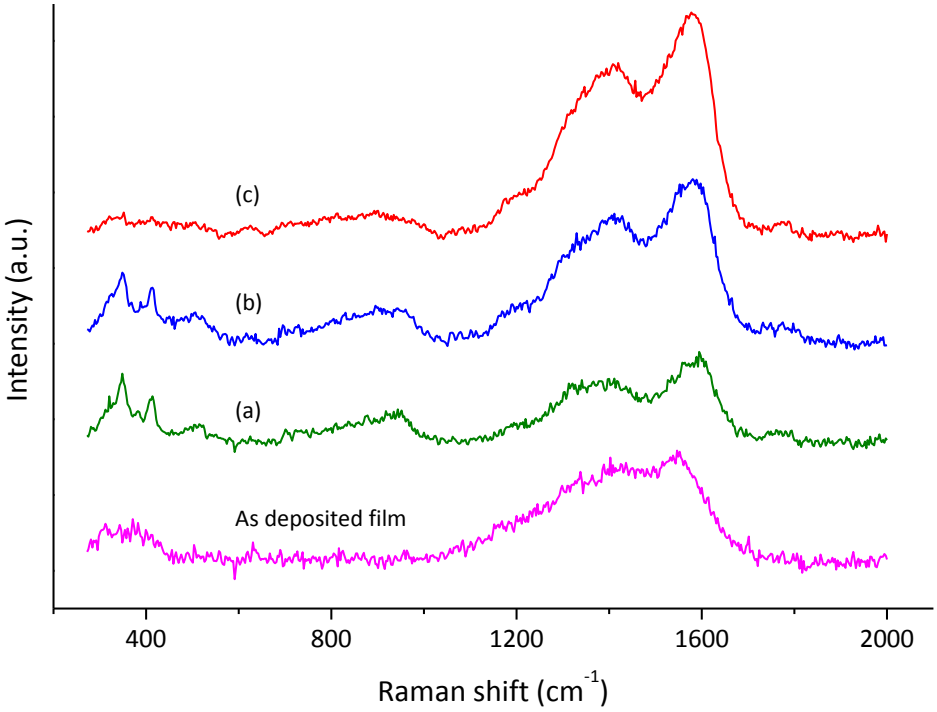

Fig. 6.13 Raman spectra of the material adhered to the steel ball in the positions indicated in Fig. 6.10, after test with load 10 N.

Raman analysis of a wear track produced on the 7Cr film by sliding in dry air after 10000 cycles exhibited a pair of strong sharp peaks at ~350 and 420 cm^{-1} indicating a well-ordered and relatively thick layer of WS_2. This characteristic was not observed in the spectrum of a wear track produced in humid air and otherwise equal conditions, where the peaks in the WS_2 region were poorly defined, related to a lower structural quality. These results suggest that humidity alone can hinder the formation of a well-ordered tribolayer.

6.5 Tribological properties of patterned samples

The tribological behaviour was significantly affected by the presence of grooves on the surface. For tests carried out with a load of 5 N for 5000 cycles, the coefficient of friction of the non-patterned 13Cr coating was 0.11. The patterned samples C–F exhibited overall higher friction, above 0.15, with the highest value of 0.20 observed for sample E, i.e. the sample with the highest density of grooves. However, the coefficient of friction measured for samples A and B (0.10 and 0.09, respectively) was slightly lower than that of the polished sample. Typical friction curves

(examples shown in Fig. 6.14) showed that the friction coefficient during running-in was somewhat erratic, although it usually stabilized within about 500 cycles.

Similarly to non-patterned samples, the average friction of samples A and B decreased with load (see Fig. 6.15). The friction coefficient over one cycle during the running-in is shown in Fig. 6.16 (sample A, load 1 N). Six transitions in friction (sharp drops followed by an immediate increase) were separated in six regular intervals, matching well the surface pattern. However, these transitions disappeared when the steady-state wear regime was reached and, then, the friction was more stable.

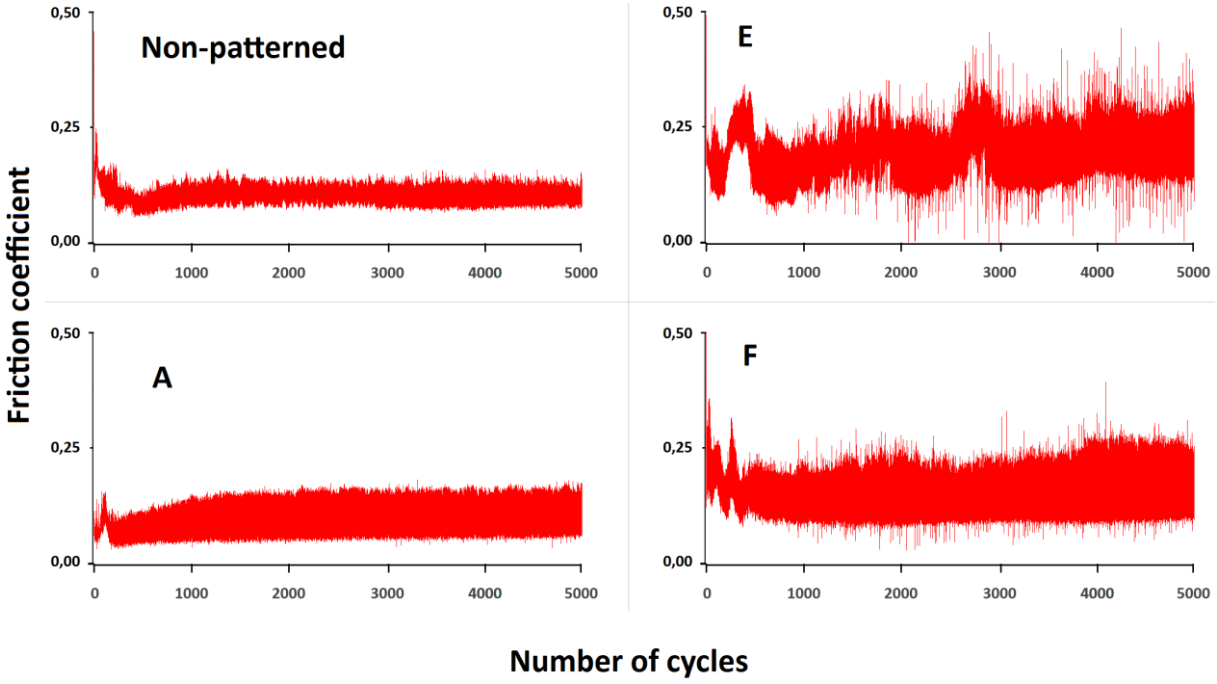

Fig. 6.14 Selected friction curves of non-patterned and patterned samples.

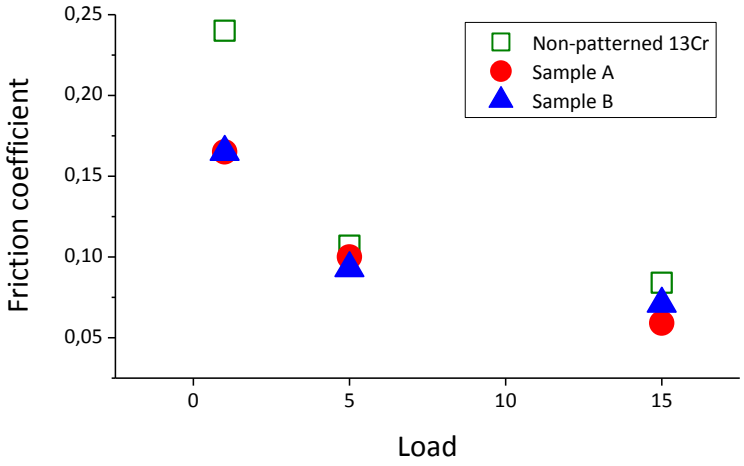

Fig. 6.15 Friction coefficient versus load for samples with and without grooves.

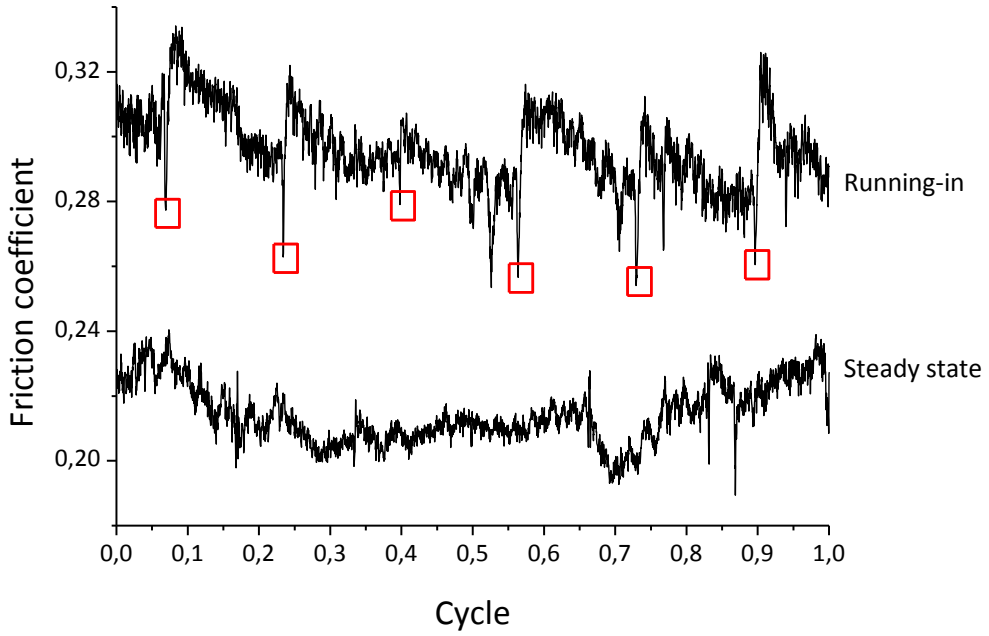

Fig. 6.16 Friction coefficient over one cycle during running-in stage (sample A).

6.5.1 Analysis of the wear tracks

On non-patterned samples, we averaged the measurements of the wear track cross-section areas in different spots along the wear track to determine the wear rate as the worn volume per sliding distance per load. For the patterned samples, wear rates were not calculated since there were clear changes in the worn volume from one spot to another. 3D profilometry of the wear tracks after the sliding tests revealed that the grooves were completely filled up in the wear tracks. Raman spectra obtained directly on the material accumulated in the grooves, after sliding tests on samples A and B, were almost identical to spectra obtained immediately before or after the grooves (always from the centre of the wear track; see Fig. 6.17).

An interesting wear behaviour has been observed in the vicinity of the grooves. In the following analysis the cross-section area is used to characterise the wear, instead of the wear rate, since it allows direct comparisons between different sections or positions in the wear tracks. Using this approach, we could observe that the wear was significantly lower immediately after the grooves on sample A. The sudden drop was followed by a slower increase up to values comparable to those observed before the grooves (see Fig. 6.18). Moreover, the wear tracks were much smoother and shallower after the grooves than before.

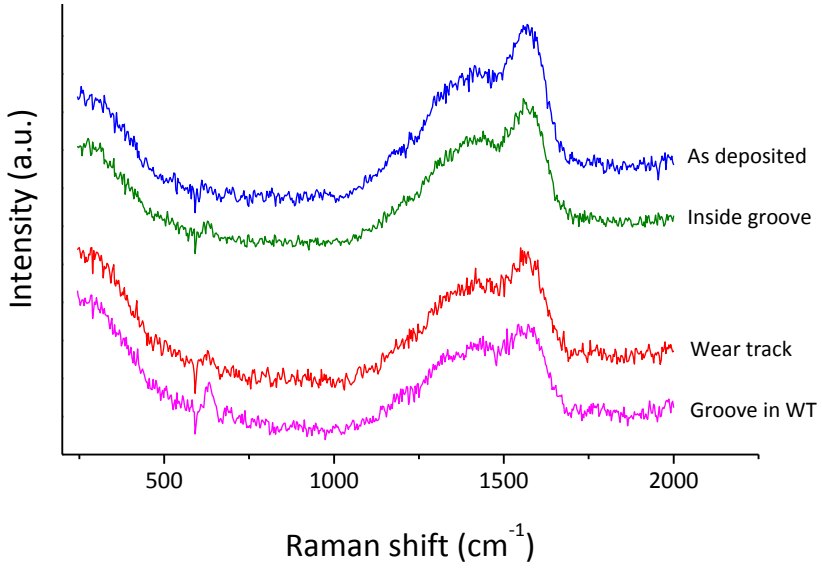

Fig. 6.17 Raman spectra acquired on the polished surface and inside the groove after deposition, and in the centre of the wear track inside and outside of the grooves (sample A).

Quantification of the wear track recovery, i.e. the decrease of the wear track cross-section area after the grooves, was not straightforward since the cross section is rarely constant along the entire wear track, even in the case of non-patterned samples. This is primarily due to the conditions of the tribological tests, such as sample position in respect to loaded arm with the ball. To minimize the effect of the wear track area fluctuations, Fig. 6.18 shows the wear track area for every single groove (named *g1* through *g6*) on sample A. It can be clearly seen that there was always a significant drop of the cross-section area immediately after each groove. Sample B, with 6 equally-spaced grooves with different widths, exhibited similar trend (as shown in Fig. 6.19).

When the pin-on-disc tests were performed on sample C, the angle between the sliding direction and the grooves periodically changed from 0 (parallel) to 90° (perpendicular), twice every cycle. The high average friction of 0.2 clearly indicates that the density of the grooves was too high to achieve a positive effect. The variation the friction coefficient clearly depended on the position of the ball on the surface: for perpendicular sliding (i.e. the ball crossing the grooves at a right angle), the friction reached maximum about 0.27, whereas the minimum value 0.13 was observed for parallel sliding (see Fig. 6.20).

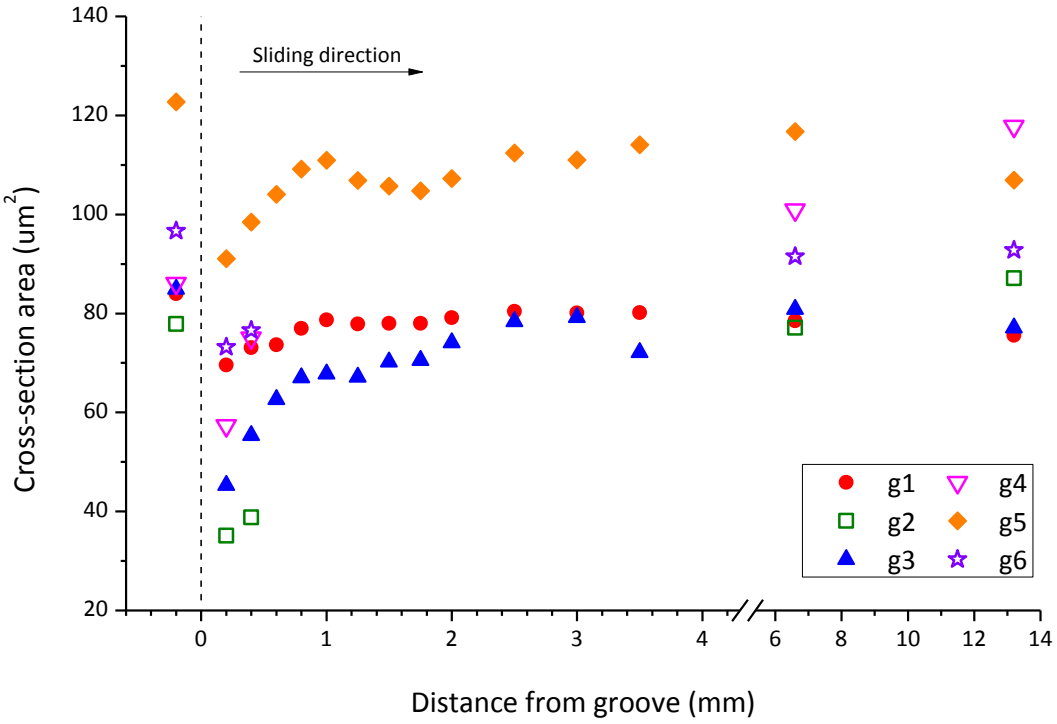

Fig. 6.18 Cross sections immediately before and after grooves. In this wear track, produced with linear speed 50 cm/s, the distance between each groove was 19.9 mm (sample A).

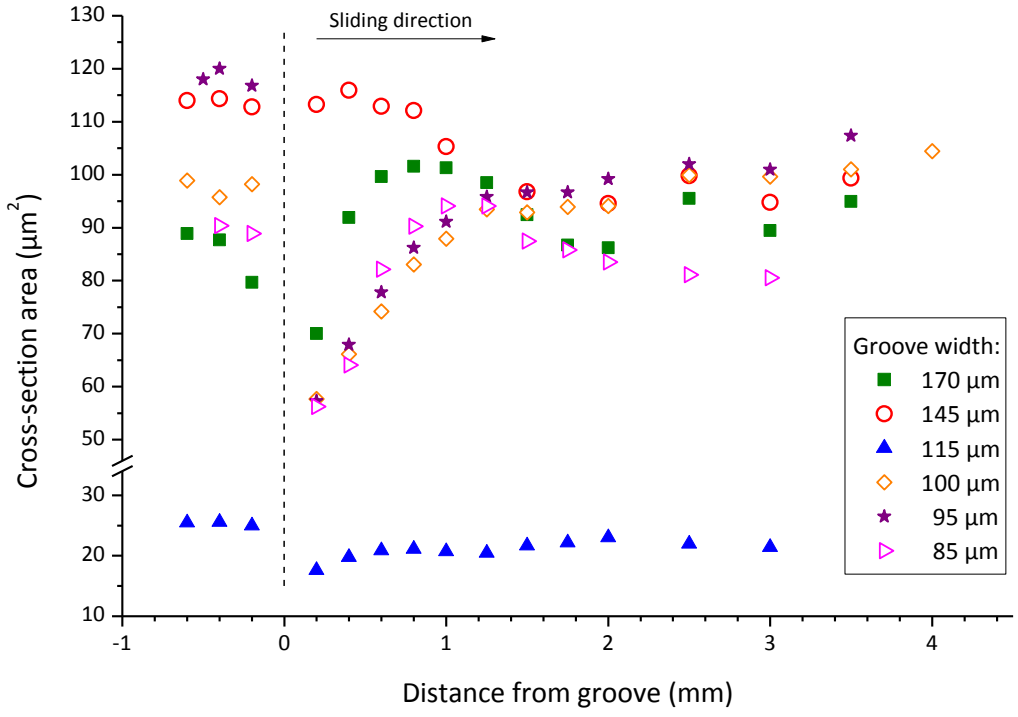

Fig. 6.19 Cross-section area of the wear track in the vicinity of the grooves (sample B).

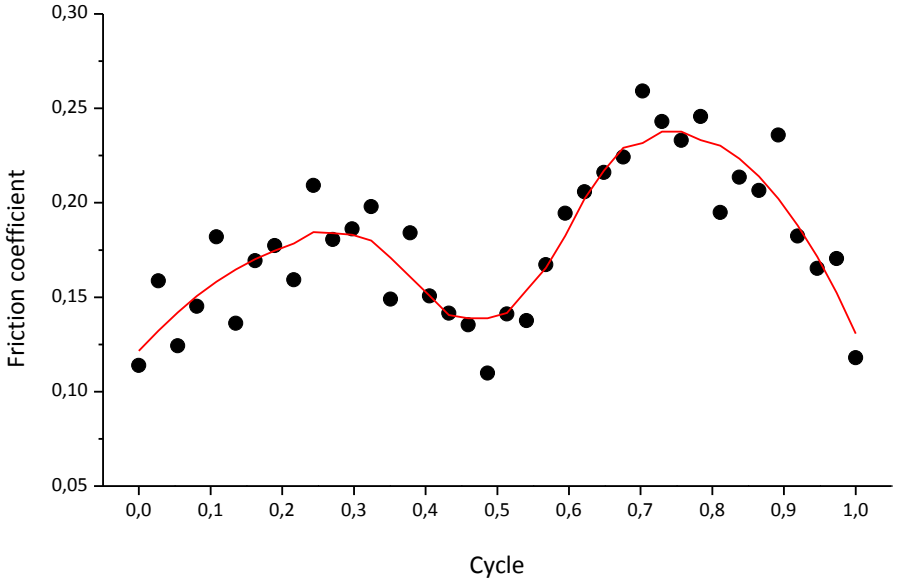

Fig. 6.20 Periodic variation of friction over one cycle on sample C, after 3000 laps. The average is shown to help visualization.

Sample D, with an orthogonal matrix of grooves, exhibited friction coefficient higher than 0.25, which was independent of the position. The wear of sample F increased rapidly when the ball entered the patterned region, see Fig. 6.21. The maximum wear occurred far from the first groove, i.e. it increased progressively within the patterned area until reaching maximum value. Then, it decreased smoothly during sliding the non-patterned zone.

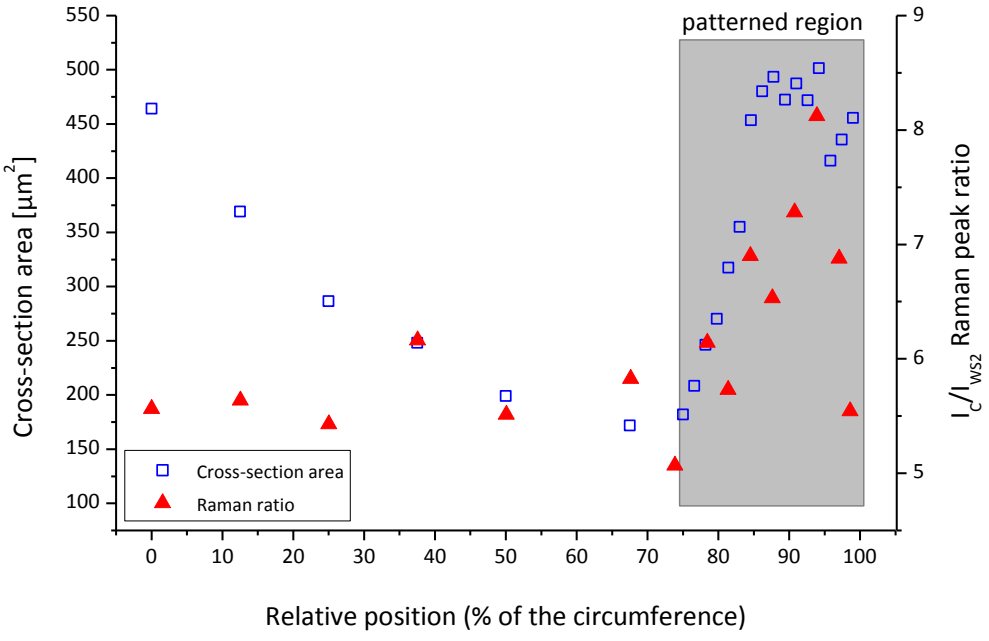

Fig. 6.21 Cross-section area and I_C/I_{WS2} ratio of the wear track as a function of position on sample F.

6.5.2 Discussion on the effects of surface patterns on the tribological behaviour

Grooves produced on samples A and B could be considered as isolated, i.e. there was sufficient polished surface between two consecutive grooves. Their effect on friction and wear altered the sliding process. In the running-in stage, friction increased when the ball passed a groove due to higher surface roughness. However, the grooves became progressively filled up by worn material. Raman spectroscopy indicated that the material trapped inside the grooves was identical to that of the tribolayer observed in the wear track. The grooves, fully covered by tribolayer material, could thus act as a reservoir of low-friction material, decreasing friction and wear immediately afterwards.

The data suggest that the positive effect of sample patterns is limited to widely spaced grooves (as in samples A and B). When the grooves were too close, the low-friction tribolayer could not be formed when the ball passed between the grooves. As a consequence, neither the material in the contact area nor the material trapped in the grooves were identical to a low-friction layer. The grooves could not provide low-friction tribomaterial and the friction coefficient in the non-patterned zones was higher; consequently, so was the average friction. These assumptions are in clear agreement with the wear and Raman results obtained with sample F, where a low-friction tribolayer could be progressively built when the sliding took place on the polished regions of the substrate, and progressively destroyed in patterned area (see Fig. 6.21). Furthermore, all other tested samples where the grooves spacing is even lower (i.e. samples C, D, and E) exhibited much higher friction and wear than non-patterned samples (see comparison in Fig. 6.22).

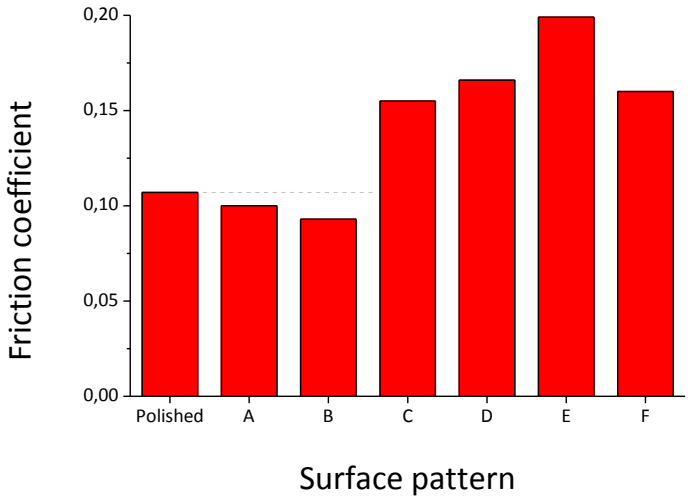

Fig. 6.22 Average friction coefficients for different surface patterns under the same test conditions.

The data presented in this Chapter suggest that there is an optimum distribution of patterned grooves for decreasing steady-state friction and wear. The rough shapes of the wear tracks and the cross-section variations made it difficult to design a precise wear model. Nevertheless, the wear as a function of the distance from the groove was successfully fitted using the following equation:

$$A_c(d) = A_{max} \cdot \left(1 - B_w^{\frac{-d.L}{s}}\right)$$

where A_c is the cross-section area; A_{max} is the stabilization value; d is the distance from the previous groove; L is the load; s is the linear speed; and B_w is a constant depending the width of the groove (and other influences). With more experimental data, it should be possible to predict optimum distribution and width of grooves to achieve minimum values of friction and wear for a given self-lubricant coating.

7 TMD coatings doped with carbon and titanium

Two series of coatings were deposited by r.f. magnetron co-sputtering using two targets: one Ti target and one C target with pellets of either WS_2 or MoS_2. Both series were prepared very similarly, depositing coatings of varying Ti content by keeping the power in the C+TMD target constant (at 600 W) and varying the power in the Ti target. Ti content was directly related to the target power ratios, as shown in Fig. 7.1. Due to difference in sputtering yields, the coatings had similar thickness (≈ 2.4 μm for W-S-C-Ti, ≈ 2.6 μm for Mo-S-C-Ti) despite the deposition time being considerably shorter for Mo-S-C-Ti (120 min) than for W-S-C-Ti (150 min). A thin Ti interlayer was deposited on the substrates before the solid lubricant films.

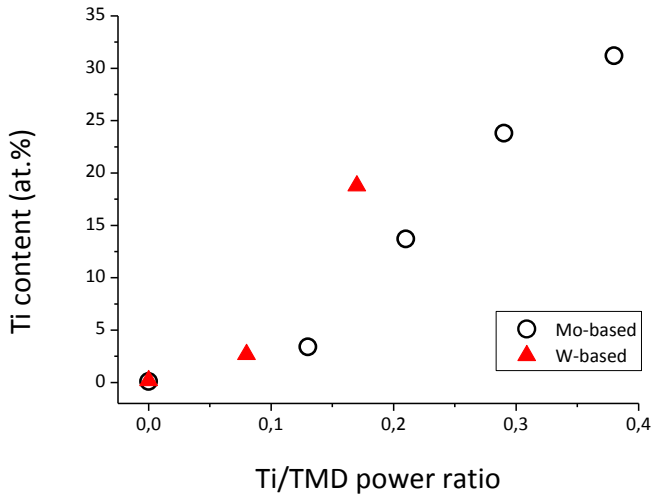

Fig. 7.1 Relation between TMD/Ti power ratio and Ti content.

The ratio between C and TMD content was higher with increasing Ti content (see Table 4). The number of TMD pellets on the graphite target was fixed, therefore it could be expected that the C/TMD ratio would not change. However, it is likely that the significant change in the power of the Ti target influenced the occurrence of re-sputtering on the substrates; since the probability of re-sputtering depends on each element, the final C/TMD ratio could change between depositions even if only the power to the Ti target was altered. The difference in the content ratio could then be explained. The S/M (M = Metal, i.e. Mo or W) ratio of W-S-C-Ti films was lower than that of Mo-S-C-Ti ones (around 1.0 and 1.5, respectively).

Table 4 Chemical composition of selected Mo/W-S-C-Ti films.

Film		Chemical composition (at.%)					C/TMD
		Mo	W	S	C	Ti	
Mo-S-C	0Ti	22.1	--	32.1	45.7	0.1	2.1
	3Ti	20.3	--	29.0	47.3	3.4	2.3
	14Ti	17.7	--	24.9	43.7	13.7	2.5
	24Ti	14.4	--	22.7	39.1	23.8	2.7
	31Ti	12.8	--	19.9	36.1	31.2	2.8
W-S-C	0Ti	--	26.7	28.7	44.4	0.2	1.7
	3Ti	--	23.7	26.2	47.4	2.7	2.0
	19Ti	--	16.8	18.9	45.5	18.8	2.7

7.1 Mechanical and tribological properties

Hardness of Mo-S-C-Ti coatings varied between 4.5 and 7.9 GPa; for W-S-C-Ti, the values were between 5.0 and 8.4 GPa. In both cases, hardness increased with Ti content, as shown in Fig. 7.2. In general, the films exhibited low adhesion and limited tribological performance: none of the coatings was able to sustain sliding tests for more than 25000 cycles under 5 N load. Although the original idea behind the incorporation of reactive metals such as Ti expected protection of the pure TMD phase from oxidation [28] and increasing wear resistance, other studies [81,105,106] have observed the deterioration of the wear resistance of Ti-doped TMD coatings, particularly associated with high Ti content. It has been suggested in Ref. [105] that this is due to the formation

of hard metallic titanium nanoparticles.

There was no apparent relation between Ti content and friction coefficients in our results, neither for films with Mo nor for films with W. Tests performed on W-S-C-Ti films with varying load showed decreasing friction when applying higher loads (Fig. 7.3), a behaviour matching those observed with other doped-TMD systems described so far.

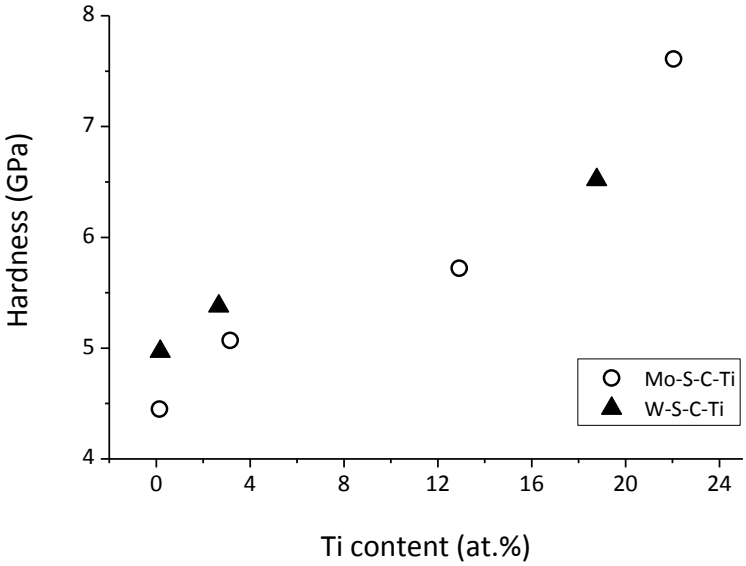

Fig. 7.2 Hardness values by Ti content.

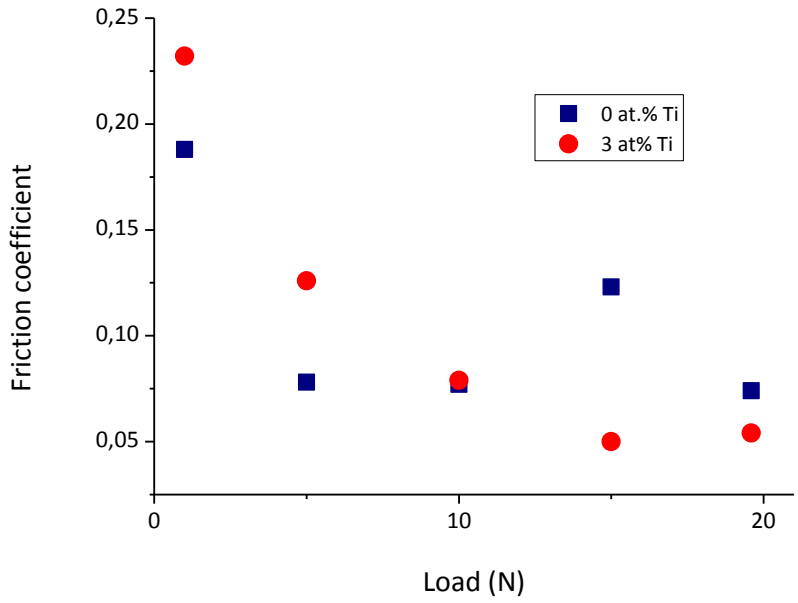

Fig. 7.3 Friction coefficient of W-S-C-Ti with increasing contact load.

7.2 Chemical bonding and microstructure

The Raman spectra of W/Mo-S-C-Ti films were dominated by the D and G peaks related to carbon, with low-intensity peaks at lower wavelengths and broad peaks related to oxides in the middle range (600–900 cm^{-1}). In Ref. [107], the occurrence of titanium carbide is associated in Raman spectra with peaks at approximately 146, 396, 515 and 636 cm^{-1}, with additional peaks associated with Ti-O in the same region, although these peaks are only visible in spectra acquired after annealing. In our W/Mo-S-C-Ti films, peaks at ~150 cm^{-1} were observed in all spectra. However, the region below ~200 cm^{-1} often presented unidentified peaks, as discussed before for other compositions. The most intense TiC-related peak expected close to 636 cm^{-1} was not observed. Other TiC-related peaks were either absent or indistinguishable from the TMD-related ones in the region between approximately 250 and 500 cm^{-1}. Nevertheless, this region was relatively shapeless, indicating there might be a contribution of bonds besides those related to W/Mo-S. In Ref. [108], the authors analyse the Raman spectra of carbide-based carbon films (including TiC) solely by the D and G peaks. The main indicator of the formation of carbides in that work is the decrease of FWHM (full width at half maximum) values in the D and G peaks, evidencing ordering of carbon bonds. This behaviour was also observed in the spectra of our W/Mo-S-C-Ti films (see Fig. 7.4), although the values were almost independent of Ti contents.

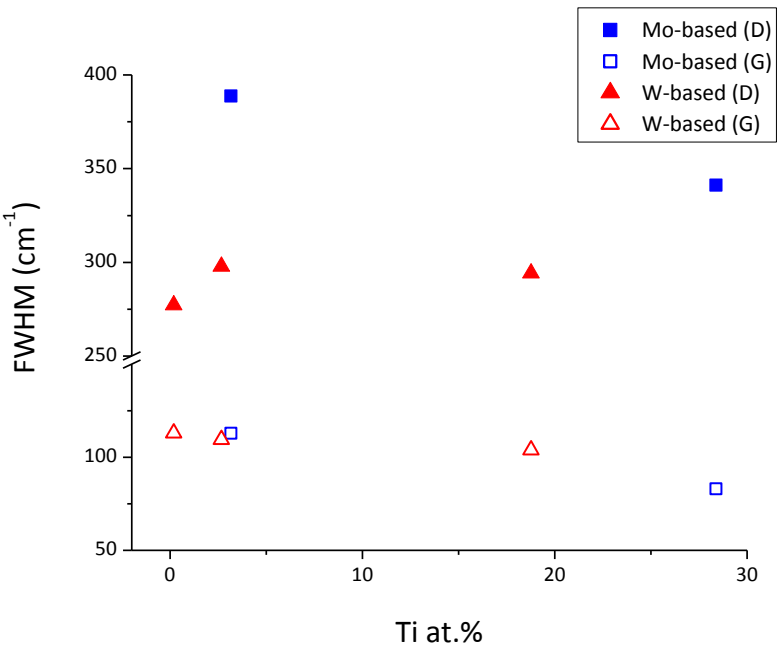

Fig. 7.4 Changes in FWHM of D and G peaks in the Raman spectra of W/Mo-S-C-Ti films.

Analysis of W-S-C-Ti films by XRD revealed that for low-Ti films, the spectra showed the usual features – broad asymmetric peak indicating (10*L*) planes. When the Ti content increased, however, there was the predominance of peaks which matched the diffraction angles corresponding to titanium carbide at ~40°, 46° and 68°. Since not all coatings analysed by XRD had their Ti atomic percentage determined due to adhesive failures, the data in Fig. 7.5 is shown according to deposition power.

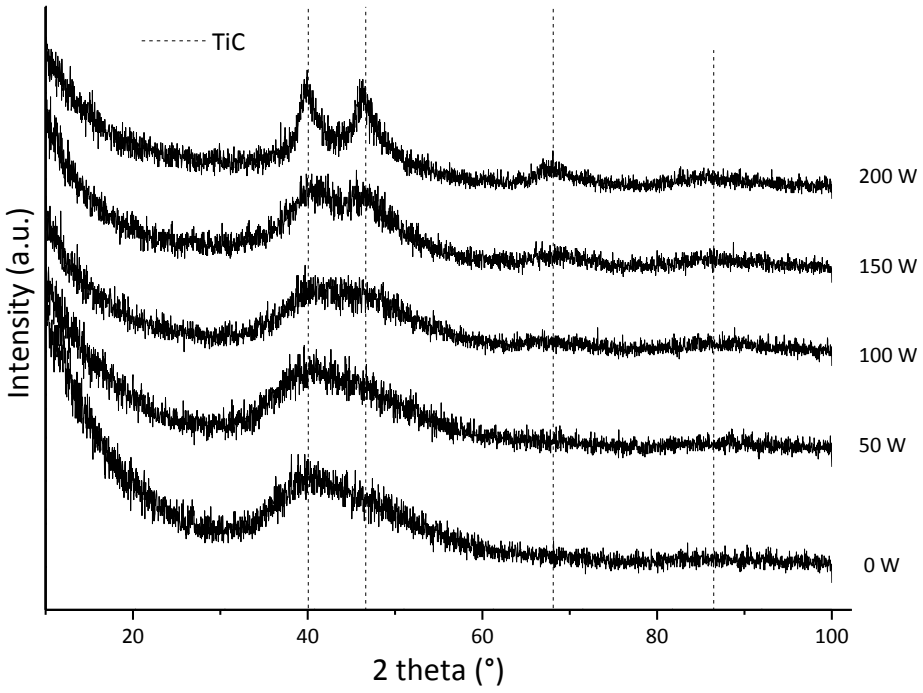

Fig. 7.5 XRD spectra for increasing Ti deposition power.

The evolution of the XRD spectra suggested that the TiC peaks observed should be associated with Ti in the coating – not (only) with the interlayer, which was approximately equal in all depositions. It seems that the co-deposition with Ti led to the formation of TiC grains in the film, although in low structural quality.

7.3 Comparison with other systems

The increase in dopant was associated, in the others series presented in this work, with the resulting films being more amorphous, thus improving both hardness and adhesion. Comparing W/Mo-S-

C with the present case of W/Mo-S-C-Ti, it can be seen that while the additional doping with Ti resulted in hardness values similar or greater than those doped only by C, the adhesion was significantly worse. It must be noted that although there was an increase in hardness associated with dopant content in W/Mo-S-C-Ti coatings, adhesion followed the same trend only for W-S-C-Ti. Thus, the results suggest that the adhesion problems could be a consequence of factors (partially) unrelated to the composition. In fact, it was shown previously [31], that a Ti interlayer improves adhesion of W-S-C films through formation of a very thin carbide layer, see Fig. 7.6. During the deposition of W-S-C-Ti (carried out later) we observed that the base pressure was higher than a certain value resulted in poor film adhesion regardless of dopant content. It is likely that doping with C and Ti could still result in coatings with good mechanical and tribological properties, at least comparable to those observed in other compositions, provided the deposition is fully optimized.

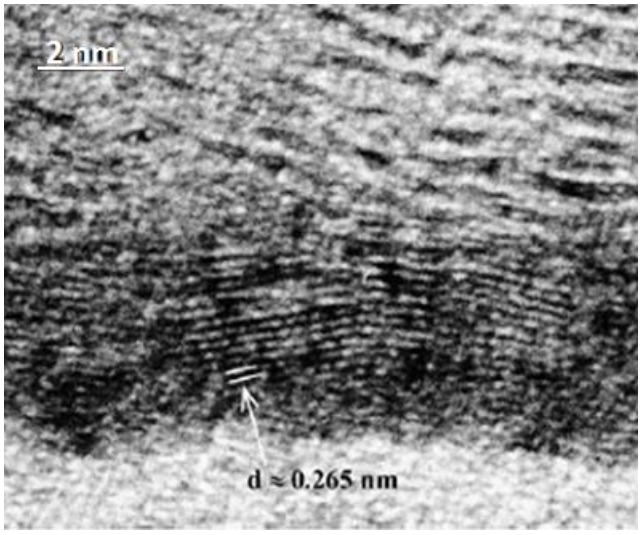

Fig. 7.6 TiC layer at the interface between Ti interlayer and W-S-C coating (from [31]).

8 Coatings based on molybdenum and tungsten diselenides

For low-friction applications, TMDs based on diselenides have not received as much attention as those based on disulfides. Nevertheless, studies with $MoSe_2$ have found it comparable with MoS_2, with the advantage of being more resistant to the detrimental effect of humidity and having higher temperature stability [69,109]. Coatings composed of Mo/W-Se-C (molybdenum or tungsten diselenide doped with carbon) have also been shown to exhibit good tribological results and higher hardness values when compared to pure Mo/WSe_2 [26, 110]. However, the tribological performance of the diselenide-based coatings examined in this work was often seriously hindered by low adhesion to the steel substrates.

The coatings used had been deposited beforehand, either by co-sputtering C and Mo/WSe_2 or by reactive sputtering of WSe_2 in a CH_4 atmosphere. Several compositions were prepared, with varying carbon content.

8.1 Mechanical and tribological properties

Most of the Mo-Se-C coatings tested during the course of this work exhibited severe adhesion failures and did not withstand tribological tests under the conditions presented so far for other systems. Only one composition, with 14 at.% C, exhibited low friction (0.1) in a 5000-cycle test under 5 N. The wear track produced was rough with indications that the coating was locally worn

out in many spots. No further tests were carried out on this Mo-Se-C series.

After preliminary analysis, four compositions of W-Se-C were selected, with varying C content (see Table 5). Raman examination of the as-deposited coatings suggested a direct relation between carbon content and the ratio of C peaks (D and G) to the WSe_2 region (broad, poorly-defined peaks at approx. 253 cm^{-1}).

The W-Se-C coatings had low hardness (1.9 to 5.3 GPa) compared to the other systems studied. Although their adhesion was not quantified, very few of the coatings survived tribological tests in the standard conditions of 5 N for 5000 cycles. Therefore we tried to evaluate the coatings in milder conditions: tribological tests were carried out with a load of 1 N, since it was apparent that these coatings could not withstand higher loads. Furthermore, the tests were carried out only until 500 cycles. For these conditions using 6-mm 100Cr6 balls, the friction coefficients were between 0.14 and 0.4. The coatings with high C content exhibited higher friction. Wear rates were higher than those of W-S-C, around 1.5×10^{-6} mm^3/Nm.

Table 5 Chemical composition of selected W-Se-C films.

Deposition method	Chemical composition (at.%)		
	W	Se	C
Co-sputtering	33.8	29.9	36.3
Co-sputtering	15.5	15.4	69.1
Reactive CH_4	22.4	51.6	26.0
Reactive CH_4	11.7	20.2	68.1

8.1.1 Effect of contact pressure on the frictional behaviour

In order to verify if the W-Se-C coatings also exhibited the decrease in friction with increasing load observed in other systems, an alternative approach was used: tests with constant load using as contact partners balls of different diameters (6.0, 7.94, and 10.0 mm). The contact pressure was thereby lower with larger diameters, since the contact area was larger, and we expected to see a decrease in friction associated with smaller diameters (i.e. increasing the contact pressure). This was verified only in some of the tests. The main issue here was that the tests had to be so short that they probably did not span the entire running-in period before the coating was worn out. Since friction in these conditions is usually high in the initial stages of sliding, tests too short would not be representative of the friction-contact pressure relation which was expected in the steady state.

Furthermore, during the first laps of sliding the contact area was usually very small, and the wear tracks were initially characterised by scratches and polishing of the wear track area (as seen by the *in situ* monitoring carried out with W-S-C-Cr films). Thus, our assumptions that the contact area is proportional to the diameter of the ball may not be valid until further stages of the sliding process.

Results obtained later (outside of the scope of this work) by Polcar et al., in Ref. [111], verified lower friction for increasing loads in MoSe-based sputtered coatings with higher C content (47 and 61 at.%). They have also observed lower friction for higher C content.

9 Discussion

We were able to verify common traits among the different compositions which helped elucidate the characteristics of tribological TMD films in general. A comparison of the main properties assessed in our analyses of the different systems is presented in Table 6. Since all of the series except for W–S–C had their compositions varied in different depositions, the films compared in Table 6 were chosen for medium dopant content. (The chemical composition of W-S-Cr was estimated from deposition parameters, see Chapter 5.) The friction coefficients are presented for tests in humid air, under 5 N for 5000 cycles.

Table 6 Comparison of results obtained with different series.

Composition	Deposition method	W or Mo at.%	S at.%	C at.%	Ti or Cr at.%	Hardness (GPa)	Friction coefficient	Critical load (N)
W–S–C	d.c. co-sputtering	26	32	42	--	9.0	0.073	9.0
W–S–Cr	d.c. co-sputtering	27	35	--	38	3.4	0.108	n/a
W–S–C–Cr	r.f. co-sputtering + pellets	20	24	41	15	7.2	0.107	22.5
W–S–C–Ti	r.f. co-sputtering + pellets	17	19	45	19	6.5	0.088	7.0
Mo–S–C–Ti	r.f. co-sputtering + pellets	18	25	44	13	5.7	0.117	< 4.0
Mo–S–C	r.f. co-sputtering	17	28	55	--	4.0	0.088	< 8.3

An interesting point observed in the deposition and characterisation procedures was the correlation between target power ratios, chemical composition, and peak intensities in Raman spectra. Although their interdependence was not thoroughly examined or quantified, it is clear that these factors are almost linearly related. This is an interesting observation from an experimental point of view, since it suggests that a) given certain conditions, the final chemical composition of doped films could be controlled by a single deposition parameter; and b) we were able to observe changes in the film material, such as those observed during sliding tests, using a relatively fast and non-destructive technique, without restrictive requirements of measuring environment or sample preparation.

9.1 On the adhesion of the films studied and their durability

Among the compositions in this work, it was apparent that the main obstacle hindering tribological performance of thin films based on doped TMDs was the quality of adhesion to the substrate. If we select the coatings with good enough adhesion for tribological testing, most compositions exhibited low friction coefficient, below 0.12, for tribological tests in humid air. As discussed for W-S-Cr in Chapter 5 and W-S-C-Ti in Chapter 7, poor adhesion (and cohesion) was more associated with the deposition process – the chamber pressure in particular – than with the chemical composition. The mid to high percentages of dopant used were enough to ensure more amorphous coatings with improved hardness even when adhesion was not satisfactory. Simmonds et al. [112] deposited MoS_2 films co-sputtered with Au, Ti, Cr or WSe_2, in various concentrations, and tested them in similar conditions. They observed that while dopant concentration is vital to film performance, the optimum level of dopant content was different for each material. In fact, the severe differences in wear rates suggested that doping with Ti and Cr led to different wear mechanisms. Furthermore, an interesting observation was that for all four compositions the concentration that exhibited the lowest friction coefficient was not the concentration with the longest lifetime. In our results, on the other hand, the lowest friction was usually associated with the highest durability. However, it should be noted that there were six or more variations of composition with each dopant in Ref. [112]; therefore we cannot exclude the possibility of that behaviour as a general rule, since we have insufficient number of different dopants.

Ogilvy et al. [113] developed a simple wear model, associated with a contact model, to predict the durability of MoS_2 films. The model comprised extremely large fluctuations in film lifetimes, yet still experimental values did not fall within the prediction. One reason was likely because the model did not consider the transfer of tribomaterial during sliding. A later simulation by Onodera et al. [114] of the tribochemical reactions of MoS_2 predicted the self-organization of an initially amorphous MoS_2 layer into a tribofilm. Their modelling of the sliding process under certain conditions predicted a running-in followed by steady state very similar to that exhibited by most of our coatings. However, their models made no prediction of durability.

Although the self-healing characteristic of our coatings was verified, with tribomaterial accumulating on areas where it had been previously worn out or had not been formed (as in the case of patterned W-S-C-Cr samples), it can be assumed that adhesive and/or cohesive problems contributed to increasing friction and, in particular, lowering wear rates.

9.2 On oxygen contamination

Another important factor influencing the tribological performance of these self-lubricant coatings was oxidation. It was already known that humid atmospheres hindered their performance. The absence of oxygen in the outermost layer can be important to achieve lower friction [19], although superficial oxidation should be easily and quickly worn away and not have a lasting influence, as shown by the case of Mo-S-C. In the majority of sliding tests with all systems in humid air, the highest friction was observed in the initial laps and it is assumed that most superficial oxidation was worn away at this stage. It has often been considered that metal dopants in TMD coatings would have a beneficial role in that they would react preferentially with the residual atmosphere; the metals would oxidize and thus protect the TMD phases [11]. In the analyses of W-S-Cr and W-S-C-Cr in this work, there was evidence of Cr_2O_3 (and Cr carbide) on or below the surface, although XPS indicated that oxygen was bonded mostly to W. The same applies to W-S-C-Ti and Ti oxides/carbides. These systems exhibited higher friction and wear rates than W-S-C. This can surely be attributed in part to adhesive/cohesive problems, as described earlier (it should be noted, however, that the critical load of W-S-C-Cr films was much higher than that of W-S-C). The second detrimental influence on tribological properties is likely oxidation, but the comparison of our results obtained with different systems show a complex picture and does not allow a clear general

conclusion regarding the presence of metals in the material. There is no doubt that, when compared to pure TMDs, using of metals as dopants can improve tribological performance (although often not as much as using only carbon). Nevertheless, our studies indicate that the presence of oxides below the surface of the material can not only increase friction, but also have a more detrimental effect in generating abrasive wear – and the effect would be heightened in the case of hard oxides such as Cr_2O_3.

In [95], Polcar et al. performed tribological tests on the same W-S-C-Cr coatings presented in this work, then removed a cross-section of the wear track using focused ion beam (FIB) and analysed it by TEM. It was found that, while the top of the tribolayer of W-S-C coatings was composed primarily of WS_2, W-S-C-Cr coatings contain mainly oxides on the interface at the top of the wear track, and consequently exhibit higher friction coefficients. TEM of the cross-sections revealed that the tribolayer was mostly amorphous but with crystalline WS_2 phases in some areas. While there was no indication of the crystalline WS_2 phase at the outermost surface of the wear track produced in humid air, the interface between the tribolayer and coating showed a layer of WS_2 with basal planes parallel to the surface. In dry air, in contrast, on the topmost surface was a distinct layer of (002) oriented WS_2. Further analysis showed high content of iron and tungsten oxides in the amorphous-like layer in the tribomaterial.

A similar analysis of W-S-N films was carried out again more recently [115], on a wear track produced in humid air (RH 10%) and the corresponding counterpart. The authors found a thin layer of WS_2 in the (002) orientation covering the outermost surface of the entire track. Beneath this layer was a *quasi*-amorphous phase with WS_2 platelets and WO_3 nanograins. Further down under the *quasi*-amorphous layer were found WS_2 platelets, again with (002) basal planes parallel to the surface. On the counterpart, a similar distribution was found in the transfer film. Raman investigation showed similar results to those presented in this work for W-S-C: a maximum of WS_2 peaks in the centre of the wear track, and lower towards the as-deposited coating. The opposite trend was observed for WO_3. Despite a clear TEM observation of WS_2 planes, the presence of oxygen in the topmost layers could not be ruled out by the experimental analyses. The authors argued that whatever oxygen was present in the contact, it should not be tungsten oxide, but rather substitution of sulfur in WS_2 crystals. In other words, $WS_{2-x}O_x$ is created; in such case the low-friction characteristic would not be compromised, as described by Fleischauer and Lince for MoS_2 (see section 2.1).

The presence of oxides between the interface of the coating and the topmost WS_2 layer was tentatively explained by using a simple model of molecular dynamics developed by Rigney et

al. [116]. The hypothesis is that when the sliding of the hard ball is taking place with two separate layers (WS_2 and oxides), the sliding interface will be the softer WS_2. When this layer is removed, the sliding interface moves to the oxide layer. Then the oxides are mechanically mixed with coating material. The WS_2 in this mix is then moved upwards to the contact interface, and thus the well-oriented WS_2 layer can be found once again. In [117], Polcar and Cavaleiro analysed various carbon-doped TMD films (in particular W-S-C and Mo-Se-C) using, among other methods, TEM of wear track cross sections. They also revealed platelets of TMD aligned parallel to the surface. The authors concluded that the oriented TMD layers that could be observed on the surface were not generated by agglomerated wear debris, but in fact must have risen to the surface already as aligned platelets.

Although the process is not yet fully understood, it seems clear that the self-adaptation of these films, promoting reorientation as a response to the sliding process, is the most crucial factor for their good tribological properties. The common characteristics of the doped-TMD films in the present work and the collection of results in the literature referred to above lead us to believe that a similar process could take place in most TMD-based systems.

Conclusion

Solid lubricant coatings based on doped TMDs were deposited and tested. Characterisation was carried out using various experimental techniques, among them new methods and innovative approaches. The films presented in this work were among the first solid lubricants to be analysed in our group's 3D optical profilometer and Raman spectrometer; they were furthermore the only ones so far to be examined with the equipment adapted for video monitoring and *quasi in-situ* acquisition of Raman spectra. While these approaches undoubtedly yielded important results in our analyses, they also revealed plenty of room for improvement in handling these techniques and equipment.

The characterisation and analyses of the films permitted further understanding of their mechanical properties and the mechanisms involved in friction against a static partner, including the role of the dopants on the formation of a low-friction tribolayer. The evolution of the sliding process in humid air was examined, as well as the effect of test parameters such as the contact load. The self-healing capacity of such films was also verified in different compositions and conditions.

Our results supported the hypothesis that a TMD-based coating can exhibit very good tribological performance in humid air with improved load-bearing capacity and improved adhesion, if co-sputtered with an adequate dopant material. The main role of the dopant is not direct reaction with the TMD phase, but rather to prevent the formation of large grains and defects, rendering the coating dense and amorphous.

The deposition of doped TMD coatings by magnetron sputtering allowed an improvement in load-bearing capacity and tribological properties in comparison with pure TMD films, particularly in humid air. The main drawback observed overall was low adhesion, which our results indicate can be solved or minimized in the future with optimization of the deposition process.

References

[1] Gwidon W. Stachowiak, and Andrew W. Batchelor, *Engineering Tribology*, 2nd Ed., Butterworth-Heinemann, 2001.

[2] M. Changizi, R. Weber, R. Kotecha, and J. Palazzo. Are wet-induced wrinkled fingers primate rain treads?, *Brain Behav. Evol.* 77 (2011) 286.

[3] Yu. N. Drozdov, N. V. Lukashina, and T. I. Nazarova. Using the achievements in tribology for teaching technical disciplines, *J. Mach. Manuf. Reliab.* 40 (2011) 97.

[4] Bharat Bhushan, *Principles and Applications of Tribology*, John Wiley & Sons, 1999.

[5] Ali Erdemir, Julien Fontaine, and Cristophe Donnet, "An Overview of Superlubricity in Diamond-like Carbon Films", in: Christophe Donnet, Ali Erdemir (Eds.), *Tribology of diamond-like carbon films: fundamentals and applications*, Springer, 2008.

[6] S. Hogmark, S. Jacobson, and M. Larsson. Design and evaluation of tribological coatings, *Wear* 246 (2000) 20.

[7] A. A. Voevodin, J. P. O'Neill, and J. S. Zabinski. Nanocomposite tribological coatings for aerospace applications, *Surf. Coat. Technol.* 116-119 (1999) 36.

[8] A. A. Voevodin, and J. S. Zabinski. Nanocomposite and nanostructured tribological materials for space applications, *Compos. Sci. Technol.* 65 (2005) 741.

[9] C. Donnet, and A. Erdemir. Historical developments and new trends in tribological and solid lubricant coatings, *Surf. Coat. Technol.* 180-181 (2004) 76.

[10] L. Rapoport, V. Leshchinsky, Y. Volovik, M. Lvovsky, O. Nepomnyashchy, Y. Feldman, R. Popovitz-Biro, and R. Tenne. In Oil: Modification of contact surfaces by fullerene-like solid lubricant nanoparticles, *Surf. Coat. Technol.* 164/164 (2003) 405.

[11] A. R. Lansdown, *Molybdenum Disulfide Lubrication*, Elsevier, 1999.

[12] H. Waghray, T.-S. Lee, and B. J. Tatarchuk. A study of the tribological and electrical properties of sputtered and burnished transition metal dichalcogenide films, *Surf. Coat. Technol.* 76-77 (1995) 415.

[13] C. Donnet, and A. Erdemir. Solid lubricant coatings: recent developments and future trends, *Tribol. Lett.* 17 (2004) 389.

[14] J. S. Zabinski, M. S. Donley, V. J. Dyhouse, and N. T. McDevitt. Chemical and tribological characterization of PbO-MoS2 films grown by pulsed laser deposition, *Thin Solid Films* 214 (1992) 156.

[15] A. A. Voevodin, and J. S. Zabinski. Supertough wear-resistant coatings with 'chameleon' surface adaptation, *Thin Solid Films* 370 (2000) 223.

[16] T. Spalvins. Frictional and morphological properties of Au–MoS2 films sputtered from a compact target, *Thin Solid Films* 118 (1984) 375.

[17] K. J. Wahl, L. E. Seitzmann, R. N. Bolster, and I. L. Singer. Low-friction, high-endurance, ion-beam-deposited Pb-Mo-S coatings, *Surf. Coat. Technol.* 73 (1995) 152.

[18] M. Evaristo, T. Polcar, and A. Cavaleiro. Tribological behaviour of C-alloyed transition metal dichalcogenides (TMD) coatings in different environments, *Int. J. Mech. Mater. Des.* 4 (2008) 137.

[19] T. Polcar, and A. Cavaleiro. Self-adaptive low friction coatings based on transition metal di-chalcogenides, *Thin Solid Films* 519 (2011) 4037.

[20] P. D. Fleischauer. Fundamental aspects of the electronic structure, materials properties and lubrication performance of sputtered MoS2 films, *Thin Solid Films* 154 (1987) 309.

[21] E. Benavente, M.A. Santa Ana, F. Mendizábal, and G. González. Intercalation chemistry of molybdenum disulfide, *Coord. Chem. Rev.* 224 (2002) 87.

[22] J. M. Martin, C. Donnet, Th. Le Mogne, and Th. Epicier. Superlubricity of molybdenum di-sulfide, *Phys. Rev. B* 48 (1993) 10583.

[23] T. Onodera, Y. Morita, R. Nagumo, R. Miura, A. Suzuki, H. Tsuboi, N. Hatakeyama, A. Endou, H. Takaba, F. Dassenoy, C. Minfray, L.Joly-Pottuz, M. Kubo, J. M. Martin, and A. Miyamoto. A Computational Chemistry Study on Friction of h-MoS2. Part II. Friction Anisotropy, J. Phys. Chem. B 114 (2010) 15832.

[24] M. Hirano, and K. Shinjo. Superlubricity and frictional anisotropy, *Wear* 168 (1993) 121.

[25] K. Shinjo, and M. Hirano. Dynamics of friction: superlubric state, Surf. Sci. 283 (1993) 473.

[26] T. Polcar, M. Evaristo, M. Stueber, and A. Cavaleiro. Synthesis and structural properties of Mo–Se–C sputtered coatings, *Surf. Coat. Technol.* 202 (2008) 2418.

[27] S. V. Prasad, N. T. McDevitt, and J. S. Zabinski. Tribology of tungsten disulfide films in humid environments: The role of a tailored metal-matrix composite structure, *Wear* 230 (1999) 24.

[28] P. D. Fleischauer, and J. R. Lince. A comparison of oxidation and oxygen substitution in MoS2 solid film lubricants, *Tribo. Int.* 32 (1999) 627.

[29] Lucile Joly-Pottuz, and Fabrice Dassenoy, "Nanoparticles made of metal dichalcogenides", in: Jean M. Martin, Nobue Ohmae (Eds.), *Nanolubricants*, Wiley-Blackwell, 2008.

[30] T. Onodera, Y. Morita, A. Suzuki, M. Koyama, H. Tsuboi, N. Hatakeyama, A. Endou, H. Takaba, M. Kubo, F. Dassenoy, C. Minfray, L. Joly-Pottuz, J. M. Martin, and A. Miyamoto. A Computational Chemistry Study on Friction of h-MoS2. Part I. Mechanism of Single Sheet, *J. Phys. Chem. B* 113 (2009) 16526.

[31] A. Nossa, and A. Cavaleiro. Chemical and physical characterization of C(N)-doped W–S sputtered films, *J. Mater. Res.* 19 (2004) 2356.

[32] A. Nossa, A. Cavaleiro, N. J. M. Carvalho, B. J. Kooi, and J. Th. M. De Hosson. On the

microstructure of tungsten disulfide films alloyed with carbon and nitrogen, *Thin Solid Films* 484 (2005) 389.

[33] A. Nossa, and A. Cavaleiro. The influence of the addition of C and N on the wear behaviour of W-S-C/N coatings, *Surf. Coat. Technol.* 142-144 (2001) 984.

[34] T. Polcar, M. Evaristo, and A. Cavaleiro. Friction of Self-Lubricating W-S-C Sputtered Coatings Sliding Under Increasing Load, *Plasma Process. Polym.* 4 (2007) S541.

[35] T. Polcar, M. Evaristo, and A. Cavaleiro. Self-Lubricating W–S–C Nanocomposite Coatings, *Plasma Process. Polym.* 6 (2009) 417.

[36] S. Watanabe, J. Noshiro, and S. Miyake. Tribological characteristics of WS2/MoS2 solid lubricating multilayer films, *Surf. Coat. Technol.* 183 (2004) 347.

[37] Andrey A. Voevodin, "Hard DLC Growth and Inclusion in Nanostructured Wear-protective Coatings", in: Christophe Donnet, Ali Erdemir (Eds.), *Tribology of diamond-like carbon films: fundamentals and applications*, Springer, 2008.

[38] T. Polcar, M. Evaristo, and A. Cavaleiro. Comparative study of the tribological behavior of self-lubricating W–S–C and Mo–Se–C sputtered coatings, *Wear* 266 (2009) 388.

[39] Hans-Jürgen Butt, Karlheinz Graf, and Michael Kappl, *Physics and Chemistry of Interfaces*, Wiley-VCH, 2003.

[40] John A. Small, Dale E. Newbury, and John T. Armstrong, "Electron-Induced X-ray Emission", in: René E. Van Grieken, Andrzej A. Markowicz (Eds.), *Handbook of X-Ray Spectrometry*, 2nd Ed, Marcel Dekker, 2002.

[41] David Brandon, and Wayne D. Kaplan, *Microstructural Characterization of Materials*, 2nd Ed., John Wiley & Sons, 2008.

[42] CAMECA Science & Metrology Solutions, Electron Probe Micro-Analysis, 2010. (Available at: http://www.cameca.com/instruments-for-research/epma.aspx)

[43] CSM Instruments, Applications Bulletin n°18 – Overview of Mechanical Testing Standards, 2002.

[44] J. Neidhardt, L. Hultman, E. Broitman, T.W. Scharf, and I.L. Singer. Structural, mechanical and tribological behavior of fullerene-like and amorphous carbon nitride coatings, *Diamond. Relat. Mater.* 13 (2004) 1882.

[45] British Standards Institute, EN 1071-3:2002 Advanced technical ceramics – Methods of test for ceramic coatings – Part 3: Determination of adhesion and other mechanical failure modes by a scratch test, 2002.

[46] S. Ramalingam, and L. Zheng. Film-substrate interface stresses and their role in the tribological performance of surface coatings, *Tribol. Int.* 28 (1995) 145.

[47] CSM Instruments, CSM Calotest User Guide, 1998.

[48] J. Calatroni, A. L. Guerrero, C. Sainz, and R. Escalona. Spectrally-resolved white-light interferometry as a profilometry tool, *Opt. Laser Technol.* 28 (1996) 485.

[49] Zygo Corporation, NewViewTM 7200 Specifications, 2008.

[50] John R. Ferraro, Kazuo Nakamoto, and Chris W. Brown, *Introductory Raman Spectroscopy*, 2nd Ed, Elsevier, 2003.

[51] Wieland Hill, "Surface Raman Spectroscopy", in: Henning Bubert, Holger Jenett (Eds.), *Surface*

and Thin Film Analysis, Wiley VCH, 2002.

[52] Joseph B. Slater, James M. Tedesco, Ronald C. Fairchild, and Ian R. Lewis, "Raman Spectroscopy and the Industrial Environment", in: Ian R. Lewis, H. Edwards (Eds.), *Handbook of Raman Spectroscopy: from the research laboratory to the process line*, CRC Press, 2001.

[53] Mario Birkholz, *Thin Film Analysis by X-Ray Scattering*, Wiley-VCH, 2006.

[54] Mario Birkholz, and Christoph Genzel, "Residual Stress Analysis", in: Mario Birkholz, *Thin Film Analysis by X-Ray Scattering*, Wiley-VCH, 2006.

[55] P. S. Prevéy, *X-ray diffraction residual stress techniques*, Lambda Technologies, 1986.

[56] M. A. Baker, R. Gilmore, C. Lenardi, and W. Gissler. XPS investigation of preferential sputtering of S from MoS2 and determination of MoSx stoichiometry from Mo and S peak positions, *Appl. Surf. Sci.* 150 (1999) 255.

[57] M. Evaristo, T. Polcar, and A. Cavaleiro. Synthesis and properties of W–Se–C coatings deposited by PVD in reactive and non-reactive processes, *Vacuum* 83 (2009) 1262.

[58] B. Vincent Crist, *Handbook of Monochromatic XPS Spectra*, Wiley-Blackwell, 2000.

[59] K. Baba, and R. Hatada. Preparation and properties of metal-containing diamond-like carbon films by magnetron plasma source ion implantation, *Surf. Coat. Technol.* 196 (2005) 207.

[60] L. Ji, H. Li, F. Zhao, J. Chen, and H. Zhou. Microstructure and mechanical properties of Mo/DLC nanocomposite films, *Diamond Relat. Mater.* 17 (2008) 1949.

[61] N. M. D. Brown, N. Y. Cui, and A. McKinley. An XPS study of the surface modification of natural MoS2 following treatment in an RF-oxygen plasma, *Appl. Surf. Sci.* 134 (1998) 11.

[62] L. Benoist, D. Gonbeau, G. Pfister-Guillouzo, E. Schmidt, G. Meunier, and A. Levasseur. X-ray photoelectron spectroscopy characterization of amorphous molybdenum oxysulfide thin films, *Thin Solid Films* 258 (1995) 110.

[63] M. Regula, C. Ballif, J. Moser, and F. Lévy. Structural, chemical, and electrical characterisation of reactively sputtered WSx thin films, *Thin Solid Films* 280 (1996) 67.

[64] J. Moser, and F. Lévy. Random stacking in MoS2-x sputtered thin films, *Thin Solid Films* 240 (1994) 56.

[65] B. C. Windom, W. G. Sawyer, and D. W. Hahn. A Raman Spectroscopic Study of MoS2 and MoO3: Applications to Tribological Systems, *Tribol. Lett*. 42 (2011) 301.

[66] J. Robertson. Diamond-like amorphous carbon, *Mat. Sci. Eng. R* 37 (2002) 129.

[67] A. C. Ferrari, "Non-destructive Characterisation of Carbon Films", in: Christophe Donnet, Ali Erdemir (Eds.), *Tribology of diamond-like carbon films: fundamentals and applications*, Springer, 2008.

[68] P. K. Chu, and L. Li. Characterization of amorphous and nanocrystalline carbon films, *Mater. Chem. Phys.* 96 (2006) 253.

[69] T. Kubart, T. Polcar, L. Kopecký, R. Novák, and D. Nováková. Temperature dependence of tribological properties of MoS2 and MoSe2 coatings, *Surf. Coat. Technol.* 193 (2005) 230.

[70] C. Donnet, J. M. Martin, Th. Le Mogne, and M. Belin. Super-low friction of MoS2 coatings in various environments, *Tribol. Int.* 29 (1996) 123.

[71] M. Evaristo, A. Nossa, and A. Cavaleiro. W–S–C sputtered films: Influence of the carbon

alloying method on the mechanical properties, *Surf. Coat. Technol.* 200 (2005) 1076.

[72] K. A. Beadle, R. Gupta, A. Mathew, J. G. Chen, and B. G. Willis. Chemical vapor deposition of phase-rich WC thin films on silicon and carbon substrates, *Thin Solid Films* 516 (2008) 3847.

[73] J.-P. Hirvonen, J. Koskinen, J. R. Jervis, and M. Nastasi. Present progress in the development of low friction coatings, *Surf. Coat. Technol.* 80 (1996) 139.

[74] S. R. Cohen, L. Rapoport, E. A. Ponomarev, H. Cohen, T. Tsirlina, R. Tenne, and C. Lévy-Clément. The tribological behavior of type II textured MX2 (M=Mo, W; X=S, Se) films, *Thin Solid Films* 324 (1998) 190.

[75] National Institute of Standards and Technology, NIST X-ray Photoelectron Spectroscopy Database, 2000. (URL: http://srdata.nist.gov/xps/)

[76] J. S. Zabinski, M. S. Donley, S. V. Prasad, and N. T. McDevitt. Synthesis and characterization of tungsten disulphide films grown by pulsed-laser deposition, *J. Mater. Sci.* 29 (1994) 4834.

[77] C. D. Wagner, W. H. Riggs, C. E. David, J. F. Moulder, and G. E. Muilenberg (Ed.), *Handbook of X-ray photoelectron spectroscopy*, Perkin-Elmer Corporation, 1979.

[78] D. V. Shtansky, T. A. Lobova, V. Yu. Fominski, S. A. Kulinich, I. V. Lyasotsky, M. I. Petrzhik, E. A. Levashov, and J. J. Moore. Structure and tribological properties of WSex, WSex/TiN, WSex/TiCN and WSex/TiSiN coatings, Surf. Coat. Technol. 183 (2004) 328.

[79] V. Yu. Fominski, R. I. Romanov, A. V. Gusarov, and J.-P. Celis. Pulsed laser deposition of antifriction thin-film MoSex coatings at the different vacuum conditions, Surf. Coat. Technol. 201 (2007) 7813.

[80] S. N. Grigoriev, V. Yu. Fominski, A. G. Gnedovets, and R. I. Romanov. Experimental and numerical study of the chemical composition of WSex thin films obtained by pulsed laser deposition in vacuum and in a buffer gas atmosphere, Appl. Surf. Sci. 258 (2012) 7000.

[81] T. W. Scharf, A. Rajendran, R. Banerjee, and F. Sequeda. Growth, structure and friction behavior of titanium doped tungsten disulphide (Ti-WS2) nanocomposite thin films, *Thin Solid Films* 517 (2009) 5666.

[82] P. M. Sousa, A. J. Silvestre, N. Popovici, and O. Conde. Morphological and structural characterization of CrO2/Cr2O3 films grown by Laser-CVD, *Appl. Surf. Sci.* 247 (2005) 423.

[83] J. E. Maslar, W. S. Hurst, W. J. Bowers, Jr., J. H. Hendricks, M. I. Aquino, and I. Levin. In situ Raman spectroscopic investigation of chromium surfaces under hydrothermal conditions, *Appl. Surf. Sci.* 180 (2001) 102.

[84] J.-W. Chung, Z. R. Dai, and F. S. Ohuchi. WS2 thin films by metal organic chemical vapor deposition, *J. Cryst. Growth* 186 (1998) 137.

[85] A. Blatter, M. Maillat, S.M. Pimenov, G. A. Shafeev, A. V. Simakin, and E. N. Loubnin. Lubricated sliding performance of laser-patterned sapphire, *Wear* 232 (1999) 226.

[86] M. Wakuda, Y. Yamauchi, S. Kanzaki, and Y. Yasuda. Effect of surface texturing on friction reduction between ceramic and steel materials under lubricated sliding contact, *Wear* 254 (2003) 356.

[87] P. Andersson, J. Koskinen, S. Varjus, Y. Gerbig, H. Haefke, S. Georgiou, B. Zhmud, and W. Buss. Microlubrication effect by laser-textured steel surfaces, *Wear* 262 (2007) 369.

[88] X. Wang, K. Adachi, K. Otsuka, and K. Kato. Optimization of the surface texture for silicon carbide sliding in water, *Appl. Surf. Sci.* 253 (2006) 1282.

[89] A. A. Voevodin, J. Bultman, and J. S. Zabinski. Investigation into three-dimensional laser processing of tribological coatings, *Surf. Coat. Technol.* 107 (1998) 12.

[90] A. A. Voevodin, and J. S. Zabinski. Laser surface texturing for adaptive solid lubrication, *Wear* 261 (2006) 1285.

[91] P. Basnyat, B. Luster, C. Muratore, A. A. Voevodin, R. Haasch, R. Zakeri, P. Kohli, and S. M. Aouadi. Surface texturing for adaptive solid lubrication, *Surf. Coat. Technol.* 203 (2008) 73.

[92] J. H. Zimmerman, C. G. Guleryuz, and J. E. Krzanowski. Fabrication and tribological properties of titanium nitride coatings incorporating solid lubricant microreservoirs, *Surf. Coat. Technol.* 202 (2008) 2023.

[93] A. Moshkovith, V. Perfiliev, D. Gindin, N. Parkansky, R. Boxman, and L. Rapoport. Surface texturing using pulsed air arc treatment, *Wear* 263 (2007) 1467.

[94] L.E. Rumaner, T. Tazawa, and F.S. Ohuchi. Compositional change of (0001) WS2 surfaces induced by ion beam bombardment with energies between 100 and 1500 eV, *J. Vac. Sci. Technol. A* 12 (1994) 2451.

[95] T. Polcar, F. Gustavsson, T. Thersleff, S. Jacobson, and A. Cavaleiro. Complex frictional analysis of self-lubricant W-S-C/Cr coating, *Faraday Discuss.* 156 (2012) 383.

[96] M. Oku, S. Suzuki, N. Ohtsu, T. Shishido, and K. Wagatsuma. Comparison of intrinsic zero-energy loss and Shirley-type background corrected profiles of XPS spectra for quantitative surface analysis: Study of Cr, Mn and Fe oxides, *Appl. Surf. Sci.* 254 (2008) 5141.

[97] P. Hoffman, H. Galindo, G. Zambrano, C. Rincón, and P. Prieto. FTIR studies of tungsten carbide in bulk material and thin film samples, *Mater. Charact.* 50 (2003) 255.

[98] C. Santato, M. Odziemkowski, M. Ulmann, and J. Augustynski, *J. Am. Chem. Soc.* 123 (2001) 10639.

[99] B.-H. Xu, B.-Z. Lin, Z.-J. Chen, X.-L. Li, and Q.-Q. Wang. Preparation and electrical conductivity of polypyrrole/WS2 layered nanocomposites, *J. Colloid Interf. Sci.* 330 (2009) 220.

[100] B. Adamczyk, O. Boese, N. Weiher, S.L.M. Schroeder, and E. Kemnitz. Fluorine modified chromium oxide and its impact on heterogeneously catalyzed fluorination reactions, *J. Fluorine Chem.* 101 (2000) 239.

[101] D. Adliene, J. Laurikaitiene, V. Kopustinskas, S. Meskinis, and V. Sablinskas. Radiation induced changes in amorphous hydrogenated DLC films, *Mat. Sci. Eng. B-Solid* 152 (2008) 91.

[102] M. Bouchard, D. C. Smith, and C. Carabatos-Nédelec. An investigation of the feasibility of applying Raman microscopy for exploring stained glass, *Spectrochim. Acta A* 68 (2007) 1101.

[103] X. Hou, and K.-L. Choy. Synthesis of Cr2O3-based nanocomposite coatings with incorporation of inorganic fullerene-like nanoparticles, *Thin Solid Films* 516 (2008) 8620.

[104] J. Álvarez-Garsía, J. Marcos-Ruzafa, A. Pérez-Rodríguez, A. Romano-Rodríguez, J. R. Morante, and R. Scheer. MicroRaman scattering from polycrystalline CuInS2 films: structural analysis, *Thin Solid Films* 361-362 (2000) 208.

[105] V. Rigato, G. Maggioni, A. Patelli, D. Boscarino, N. M. Renevier, and D.G. Teer. Properties of sputter-deposited MoS2/metal composite coatings deposited by closed field unbalanced magnetron sputter ion plating, *Surf. Coat. Technol.* 131 (2000) 206.

[106] M. Evaristo, A. Nossa, and A. Cavaleiro, The influence of the addition of Ti on the mechanical properties of W-S-Ti coatings, *Mater. Sci. Forum* 514 (2006) 687.

[107] L. Zhang, and R.V. Koka. A study on the oxidation and carbon diffusion of TiC in alumina–titanium carbide ceramics using XPS and Raman spectroscopy, *Mater. Chem. Phys.* 57 (1998) 23.

[108] S. Urbonaite, L. Hälldahl, and G. Svensson. Raman spectroscopy studies of carbide derived carbons, *Carbon* 46 (2008) 1942.

[109] E. Bergmann, G. Melet, C. Muller, and A. Simon-Vermot. Friction properties of sputtered dichalcogenide layers, *Tribol. Int.* 14 (1981) 329.

[110] M. Evaristo, T. Polcar, and A. Cavaleiro. Can W-Se-C coatings be competitive to W-S-C ones?, *Plasma Process. Polym.* 6 (2009) S92.

[111] F. Gustavsson, S. Jacbson, A. Cavaleiro, and T. Polcar. Frictional behavior of self-adaptive nanostructural Mo-Se-C coatings in different sliding conditions, *submitted for publication* (2013).

[112] M. C. Simmonds, A. Savan, E. Pflüger, and H. Van Swygenhoven. Mechanical and tribological performance of MoS2 co-sputtered composites, *Surf. Coat. Technol.* 126 (2000) 15.

[113] J. A. Ogilvy. Predicting the friction and durability of MoS, coatings using a numerical contact model, *Wear* 160 (1993) 171.

[114] Y. Morita, T. Onodera, A. Suzuki, R. Sahnoun, M. Koyama, H. Tsuboi, N. Hatakeyama, A. Endou, H. Takaba, M. Kubo, C. A. Del Carpio, T. Shin-yoshi, N. Nishino, A. Suzuki, and A. Miyamoto. Development of a new molecular dynamics method for tribochemical reaction and its application to formation dynamics of MoS2 tribofilm, *Appl. Surf. Sci.* 254 (2008) 7618.

[115] F. Gustavsson, S. Jacobson, A. Cavaleiro, and T. Polcar. Ultra-low friction and self-healing ability of W-S-N solid lubricant coating, *submitted for publication* (2013).

[116] D. A. Rigney, and S. Karthikeyan. The Evolution of Tribomaterial During Sliding: A Brief Introduction, *Tribol. Lett.* 39 (2010) 3.

[117] T. Polcar, and A. Cavaleiro. Review on self-lubricant transition metal dichalcogenide nano-composite coatings alloyed with carbon, *Surf. Coat. Technol.* 206 (2011) 686.

List of author's publications

Works related to the doctoral thesis

Peer-reviewed articles in impacted journals

[A.1] J. V. Pimentel, T. Polcar, and A. Cavaleiro. Structural, mechanical and tribological properties of Mo-S-C solid lubricant coating, *Surface and Coatings Technology* vol. 205 (2011), pages 3274–3279.
(Contribution: 45%)

[A.2] J. V. Pimentel, T. Polcar, M Evaristo, and A. Cavaleiro. Examination of the tribolayer formation of a self-lubricant W–S–C sputtered coating, *Tribology International* vol. 47 (2012), pages 188–193.
(Contribution: 50%)

Other publications

[A.3] J. V. Pimentel, M. Evaristo, A. Cavaleiro, and T. Polcar, "Tribological Behavior of Self-Lubricating Mo-S-C Coatings", *Twelfth International Conference on Plasma Surface Engineering (PSE 2010)*, Garmisch-Partenkirchen, Germany, Sep. 13-17, 2010.

[A.4] J. V. Pimentel, M. Evaristo, T. Polcar, and A. Cavaleiro, "Scratch Resistance of Self-Lubricating Thin Films Based on TMDs Alloyed with Carbon", *11th European Vacuum Conference (EVC-11)*, Salamanca, Spain, Sep. 20-24, 2010.

[A.5] M. Evaristo, J. V. Pimentel, T. Polcar, and A. Cavaleiro, "Characterization of TMD-C doped with Ti deposited by PVD Magnetron Sputtering", *11th European Vacuum Conference (EVC-11)*, Salamanca, Spain, Sep. 20-24, 2010.

[A.6] T. Vitu, J. V. Pimentel, P. Siroky, M. Evaristo, A. Cavaleiro, and T. Polcar, "W-doped carbon coatings - determination of friction and wear mechanisms", *8th Asian-European International Conference on Plasma Surface Engineering (AEPSE 2011)*, Dalian, China, Sep. 19-22, 2011.

[A.7] J. V. Pimentel, M. Evaristo, T. Polcar, and A. Cavaleiro, "Tungsten Disulphide Films Alloyed With Chromium Deposited by D.C. Magnetron Sputtering", *International Tribology Conference Hiroshima 2011 (ITC 2011)*, Hiroshima, Japan, Oct. 03 - Nov. 04, 2011.

[A.8] J. V. Pimentel, F. Gustavsson, T. Polcar, and A. Cavaleiro, "Effect of surface defects on the tribology of WSC-Cr self-lubricant coatings", *European Materials Research Society Spring Meeting (E-MRS 2012)*, Strasbourg, France, May 14-18, 2012.

[A.9] J. V. Pimentel, M. Evaristo, T. Polcar, and A. Cavaleiro, " Self-lubricating W-S-C-Cr tribological coatings deposited by r.f. magnetron sputtering", *Thirteenth International Conference on Plasma Surface Engineering (PSE 2012)*, Garmisch-Partenkirchen, Germany, Sep. 10-14, 2012.

[A.10] J. V. Pimentel, M. Danek, T. Polcar, and A. Cavaleiro. Effect of patterned surface on the tribology of W-S-C/Cr self-lubricant coatings. Submitted to *Surface and Coatings Technology*, 2013.

Citations of [A.1]

[A.11] T. Polcar, and A. Cavaleiro. Review on self-lubricant transition metal dichalcogenide nanocomposite coatings alloyed with carbon, *Surf. Coat. Technol.* 206 (2011) 686.

[A.12] A. Shtertser, C. Muders, S. Veselov, S. Zlobin, V. Ulianitsky, X. Jiang, and V. Bataev. Computer controlled detonation spraying of WC/Co coatings containing MoS2 solid lubricant, *Surf. Coat. Technol.* 206 (2012) 4763.

Citations of [A.2]

[A.13] X.-F- Yang, P.-L. Song, S.-R. Wang, L.-Y. Yang, and Y.-J. Wang. Wear properties of self-lubricating Al2O3/TiC/CaF2 ceramic composites, *Rengong Jingti Xuebao* 41 (2012) 1741.

Work unrelated to the doctoral thesis

[A.14] G. S. Beserra, J. F. Eusse, A. M. Sampaio, J. V. Pimentel, and R. P. Jacobi, "A VHDL-AMS Co-Simulation of a System on Chip for Wireless Sensor Networks", *XVI IBERCHIP Workshop (IBERCHIP 2010)*, Foz do Iguaçu, Brazil, Feb. 23-25, 2010.

[A.15] J. V. Pimentel, and J. C. Costa, "A Methodology for Describing Analog/Mixed-Signal Blocks as IP", *IP-Embedded Systems Conference (IP/ESC'09)*, Grenoble, France, Dec. 01-03, 2009. Published online as full article in Design & Reuse, 2009. (Available at: http://www.design-reuse.com/ articles/25000/analog-mixed-signal-ip-description.html)

[A.16] J. V. Pimentel, D. C. Cafe, J. E. G. Medeiros, G. S. Beserra, L. C. Neves, J. G. Guimaraes, and J. C. Costa, "An Introductory Course in VLSI CMOS Design", *Edutech 2009*, Florianópolis, Brazil, Oct. 15-16, 2009.

[A.17] J. V. Pimentel, and J. C. Costa, "VHDL-AMS Modeling of Analog/Mixed-Signal IP Blocks", *9th Microelectronics Student Forum – Chip on the Dunes (SForum 2009)*, Natal, Brazil, Aug. 31–Sep. 03, 2009.

Summary

Thin films composed of transition metal dichalcogenides have been used in the past as solid lubricants for their good tribological properties, especially in vacuum or dry conditions. However, pure TMD coatings typically exhibit low hardness, poor adhesion, and are susceptible to detrimental effects of humidity. Doping TMD films is an approach that has been shown to improve their mechanical properties and tribological performance.

In this thesis, self-lubricant thin films based on doped TMDs (particularly molybdenum and tungsten disulfides) are investigated. The focus is kept on their tribological performance in humid air. Numerous factors that influence the films' properties and tribological behaviour – such as deposition parameters, choice and concentration of dopant element(s), and testing conditions – are analysed and discussed. The characterisation of the coatings and the results obtained are presented in detail.

The coatings were deposited in several different chemical compositions. They were examined in their as-deposited state as well as during and after tribological tests. Their characterisation was carried out using various experimental techniques, among them new methods and innovative approaches. The coatings exhibited improvements in load-bearing capacity, adhesion, and tribological properties in comparison with pure TMD films. Common traits could be observed among the different compositions, which helped elucidate the characteristics of TMD-based films in general, including the role of the dopants on the improvement of hardness and on the formation of a low-friction tribolayer. It was possible to verify the adaptive and self-lubricating characteristics of the films and to gain a further understanding of how they originate.